Functional Magnetic Resonance Imaging: Diffusion Weighted and Chemical Shift Imaging in Head and Neck

FONG, Kwan Ying

A Thesis Submitted in Partial Fulfilment
of the Requirements for the Degree of
Master of Philosophy
in
Medical Imaging

The Chinese University of Hong Kong

April 2010

Thesis/Assessment Committee

Professor Wang, Yi Xiang (Chair)
Professor King, Ann Dorothy (Thesis Supervisor)
Dr. Yeung, Ka Wai David (Thesis Co-supervisor)
Professor Chu, Chiu Wing Winnie (Committee Member)
Professor Michael Tin-cheung YING (External Examiner)

Abstract

Magnetic resonance imaging (MRI) is used for characterization and diagnosis of head and neck tumors as well as staging and monitoring the treatment response of patients with cancer. The anatomical information provided by conventional MRI lacks specificity in characterizing head and neck tumors and in monitoring cancer response to treatment. New, non-invasive MRI techniques, such as Diffusion-Weighted Imaging (DWI) and Chemical Shift Imaging (CSI), which look at tumor function rather than morphology, have the potential to improve accuracy in the MRI evaluation of head and neck tumors. However, in the head and neck region local magnetic susceptibility differences between tissues cause magnetic field inhomogeneity resulting in severe susceptibility artifacts which cause image distortion in DWI and spectral peak broadening in CSI. Recently some of the problems with susceptibility artifact have been overcome for DWI and this technique has developed to the stage where it can be used as a research tool in the head and neck. On the other hand, CSI has yet to be developed to the stage where it produces data of sufficient quality for research. The two main aims of this thesis are to (1) evaluate the role of DWI in characterizing head and neck cancers with an emphasis on nasopharyngeal carcinoma which occurs at the skull base in an area that is prone to susceptibility problems and (2) develop a method to improve CSI so that it can produce functional data of sufficient quality to allow it to be used as a research tool.

DWI was performed on patients with nasopharyngeal carcinoma (NPC) to determine the apparent diffusion coefficient (ADC) of the primary cancer and the metastatic nodes. The ADC of the primary NPC was compared with two other common primary head and neck cancers, squamous cell carcinoma (SCC) and non-Hodgkin's

lymphoma (NHL) to determine if the ADC could be used to differentiate between these three cancers. In order to develop a method to improve the local magnetic field homogeneity for CSI, an anti-susceptibility device and different shimming methods were tested using a custom-made phantom containing Choline compound samples. The optimized sequence was then used to try to obtain functional data in patients with head and neck tumors.

The results showed that DWI is a feasible technique for examining head and neck cancers, even at sites that suffer from susceptibility artifacts such as the skull base. The mean ADC value for primary NPC was $0.984 \pm 0.161 \times 10^{-3}$ mm^2/s which was significantly different ($p < 0.001$, Kruskal-Wallis test) from SCC and NHL ADC of $1.14 \pm 0.196 \times 10^{-3}$ mm^2/s and $0.746 \pm 0.19 \times 10^{-3}$ mm^2/s respectively, suggesting that the technique may be useful in the characterization of head and neck cancers. For CSI, the results showed that local magnetic field homogeneity could be improved by employing an anti-susceptibility device and applying a second-order shimming method. This resulted in substantial improvement in spectral linewidth and for the first time allowed CSI to be successfully employed in the head and neck producing functional data on the distribution of choline containing compounds (Cho) in patients with head and neck tumors. These preliminary results showed that CSI may have the potential to guide biopsies of head and neck tumors as well as may be useful in the characterization of head and neck lesions.

摘要

磁共振成像（MRI）技术被广泛地用于头颈部肿瘤的特征描述和诊断，並且能夠分級和监测癌症患者对抗癌治疗的反应。由于传统的 MRI 技术所提供的解剖讯息用于头颈部肿瘤特征分析及监测癌症治疗的反应方面缺乏特异性。 所以，新的无创性 MRI 技术如弥散加权成像（DWI）和化学位移成像（CSI），可以提供肿瘤功能方面的讯息，而非形态方面，因此能够在很大程度上提高 MRI 对头颈部肿瘤的评估的准确性。然而，由於在头颈部位，组织之间的磁化率不同导致不均匀磁场，造成严重的磁敏感性伪影，而致造成 DWI 影像失真和 CSI 谱线增宽的问题。 最近，DWI 已经克服了一些磁敏感导致的伪影的问题，并且将这个技术发展到了可以作为头颈部研究工具使用的阶段。然而，另一方面，CSI 仍有待开发到可以生产足够的质量的数据进行研究的阶段。因此，本课题的二个主要目标是：(1) 探讨 DWI 在描述头颈癌特征中的作用，并重点探讨极易造成磁敏感性问题的颅底部的鼻咽癌肿瘤；(2) 研究用来改善 CSI 成像的方法，以便它能够生产足够的质量的数据，并将其作为一个研究工具被开发应用。

在 DWI 方面，对头颈癌患者进行 DWI 扫描，以测定原发鼻咽癌和转移淋巴结的表观扩散系数(apparent diffusion coefficient, ADC)值， 以及比较原发鼻咽癌(Primary NPC)和另外两种原发头颈癌、鳞状细胞癌(squamous cell carcinoma, SCC)和非霍奇金淋巴瘤(non-Hodgkin's lymphoma, NHL)的 ADC 值，以评估 ADC 值是否可以用来区分这三种癌症。在 CSI 方面，为了研究一个有效的方法来提高局域磁场均匀性，运用实验订制的胆碱类复合样品的模型，对

抗磁敏感性装置和不同的均场方法进行了测试。然后，尝试用优化的序列来获得与头颈部肿瘤患者在肿瘤功能方面的数据。

DWI 结果显示：DWI 是一个可行的检测头颈部肿瘤技术，即使在一个容易造成磁敏感性伪影的部位，如颅底。原发鼻咽癌的 ADC 值 (0.984 ± 0.161 $\times 10^{-3}$ mm^2/s)与鳞状细胞癌 (1.14 ± 0.196 $\times 10^{-3}$ mm^2/s)和非霍奇金淋巴瘤(0.746 ± 0.19 $\times 10^{-3}$ mm^2/s) 比较，差异有统计学意义($p < 0.001$, Kruskal-Wallis test)。表明 DWI 技术可用于头颈癌的特徵描述。CSI 结果显示：抗磁敏感性装置和第二阶均场方法对局域磁场均匀性有明显提高。其结果显示谱线宽度都有实质性的改进，并首次成功将 CSI 技术应用于头颈部肿瘤患者，产生含有胆碱类复合物的分布的数据。以上初步的研究表明，CSI 对导引头颈部肿瘤针切片检查有极大的潜力，并且可用于头颈癌的特征描述。

Acknowledgements

As I look back on these years at The Prince of Wales Hospital it is apparent that I owe a tremendous debt of gratitude to several individuals and institutions for their help and encouragement in the completion of this thesis.

First of all, I would like to express my deepest appreciation to my supervisors, Dr. King, AD and Dr. Yeung, KW David. I am grateful for their support, expert guidance, valuable advice and enthusiastic commitment to my research, despite their tight schedules. I would like to dedicate myself to the career of medical imaging and oncology, following them as role models.

I would also like to extend my special thank to my colleagues in the departments of Diagnostic Radiology & the Organ Imaging, Clinical Oncology and Chemical Pathology, for helping me throughout the process of this research. Without their support this research would never have been completed.

I gratefully acknowledge Dr. William Goggins and Dr. Theo Lorentz, for their kind assistances and support for this research.

Finally, I would also like to thank my family members for their unconditional and everlasting love and support during my work on this study.

Contents

Chapter 1: Introduction, problems and objectives

1.1 Introduction

Cancer in the head and neck region accounts for approximately 5% of all adult cancers and are an important cause of morbidity and mortality. Medical imaging has a vital role in the management of head and neck cancer where it is used to detect and diagnosis cancer, stage and plan treatment, assess treatment response and identify recurrent tumors. One of these imaging techniques is magnetic resonance imaging (MRI). MRI is a non-invasive diagnostic imaging technique, which has been in clinical use since the early 1980s. MRI uses a strong magnet and radiofrequency waves to produce images with extraordinary detail of the body's organs, tissues, bones and other internal body structures, without the use of ionizing radiation. It is based on the principle of nuclear magnetic resonance (NMR) to provide cross-sectional images in any plane or three-dimensional images of the body that can be viewed from any angle.

MRI is one of the best imaging modalities for demonstrating the extent of the head and neck cancers because of its multiplanar capabilities and the excellent soft tissue contrast and resolution. As a result, MRI has become a powerful diagnostic tool for evaluation of head and neck tumor patients because it provides high quality morphological tumor information. However, MRI is also a very versatile technique which has the ability to provide functional information about tumor physiology and biochemistry, an advantage which is not available from other imaging modalities such as computed tomography (CT) and ultrasound (US). Some MR functional techniques are already being used to evaluate head and neck tumors, include magnetic resonance spectroscopy (MRS), which assesses metabolic activity, and

dynamic contrast-enhanced MRI (DCE-MRI), which assess tumor microcirculation (Arend Heerschap, 2007; Oberholzer, K. *et al.*, 2008). Two novel functional MR techniques in the head and neck are diffusion-weighted imaging (DWI) and chemical shift imaging (CSI) and these two functional techniques are assessed in this thesis. DWI is highly sensitive to the diffusion of water molecules and can produce diffusion-weighted (DW) images by employing a pair of diffusion-sensitizing gradient pulses. The term diffusion refers to the thermal random motion of water molecules, known as Brownian motion, which results from the thermal energy carried by these molecules (Le Bihan, D. *et al.*, 2006). Measurement of diffusion signal at different diffusion-sensitizing gradient pulses (b-values) can be used to calculate apparent diffusion coefficient (ADC), which is a quantitative value for the degree of water diffusion. Clinical application of DWI has been primarily used for early detection of ischemic stroke because of its high sensitivity and specificity to acute ischemic stroke (Schaefer, P. W., 2001). Recently, DWI with ADC measurement is gaining interest for assessing cancers and tumor cellularity in the brain and body.

Single voxel proton magnetic resonance spectroscopy SV ^{1}H-MRS can detect a wide variety of proton-containing metabolites in tumors, such as N-acetylaspartate, choline, creatine, lactate, and citrate (Catherine Westbrook *et al.*, 2005; Payne, G. S. and Leach, M. O., 2006; Robin de Graaf, 2004). This metabolic information is displayed as a spectrum.

Chemical shift imaging (CSI) takes the SV MRS technique a step further and provides images which map the spatial distribution of specific metabolites. CSI obtains localized spectra from multiple adjacent voxels based on the MRS and then uses them to form metabolite maps of specific metabolites in large heterogeneous

lesions. CSI is also known as magnetic resonance spectroscopy imaging (MRSI) and it has been used for the evaluation of tumors in the brain, breast and prostate but not in the head and neck.

1.2 Problems

DWI and CSI techniques depend on the MRI method to create images but DWI and CSI both require a very high degree of magnetic field homogeneity over the region of interest. The human neck contains many air/soft tissue interfaces which cause susceptibility differences that readily disturb magnetic field homogeneity over the region of the head and neck, resulting in artifacts that degrade the functional data. DWI will suffer from severe susceptibility-induced image distortion, particularly in region of skull base. For CSI, the technique will suffer from the spectral peak broadening and poor spatial resolution, and at present current CSI techniques have not been developed to work in the head and neck.

1.3 Objectives

In this study the two main objectives are as follows;

1. To evaluate the role of DWI in the characterization of head and neck cancers with an emphasis on nasopharyngeal carcinoma that occurs at the skull base in a challenging region for MR imaging.
2. To develop a CSI method to improve magnetic field homogeneity over the head and neck region, so that CSI can produce functional data of sufficient quality to allow it suitable for clinical applications in the head and neck.

Chapter 2: Background

2.1. Head and Neck Cancer

Worldwide, it is estimated that more than 500 000 people are diagnosed with head and neck cancer per year (Karen Belkic, 2004). In the United States, head and neck cancer accounts for approximately 5% of adult cancers. In Hong Kong, the annual incidence rates of head and neck cancer in 2006 for men and women was approximately 21.2 and 7.4 cases per 100, 000 people, respectively (Hong Kong Cancer Registry, 2008). The incidence rates are more than twice as high in men as in women, and are greatest in men who are older than 50 (American Cancer Society, 2006). The incidence rate of head and neck cancer tends to increase with age and head and neck cancer has become a public health problem for aging populations. The long-term use of tobacco and alcohol are two of the main causative factors for head and neck cancer. Other risk factors for head and neck cancer include genetic factors and other cancer-causing substances.

Cancers of the head and neck comprise a heterogeneous group of malignancies. The most common head and neck malignancies are squamous cell carcinomas (SCC), usually arising in the upper aerodigestive tract (Quon, H. *et al.*, 2001). Nasopharyngeal carcinomas (NPC) and malignant lymphomas (ML) are other less common types of head and neck malignancies. NPC develops in the nasopharynx and often invades the skull base. NPC is highly prevalent in southern China, but uncommon in western countries (Her, C., 2001). It is believed that NPC is associated with Epstein-Barr virus (EBV) infection. ML are neoplasms of lymphoid cells, divided into Hodgkin lymphomas (HL) and non-Hodgkin lymphomas (NHL)

(Atul B. Mehta and A. Victor Hoffbrand, 2000). The primary site of ML may involve nodal or extranodal sites (Vega, F. *et al.*, 2005).

Malignant tumors of the head and neck are often fast growing cancers that tend to spread locally to adjacent tissues and metastasize to lymph nodes and distant sites. Patients with head and neck tumors may experience symptoms at the primary site such as a lump, pain, bleeding or loss of function or they may only become aware of the problem once the disease has spread to nodes in the neck.

Early stage head and neck cancer (stage I and II) is curable in 60% to 95% of patients (Bruce Brockstein and Gregory Masters, 2003). The standard treatment options include surgery and/or radiation therapy. For patients with advanced-stage cancer, chemotherapy combined with radiotherapy can be used to control cancer growth and decrease the risk of cancer spread, as well as preserve function (Forastiere, A. A. *et al.*, 2003; Urba, S. G. *et al.*, 2000).

2.2 Diagnostic Imaging of Head and Neck Cancer

The management of patients with head and neck tumor depends on patient history, clinical examination, biopsy and medical imaging. Medical imaging is used to detect and diagnose cancer, stage and plan treatment, assess treatment response and identify recurrent tumors. Medical imaging is performed because it provides a safe, rapid and reliable approach to managing cancer of the head and neck. Commonly used imaging modalities are ultrasound (US), computed tomography (CT) and magnetic resonance imaging (MRI) which provide anatomical information. They show the normal structures in the head and neck and provide morphological information on tumor size, shape, extent and pattern of contrast enhancement. They also guide biopsy to confirm the diagnosis of head and neck cancer. Of these techniques MRI is

one of the best for demonstrating the extent of the head and neck cancers because of its multiplanar capabilities and the excellent soft tissue contrast and resolution. It also can see deep structures not identified by ultrasound, does not involve ionizing radiation used to produce CT images and because it is a versatile technique it can also provide functional data. Another technique in clinical use is positron emission tomography with fluorine-18 fluorodeoxyglucose (^{18}FDG PET) which provides functional information but has the draw back that it needs to be combined with CT for anatomical data.

Staging is important for the management of head and neck cancer because it provides prognostic information on patients with head and neck cancer. This information can be used to determine effective treatment options for head and neck cancer as well as predict outcome in patients with head and neck cancer. Clinically, staging is determined with the tumor-node-metastasis (TNM) system, which is based on the American Joint Committee on Cancer/ International Union Against Cancer (AJCC/UICC) TNM classification system (Frederick L. Greene *et al.*, 2006). The TNM staging system includes the T-stage to determine the local invasion and tumor size, the N-stage to determine the degree of involvement of the lymph nodes, and the M-stage to identify the presence of distant metastasis. Staging by palpation is well known to be an inaccurate method because palpation is unable to assess small, deep mobile lesions in the head and neck region, especially the neck lymph nodes, including the retropharyngeal nodes and the most superior internal jugular nodes (Lam, W. W. *et al.*, 1997). Staging therefore is highly dependent on imaging.

Over the past decades, the management of head and neck cancer has improved significantly due to the improvement in therapy as well as the advancements and refinements in imaging techniques for monitoring therapy. Conventional imaging

modalities usually provide morphological information for the management of head and neck cancer patients. Conventional CT and MRI depend on changes in tumor size to assess tumor response to treatment. The size of tumor can be measured using the following measurements: bi-dimensional measurements (BDM) from the World Health Organization (WHO) guidelines which are obtained by the product of the two greatest perpendicular diameters of the tumor (Miller, A. B. *et al.*, 1981), uni-dimensional measurements (UDM) from the Response Evaluation Criteria in Solid Tumors (RECIST) guidelines which are obtained by taking the single greatest diameter of tumor (Therasse, P. *et al.*, 2000), and tumor volume measurements which are determined with the sum of tumor areas (Suresh K. Mukherji *et al.*, 2004). Under WHO and RECIST guidelines, imaging of tumor response is determined by a reduction of tumor size during treatment or after treatment in head and neck cancer, and any aggressive tumor that enlarges or fails to reduce the tumor size significantly may be considered to fail to response to treatment. Unfortunately change in size does not always reflect the true cancer response and so recently, functional imaging techniques have been gaining interest for monitoring tumor response to treatment. Positron emission tomography with fluorine-18 fluorodeoxyglucose (^{18}FDG PET), as a functional imaging technique, provides metabolite information regarding changes in glucose metabolism in cancer cells (Catherine Castaigne *et al.*, 2008) and is already in routine clinical practice for assessing tumor response to therapy in patients with head and neck cancer (Brun, E. *et al.*, 2002; Kostakoglu, L. and Goldsmith, S. J., 2004), but as stated above it does not provide any anatomical data. In this respect new MRI based functional techniques have the advantage that they can be performed at the same time as the usual MRI examination which produces anatomical information.

2.3. Magnetic Resonance Imaging- Physics

2.3.1 Nuclear Magnetic Resonance Principle

Nuclear magnetic resonance (NMR) is a physical phenomenon that is observed only in nuclei with odd numbers of nucleons having an intrinsic property called spin. In the presence of an external magnetic field, the spinning nuclei have tendency to align their axes along the lines of magnetic field. However, the alignment is not exact, which produces a wobbly rotation around the magnetic field. This wobbly rotation causes the spin-up and spin-down nuclei to precess around the direction of the magnetic field (B_0) at a precessional frequency (Figure 2.1). The precessional frequency, which is called the Larmor frequency, is unique for each type of nuclei. Radiofrequency (RF) energy is also applied to excite these nuclei in the presence of the magnetic field. The excited nuclei will resonate at a specific frequency according to the type of nuclei. For resonance of specific type of nuclei to occur, RF energy must be applied at exactly the Larmor frequency of that type of nuclei. Typical nuclei used in NMR are, for example, hydrogen (^{1}H), carbon (^{13}C), fluorine (^{19}F), sodium (^{23}Na) or phosphorus (^{31}P) (Alessandro Lascialfari and Corti, Maurizio, 2007; Catherine Westbrook. and Roth, Carolyn Kaut, 2005; Gary Liney, 2006; Schaeffter, T. and Dahnke, H., 2008).

2.3.2 Proton Magnetic Resonance Imaging

The hydrogen nucleus is the most commonly used in clinical MRI because it is highly abundant in the human body. A hydrogen atom with a positively charged proton generates a magnetic field, which is called magnetic moment (B). The magnetic moment acts like a small magnet with magnetic north and south poles, called a magnetic dipole (Figure 2.2). When ^{1}H nuclei are placed in a static magnetic

field (B_o), the magnetic dipoles align either parallel or anti-parallel to B_o due to the two possible energy levels, known as Zeeman levels (Figure 2.3), which includes the lower energy level (E_1) and the upper energy level (E_2). The energy difference (Δ E) between these two possible energy levels is obtained by the equation:

$\Delta E = E_2 - E_1$, in which Δ E is proportional to B_o and is given by the equation:

$\Delta \mathrm{E} = h\frac{\gamma}{2\pi}B_o$, where h is the Planck's constant and γ is the gyromagnetic ratio.

For the spinning ^{1}H nucleus, Δ E is associated with a resonance frequency in the radio-frequency (RF) range, given by the equation: $\Delta \mathrm{E} = h\frac{\omega_o}{2\pi}$, in which transitions between these two possible energy levels can be stimulated by energy at this resonance frequency called the Larmor frequency (ω_o), which is given by the Larmor equation: $\omega_o = \gamma B_o$.

In the static magnetic field, the alignment of the hydrogen nuclei occurs as a result of generating a net magnetic moment, which is called a magnetization (M_o) in the direction of B_o. The magnetization can be turned from one direction to another direction by applying a RF pulse that has exactly the same frequency as the Larmor frequency of hydrogen (ω_o) and a magnetic field (B_1) perpendicular to B_o (Figure 2.4). The angle between M_o and B_o is called the flip angle, of which magnitude is determined by the type of RF pulse energy that is applied. For an example, a 90° RF pulse is applied as a result of a 90° flip angle of the magnetization (M_o).

MR signals are usually collected by using the MR receiver coils. When coherent or in phase magnetization cuts across the coil, it will induce a current or voltage, which is known as the source of magnetic resonance (MR) signal. When the RF pulse

energy is switch off, relaxation occurs in which some of the nuclei at high energy level will give off energy in the form of radio wave and return to their lower energy level. This causes the magnetization to return to the original alignment with B_o, thus generating the free induction decay (FID) signal. In the MRI system, the FID signal is converted from time domain to frequency domain using a Fourier transform (Figure 2.5). This frequency domain signal provides an easy method to determine the amplitude of each frequency component.

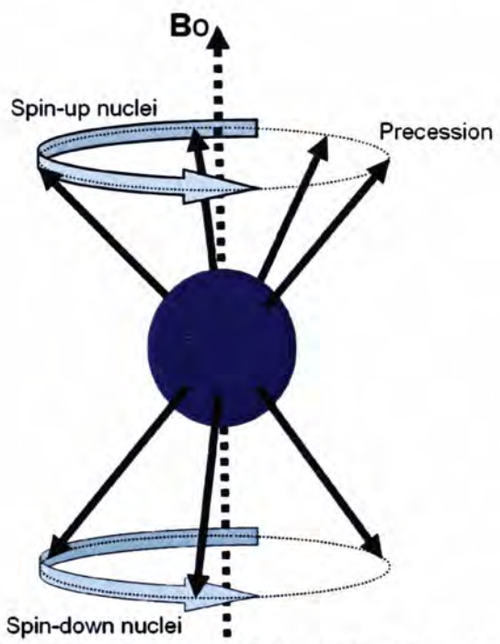

Figure 2.1: Precession of the spin-up and spin-down nuclei.

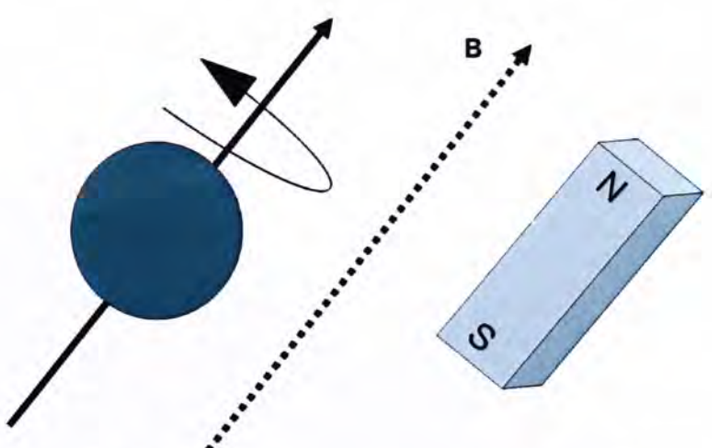

Figure 2.2: The spinning proton acts as a small magnet.

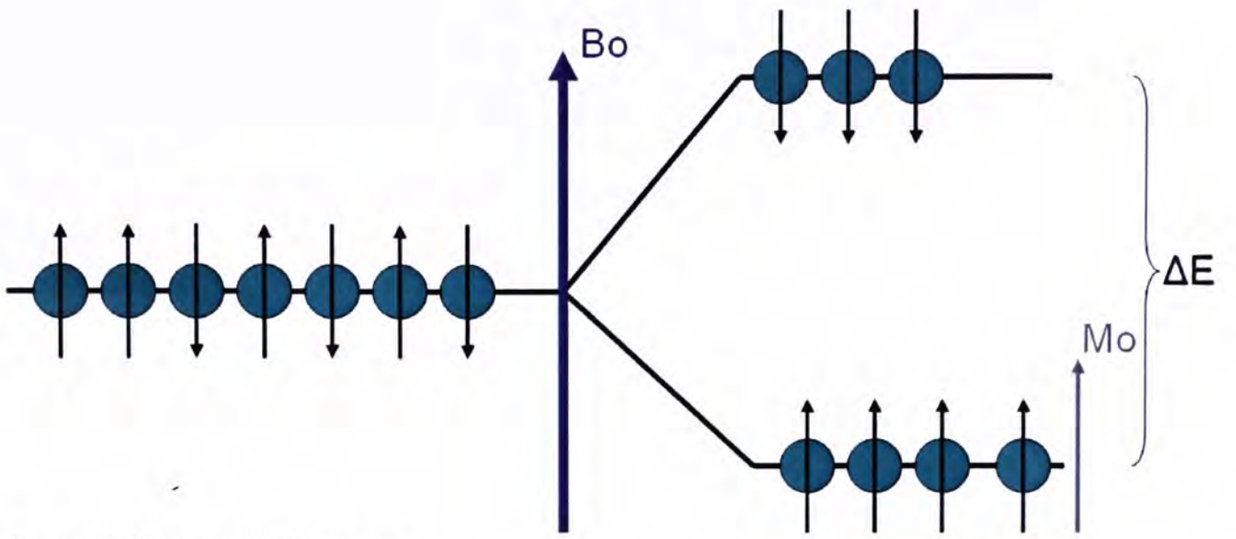

Figure 2.3: Zeeman diagram.

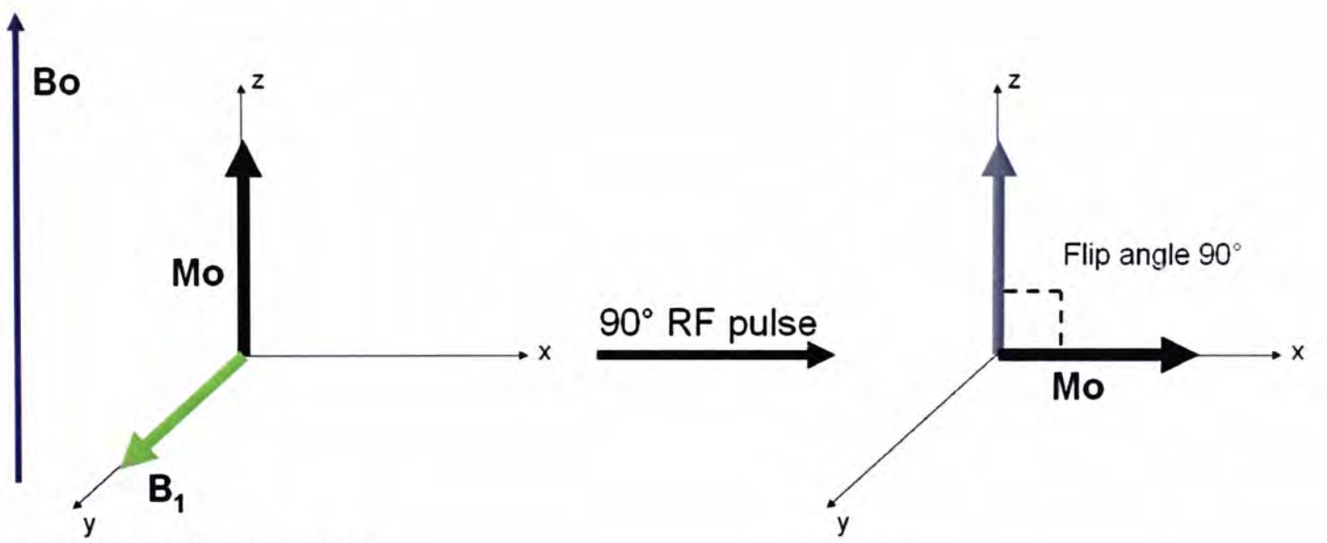

Figure 2.4: The flip angle.

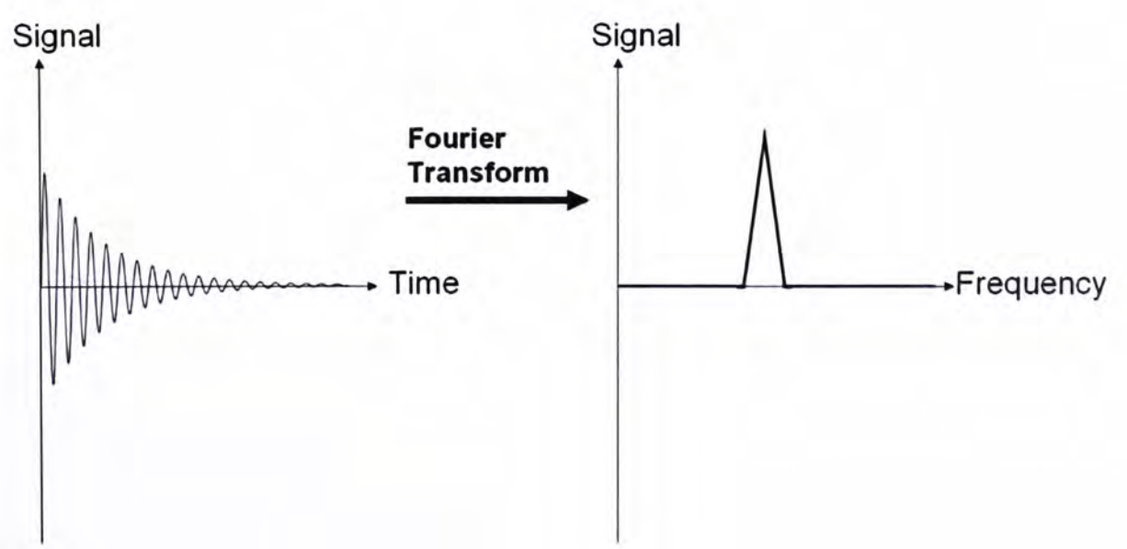

Figure 2.5: The Fourier transform of a free induction decay signal.

2.3.3 Relaxation

Relaxation is the process by which the magnetic moments return to realign to the static magnetic field by releasing the absorbed RF pulse energy (Mark A. Brown and Richard C. Semelka, 2006). This process of relaxation has two independent time constants, known as the spin-lattice (T1) and the spin-spin (T2) relaxation time. The T1 relaxation time represents the time needed for the longitudinal component of the magnetization to recover 63% of its original length, whereas the T2 relaxation time represents the time needed for the transverse component of the magnetization to return to 37% of its original length.

2.3.4 T1- and T2-weighted Imaging

Each tissue has a specific relaxation time and proton density, thereby MRI has the ability to produce different types of image contrast, or so-called, weighting (Mori, S. and Barker, P. B., 1999). The T1-contrast mainly depends on the differences in the T1 relaxation times between tissues, whereas the T2-contrast mainly depends on the differences in the T2 relaxation times between tissues. In T1-weighted (T1W) imaging, a tissue with short T1 relaxation time, such as fat tissue, shows high intensity signal on the T1W image, and vice versa. On the other hands, a tissue with long T2 relaxation time, such as water, shows high intensity signal on the T2W image, and vice versa. The proton density contrast is related to the number of excited protons per unit tissue. Tissue with a high proton density, such as brain tissue, tends to produce a high signal intensity compared with tissue with a low proton density, such as bone tissue.

2.3.5 Diffusion Weighted Imaging (DWI)

Diffusion is random motion of water molecules in biological tissues, known as Brownian motion, resulting from thermal energy (T. Scarabino *et al.*, 2006). This motion is constant but dependent on temperature and the surroundings. In biological tissues, diffusion is not entirely random, but restricted by the tissue strictures. Subtle changes in tissues components, such as cell walls, membranes, intracellular organs, macromolecules, can limit or restrict the degree of water diffusion. In many tissues, diffusion is restricted in all directions and the process is called isotropic diffusion. In some highly structured tissues, such as cerebral white matter and muscle, diffusion is anisotropic due to restricted diffusion along one particular direction. It is usually considered and has been shown that tumor diffusion is isotropic (Andrzej Dzik-Jurasz and Simon Doran, 2006).

Diffusion-weighted imaging (DWI) is a nuclear magnetic resonance (NMR) technique based on the phenomenon of diffusion. DWI is highly sensitive to molecular movement and has the ability to evaluate the diffusion of water molecules. It is commonly performed by adding a pair of strong magnetic field gradients to the MRI pulse sequence, making it sensitive to diffusion of water molecules (Heidi Johansen-Berg and Timothy E. J. Behrens, 2009). These additional gradients with equal amplitude but opposite gradient direction are applied before and after the 180° pulse (Figure 2.6). The first gradient is used to dephase the water molecules, causing them to acquire phase shifts, and the second gradient is used to rephase the dephased spins. For no net movement of water molecules, the phase shift caused by the first gradient will be cancelled out by the second gradient, producing a strong signal. For net movement or diffusion, on the other hand, the dephased spins are not completely refocused by the second gradient, resulting in incomplete spin rephasing and thereby

signal attenuation (Wen -Yih Isaac Tseng and Li-Wei Kuo, 2008). The diffusion induced signal attenuation is given by the equation: $\frac{S(b)}{S_o} = e^{-bD}$, where S_o is the signal intensity without the gradient application, $S(b)$ is the signal intensity with the gradient application and D is a diffusion coefficient, which is referred to as apparent diffusion coefficient (ADC) measured in biological tissues (Mori, S. and Barker, P. B., 1999). The b value is a gradient factor related to the gradient strength (G), the duration of each gradient pulse (δ) and the time between the beginning of the two gradient pulses (Δ), according to this equation: $b = \gamma^2 G^2 \delta^2 (\Delta - \frac{\delta}{3})$ where γ is the gyromagnetic ratio (Bammer, R., 2003). The isotropic diffusion image (DW) is created by simply averaging DW images acquired with the diffusion sensitizing gradient along the readout, phase-encoding, and section-selection directions (Le Bihan, D. *et al.*, 1988). For mapping of ADC, the DW images with at least two different b values are required. The ADC value derived from ADC map is calculated with a linear least-squares regression method by using this equation: $In\frac{S(b)}{S_o} = -(ADC) \times b$. The slope of the linear regression line describes the ADC value (Koh, D. M. and Collins, D. J., 2007). To reduce the estimation error in the calculation of ADC, more b values should be used.

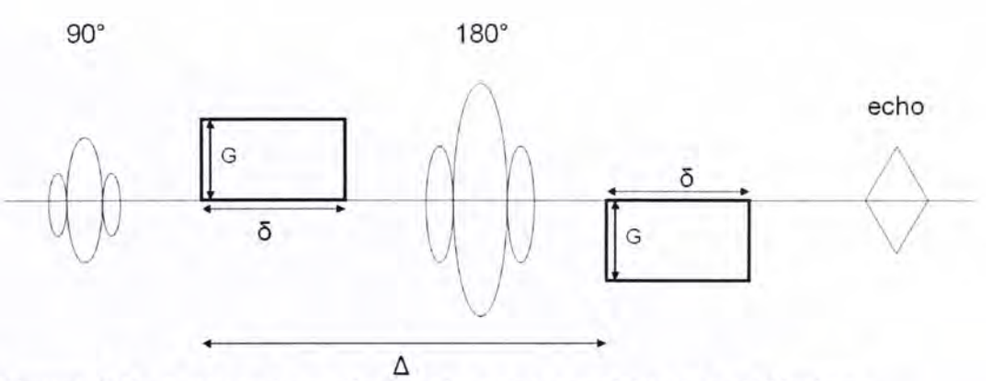

Figure 2.6: A pulsed gradient spin echo sensitized to diffusion.

2.3.6 Magnetic Resonance Spectroscopy- Single Voxel Spectroscopy and Chemical Shift Imaging

Single Voxel Magnetic Resonance Spectroscopy

Chemical shift is a phenomenon that occurs because the circulating electron cloud around an atomic nucleus generates a magnetic field that tends to oppose or shield the nucleus from the external magnetic field. This shielding effect causes a subtle difference in the magnetic field at the nucleus, and thus leading to the resonance to shift slightly to a different frequency. This small difference in resonance frequencies depending on the chemical environment is called chemical shift. Single voxel magnetic resonance spectroscopy (SV MRS) is also called nuclear magnetic resonance spectroscopy (NMRS), which is a NMR technique based on the chemical shift phenomenon. MRS is sensitive to the chemical environment of the nuclei and is able to probe the chemical structure of molecules. MRS uses RF pulses and a strong magnetic field to obtain the signal of nuclei from the region of interest (ROI). The MRS signal is displayed as a frequency spectrum in a single voxel, which shows signal intensity versus chemical shift between different molecules. The chemical shift is caused by the fact that a weak magnetic field generated by the nucleus tends to shield the nucleus from the external magnetic field, and thus generates a net magnetic field strength (B_i) at the nucleus, which is defined by the equation: $B_i = B_0(1-\sigma_i)$, where σ_i is the shielding factor for nucleus i (Nouha Mikhael Salibi and Mark A. Brown, 1998). Because nuclei (e.g. protons) in different chemical environments and locations experience different magnetic field strengths (Brateman, L., 1986), the resonant frequency of each spin will be different, depending on the amount of local nuclear shielding that depends on the electron density around a nucleus (Lindsay T. Byrne, 2008). Therefore, the resonant

frequency as indicated by the Larmor equation must also be modified into this form: $\varpi_i = \gamma B_o(1-\sigma_i)$, where ϖ_i is the frequency for the *i*th spin. This modified Larmor equation shows that the resonant frequency of a spin will shift depending on the magnetic field strength as well as its chemical environment. In this case, the shift of resonant frequency is referred to chemical shift. The chemical shift (σ_i), generally expressed in parts per million (ppm), is defined by the equation:

$\sigma_i = (\varpi_i - \omega_{ref})/\varpi_{ref}$, where ϖ_{ref} is the resonant frequency for the reference nuclei. The chemical shift is very small but useful to identify different molecules. A functional group or chemical compound containing one or more spins will have a unique chemical shift, which is referred to a specific position of the spectrum. This specific position of a given resonant peak is usually given with respect to a reference peak (Edward F. Jackson, 2001). We can therefore determine the structure of a molecule by measuring the position of the resonance peak in the spectrum. Table 2.1 (adapted from Payne, G.S. and Leach, M. O., 2006; Catherine Westbrook et al., 2005; Robin de Graaf, 2004) shows the proton chemical shifts corresponding to specific metabolites in human tissues. MRS, thus can determine the differences between chemical compounds in which the spins are present.

Water Suppression

In proton MRS, the magnetization of water is much larger than the magnetization of all metabolites of interest, and therefore the water signal giving a very broad line shape overlaps the neighboring signals from the metabolites (Klose, U., 2008). This causes the metabolite peaks undetectable in the spectrum. For this reason, the most common approach is to suppress the water signal using a frequency selective, 90° pulses, which is called chemical shift-selective water suppression (CHESS) pulses.

Metabolite	^{1}H chemical shift of main peak (ppm)	Description
Choline-containing compounds (Cho)	3.2	The signal of choline consists of choline, phosphocholine and glycerophosphorylcholine. Cho are related to cellular membrane turnover.
Creatine (Ćr-PCr)	3.0	Cr contains creatine and phosphocreatine and it plays a role in the energy metabolism.
Citrate (Cit)	2.6	Cit is synthesized and accumulated by normal prostate cells.
N-acetylaspartate (NAA)	2.0	NAA is only present in brain and is considered a neuronal marker.
Lactate (Lac)	1.3	Lac is a product of anaerobic glycolysis.
Lipids (Lip)	0.9, 1.3	Lipid is often found in necrotic.

Table 2.1: Brief details of some metabolites seen in ^{1}H spectra of human tissues

Fat Suppression

Lipid signal acquired from the head and neck region is also a dominant signal in a spectrum (Bisdas, S. *et al.*, 2007; Star-Lack, J. M. *et al.*, 2000), and it arising from the subcutaneous regions is about a thousand times greater than the signal of metabolites (Skoch, A. *et al.*, 2008). To avoid lipid signal contamination from neighboring adipose tissues, techniques to suppress the lipid signals are often required. The outer volume suppression (OVS) is a suppression technique that can be used to suppress unwanted signals by using the OVS bands to surround ROI (Figure 2.7). OVS bands allow to exclude unwanted signals as well as to preserve the metabolic information. This OVS technique can be used to reduce lipid signal

contamination and contaminations from air, water, and other substances as well, and therefore OVS bands improve quality of CSI (R.H. Wu *et al.*, 2003).

Chemical Shift Imaging

Chemical shift imaging (CSI) is a NMR technique that combines features of imaging and spectroscopy (Nouha Mikhael Salibi and Mark A. Brown, 1998). CSI acquires spatial localized spectra from individual voxels by employing the MRS method. The localized spectra can then be displayed either as spectral maps that represent the spatial distribution of the magnetic resonance spectrum or as metabolite images that visualizes the spatial distribution of different metabolites of interest. Since CSI technique is based on the MRS method to create images or maps, CSI is also referred to magnetic resonance spectroscopic imaging (MRSI) or simply spectroscopic imaging (SI).

MRS and CSI commonly employs localization techniques, such as point resolved spectroscopy (PRESS) or stimulated echo acquisition mode (STEAM) techniques, to acquire a localized spectrum from a single voxel or spatial localized spectra from multiple adjacent voxels (Donald W. McRobbie *et al.*, 2003; Peter B. Barker, 2005). Both PRESS and STEAM techniques use a series of three selective RF pulses to define the planes of interest (Figure 2.8). PRESS (Figure 2.9) uses a slice selective 90° pulse followed by two 180° refocusing pulses, whereas STEAM (Figure 2.10) uses three 90° pulses to generate the stimulate echo. The volume localization is then accomplished using phase encoding techniques. Each phase-encoding gradient is applied to replace a slice-selection gradient. In two-dimensional (2D) single slice CSI, phase encoding gradients are performed in x and y directions, leaving one direction as a slice select. In three dimensional (3D) CSI, phase encoding gradients

are performed in all three directions of slice-selection. To acquire CSI, PRESS localization technique is generally preferred because of its superior signal to noise ratio (Nelson, S. J., 2003).

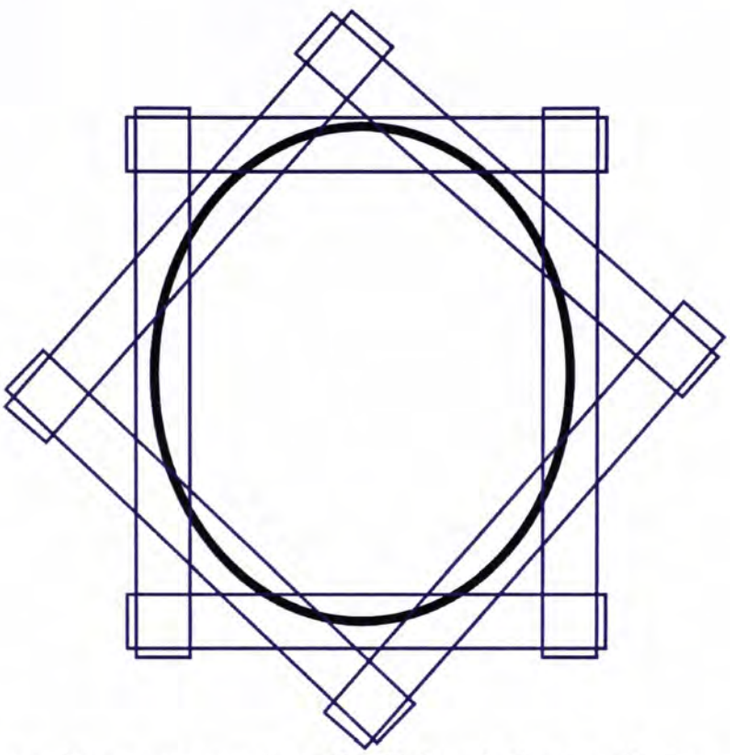

Figure 2.7: Outer volume suppression (OVS) bands (rectangles) surround the ROI.

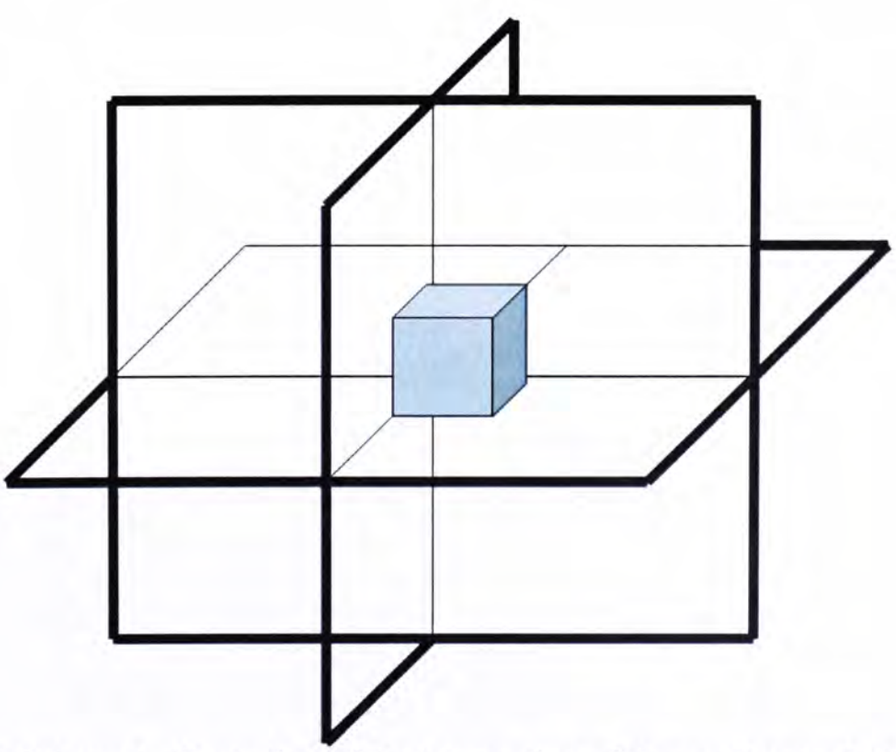

Figure 2.8: Schematic illustration of the intersection of three orthogonal planes.

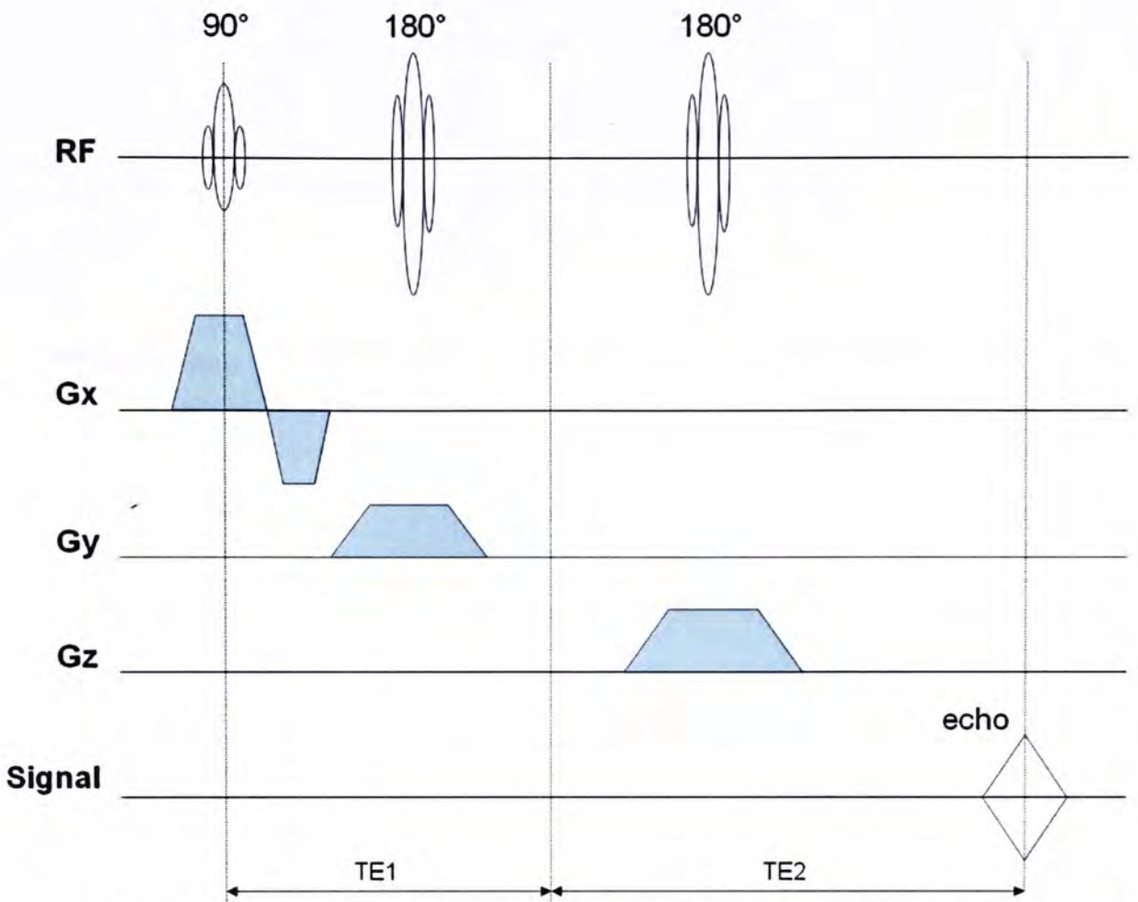

Figure 2.9: The PRESS pulse sequence. TE1 and TE2 are the first and second echo times, respectively.

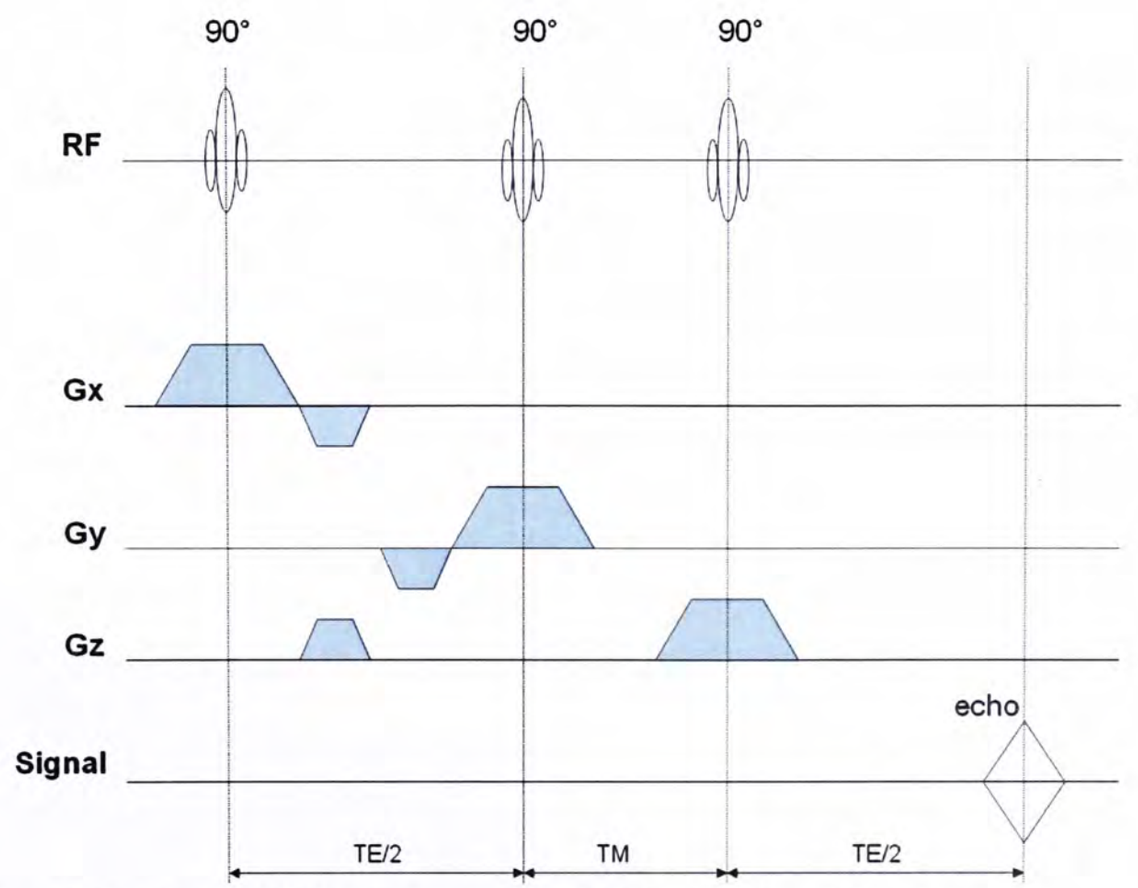

Figure 2.10: The STEAM pulse sequence. TM denotes the mixing time.

Chapter 3: Diffusion-weighted imaging in the evaluation of head and neck cancer

3.1 Introduction – Diffusion-weighted Imaging in Tumors

Diffusion-weighted imaging (DWI) is a non-invasive imaging technique that is capable of characterizing tissues and producing diffusion-weighted (DW) images based on differences in diffusion motion of water protons in tissue. Using such DW images with different b values, the apparent diffusion coefficients (ADCs) can be calculated. The term ADC refers to a quantitative value for the degree of water diffusion in biological tissues. Hence, hyper-cellular tumor tissue with smaller extra-cellular space, such as solid tumor tissue, will show low ADC values, whereas hypo-cellular tumor tissue with larger extra-cellular space, such as necrotic or cystic tumors, will show high ADC values (Ross, B. D. *et al.*, 2003). Thus, ADC values of the tissues are expected to vary according to the microstructures and physiologic states of the tissues (Sumi, M. *et al.*, 2002; Wang, J. *et al.*, 2001).

DWI has emerged as a powerful imaging tool, and with ADC can be used for lesion characterization. DWI has been applied to detect many lesions in the brain and body as well as it is used to help characterize lesions. It has been successfully used to evaluate central nervous system (CNS) disease. Previous studies have demonstrated the utility of DWI for the diagnosis and management of cerebral ischemia (Baird, A. E. *et al.*, 1997; Gonzalez, R. G. *et al.*, 1999; Lovblad, K. O. *et al.*, 1998; Schaefer, P. W. *et al.*, 2000; Sorensen, A. G. *et al.*, 1996; Warach, S. *et al.*, 1995), for the detection of white matter disorders (Tanner, S. F. *et al.*, 2000) and brain tumors (Brunberg, J. A. *et al.*, 1995; Filippi, C. G. *et al.*, 2001; Tien, R. D. *et al.*, 1994), for

the differentiation of brain lesions (Castillo, M. *et al.*, 2001; Kim, Y. J. *et al.*, 1998; Okamoto, K. *et al.*, 2000; Sugahara, T. *et al.*, 1999; Tsuruda, J. S. *et al.*, 1990), and for the detection of residual or recurrent tumors (Hein, P. A. *et al.*, 2004). Promising results have also been obtained with DWI in regions outside the CNS for differential diagnosis of benign and malignant lesions in the bone marrow (Baur, A. *et al.*, 1998; Maeda, M. *et al.*, 2003), breast (Kuroki, Y. *et al.*, 2004; Sinha, S. *et al.*, 2002), liver (Kim, T. *et ál.*, 1999; Namimoto, T. *et al.*, 1997), and lymph nodes (Abdel Razek, A. A. *et al.*, 2006; Akduman, E. I. *et al.*, 2008; Misa Sumi, Noriyuki, 2003), for characterization of cystic lesions in the ovaries (Moteki, T. and Ishizaka, H., 1999) and pancreas (Yamashita, Y. *et al.*, 1998), for evaluation of tumor response to therapies in bone (Hayashida, Y. *et al.*, 2006) and rectal cancers (Dzik-Jurasz, A. *et al.*, 2002), and for detection of malignant tumors in the prostate (Issa, B., 2002), kidney (Thoeny, H. C. *et al.*, 2005) and urinary bladder (Matsuki, M. *et al.*, 2007).

3.2 DWI of Nasopharyngeal Carcinoma

3.2.1 Introduction and Objectives

DWI has not been performed previously on primary nasopharyngeal carcinomas (NPC) because of the difficulty of performing this technique in the skull base and the ADC value of this cancer has not been established. The primary objective was to evaluate the feasibility of performing DWI using the technique descried above and establish the normal range of ADCs for undifferentiated NPC. The secondary objectives were (a) to evaluate two methods for measuring ADC employing the whole lesion (WL) and the representative section (RS) measurement techniques and (b) to compare ADCs of the primary NPC and nodal metastases.

3.2.2 Methods

Patient Selection

Head and neck cancer patients with previously untreated NPC were recruited for this prospective study. The research ethics committee approval was obtained and an informed consent was also obtained from all patients before the study.

Histological biopsy finding was the reference standard for the primary tumor, whereas the reference standard for a malignant node was based on the MRI images in which lymph nodes were evaluated for size and morphological criteria. The several conditions for selection of a malignant node were as follows: (1) in each patient, only the largest abnormal node was selected for evaluation, (2) based on the MRI criteria for characterization of lymph nodes, the node was considered as a malignant node if it had shortest axial diameter of $\geq$ 11mm in the jugulodigastric region, $\geq$5 mm in the retropharyngeal region and $\geq$ 10 mm in all other regions of the neck, (3) or as any node with necrosis or extracapsulary neoplastic spread irrespective of size (Som PM 1987; van den Crekel 1990; Lam WW 1997).

DWI

DWI– Technique Adapted for Use in the Head and Neck

DWI Protocol

In general, the isotropic diffusion-weighted (DW) image is created by simply averaging DW images acquired with the diffusion sensitizing gradient along the readout, phase-encoding, and section-selection directions (Denis Le Bihan *et al.*, 1988). Many previous DWI studies of cancers have used high b values of 1000 s/mm^2, but higher b values produce more susceptibility effects in the head and neck region and so DWI becomes difficult to perform, especially in the skull base. Hence,

this study attempts to use b values only up to 500 s/mm^2 in order to minimize the susceptibility effects. For mapping of ADC, DW images with at least two different b values are required and many studies use the basic technique of employing only two or three b values, such as 0, 500 and 1000 s/mm^2 to produce the ADC maps. In this study, six b values are used for data analysis (0, 100, 200, 300, 400, and 500 s/mm^2) in order to reduce the estimation error in the calculation of ADC.

All examinations were performed on a 1.5T MRI scanner (Intera NT; Philips Medical Systems Best, the Netherlands). The MRI scanner was equipped with a 30 mT/m maximum gradient strength for echo-planar imaging (EPI). A standard head and neck coil was used to include head and neck cancer arising.

DWI employed EPI sequence. Eleven fat-suppressed DW images were acquired in the axial plane using a spin-echo single-shot EPI sequence (repetition time = 2000ms, echo time = 75, section thickness = 4 mm, with no intersection gap, field of view = 23 cm, acquisition matrix = 112 × 112, reconstruction matrix = 256 × 256, number of signals acquired = 4) with six b values of 0, 100, 200, 300, 400, and 500 s/mm^2. A set of ADC maps with 11 sections to include the region of interests (ROIs) was generated for data analysis

Patients also underwent a conventional MR protocol to provide anatomical detail consisting of axial fat-suppressed T2-weighted turbo spin-echo (FS T2W TSE) (repetition time = 2500ms, echo time = 100ms, section thickness = 4mm, with no intersection gap, number of signals acquired = 2), axial T1-weighted spin-echo (T1W SE) (repetition time = 477ms, echo time = 12ms, section thickness = 4 mm, with no intersection gap, number of signals acquired = 2), and contrast-enhanced axial T1W SE (repetition time = 477ms, echo time = 12ms, section thickness = 4mm, with no intersection gap, number of signals acquired = 2) sequences. The contrast agents

were administrated at a dose of 0.1 mmol/kg of gadoterate meglumine (Dotarem; Guerbet, Aulnaysous-Bois, France).

DWI Analysis

Data were reconstructed with the Philips data analysis package (Philips Medical Systems, Best, the Netherlands). ADCs were measured using dedicated software (ViewForum R2.5.3, Philips Medical Systems, the Netherlands).

Lesions greater than 6 mm in minimum diameter were analyzed using conventional MR images as a reference for the anatomical details, and the ROIs of primary tumor and metastatic node were drawn manually on each section in the ADC map and their ADCs were measured. For each tumor ROI, two ADC measurements were taken: (1) ADC of the whole lesion (WL) measurement, for which the ADC value at every tumor section was measured, and the mean ADC was calculated, and (2) ADC of a single representative section (RS) measurement, which was selected to include the largest solid component of the tumor and to exclude any obviously necrotic or cystic regions.

DWI was performed and analyzed using the WL and RS measurement techniques described above. Examples of primary and nodal tumors assessed by DWI are shown in figures 3.1 and 3.2.

Statistical Analysis

A two-tailed non-parametric Mann-Whitney U test was employed to detect any statistically significant difference in the mean ADC between the WL and the RS measurement techniques. For comparing the mean ADC of the primary NPC and nodal metastases, a non-parametric Mann-Whitney U test was also used. A p value

of less than 0.05 was considered to be statistically significantly different. Data were expressed as means ± standard deviation (SD). All statistical analyses were performed using SPSS, version 11.0 (SPSS, Chicago. III).

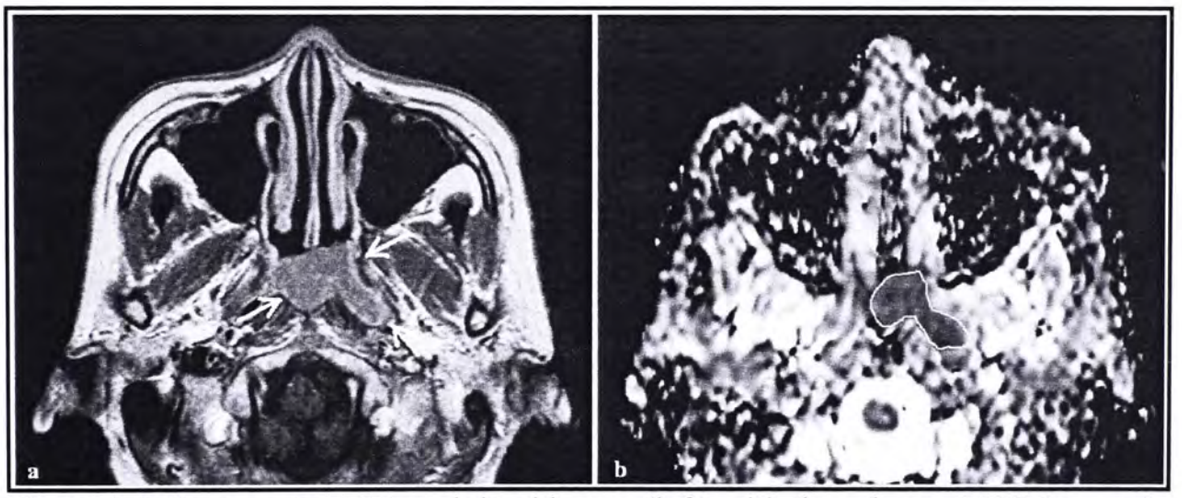

Figure 3.1: Post-contrast T1-weighted image (left) with the primary NPC (arrows) and ADC map (right) with the region of interest drawn around the primary NPC.

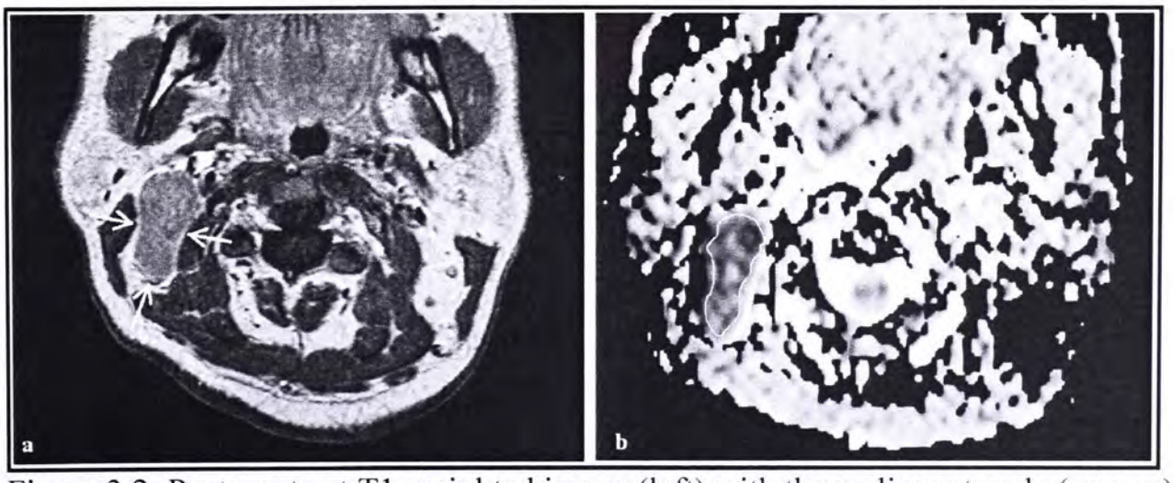

Figure 3.2: Post-contrast T1-weighted image (left) with the malignant node (arrows) and ADC map (right) with the region of interest drawn around the malignant node.

3.2.3 Results

DWI Examinations

DWI was performed in 79 patients (63 men and 16 woman) between 24 and 80 years of age (mean age ± standard derivation = 51 ± 11) with 93 newly diagnosed NPC (primary NPC, n = 65; malignant nodes, n = 28); ADC maps in 22 cases (primary NPC, n = 20; malignant nodes, n = 2) were uninterpretable due to susceptibility artifacts. Hence, the success rate of performing DWI in patients with the primary NPC at the skull base was calculated about 70% (45/65) in this study.

ADC Values of Primary NPC and Nodal Metastases

The average maximum axial diameters for primary NPC and nodal metastases were 4.12 ± 1.21 cm and 1.95 ± 6.32 cm, respectively; the maximum axial diameter range is shown in tables 3.1 and 3.2.

The mean ADC for primary NPC using the WL measurement was $0.985\pm0.157\times10^{-3}$ mm^2/s, whereas the mean ADC using the RS measurement was $0.984\pm0.161\times10^{-3}$ mm^2/s. There was no significant difference in the mean ADC between the WL and RS measurement techniques (p = 0.913, Mann-Whitney U test) (Table 3.1, Figure 3.3)

For nodal metastases, the mean ADC using the WL measurement was $0.885\pm0.105\times10^{-3}$ mm^2/s, whereas the mean ADC using the RS measurement was $0.852 \pm 0.117\times10^{-3}$ mm^2/s. There was no significant difference in the mean ADC between the WL and RS measurement techniques (p = 0.323, Mann-Whitney U test) (Table 3.2, Figure 3.4)

Comparison of the ADC of the primary tumor and nodal metastases

Comparing ADCs of the primary NPC and nodal metastases, the ADC of the primary NPC was higher than the nodal metastases and statistical analysis showed a significant difference between primary NPC and malignant nodes when using both the WL ($p = 0.008$) (Figure 3.5) and the single RS measurement techniques ($p < 0.001$) (Figure 3.6).

	Measurement technique for primary NPC	
Measurement/ Statistical values	Whole Lesion (WL)	Representative Section (RS)
Mean ADC ± SD × 10^{-3} mm^2/s	0.985 ± 0.157	0.984 ± 0.161
Range of ADC × 10^{-3} mm^2/s	0.59 – 1.31	0.62 – 1.34
Average maximum axial diameter ± SD (range) cm	4.12 ± 1.21 (1.64 – 7.31)	
p-value	0.913	

Table 3.1: Primary NPC with mean and range of ADC, tumor size and p-value.

	Measurement technique for nodal metastasis	
Measurement/ Statistical values	Whole Lesion (WL)	Representative Section (RS)
Mean ADC ± SD × 10^{-3} mm^2/s	0.885 ± 0.105	0.852 ± 0.117
Range of ADC × 10^{-3} mm^2/s	0.67 – 1.08	0.63 – 1.03
Average maximum axial diameter ± SD (range) cm	1.95 ± 6.32 (1.02 – 3.34)	
p-value	0.323	

Table 3.2: Nodal metastasis with mean and range of ADC, tumor size and p-value.

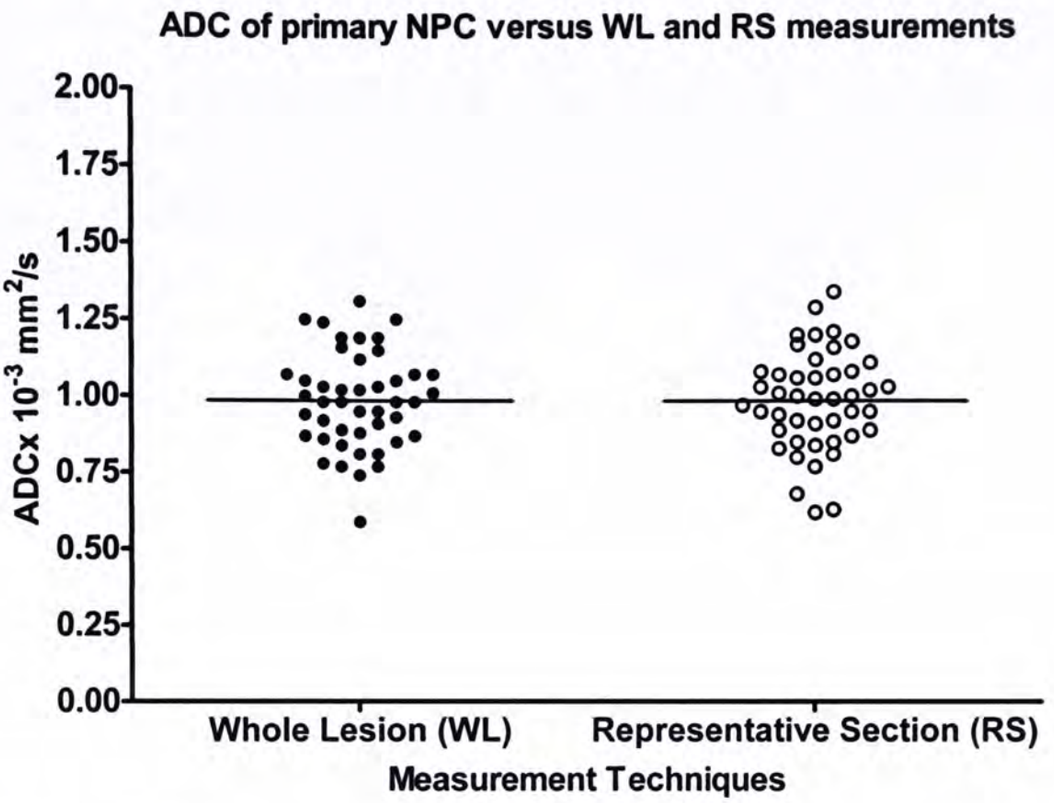

Figure 3.3: A plot of ADC of primary NPC versus WL and RS measurement techniques (p = 0.913).

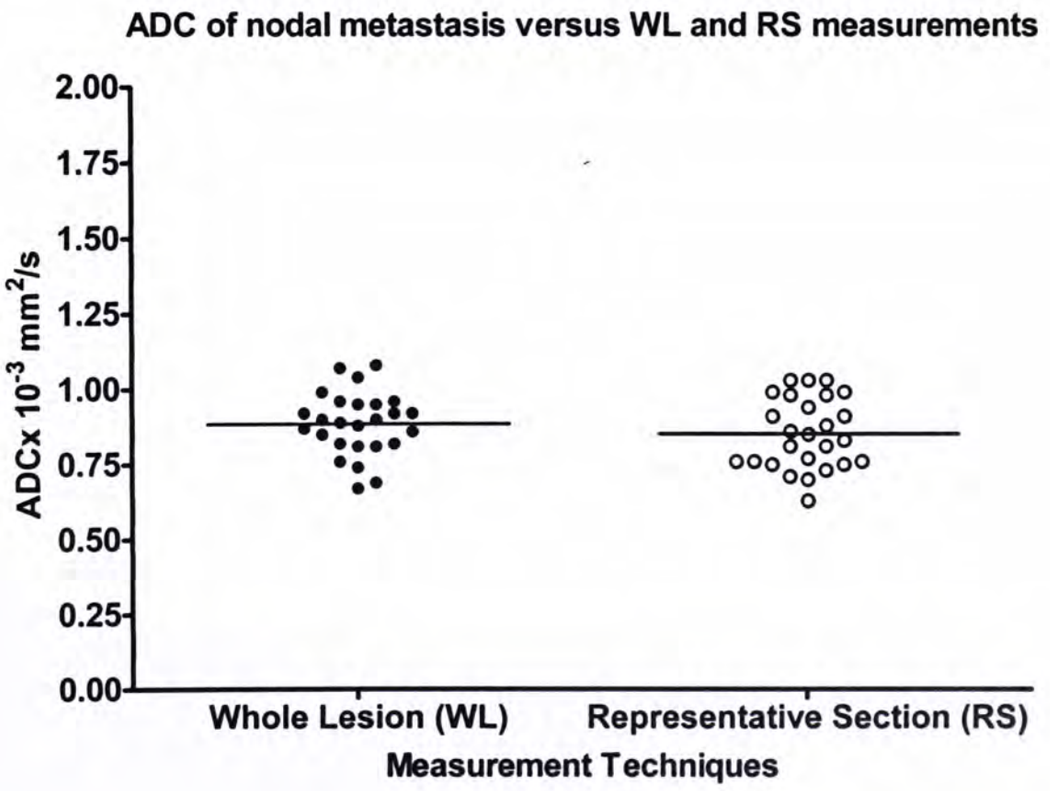

Figure 3.4: A plot of ADC of nodal metastasis versus WL and RS measurement techniques (p = 0.323).

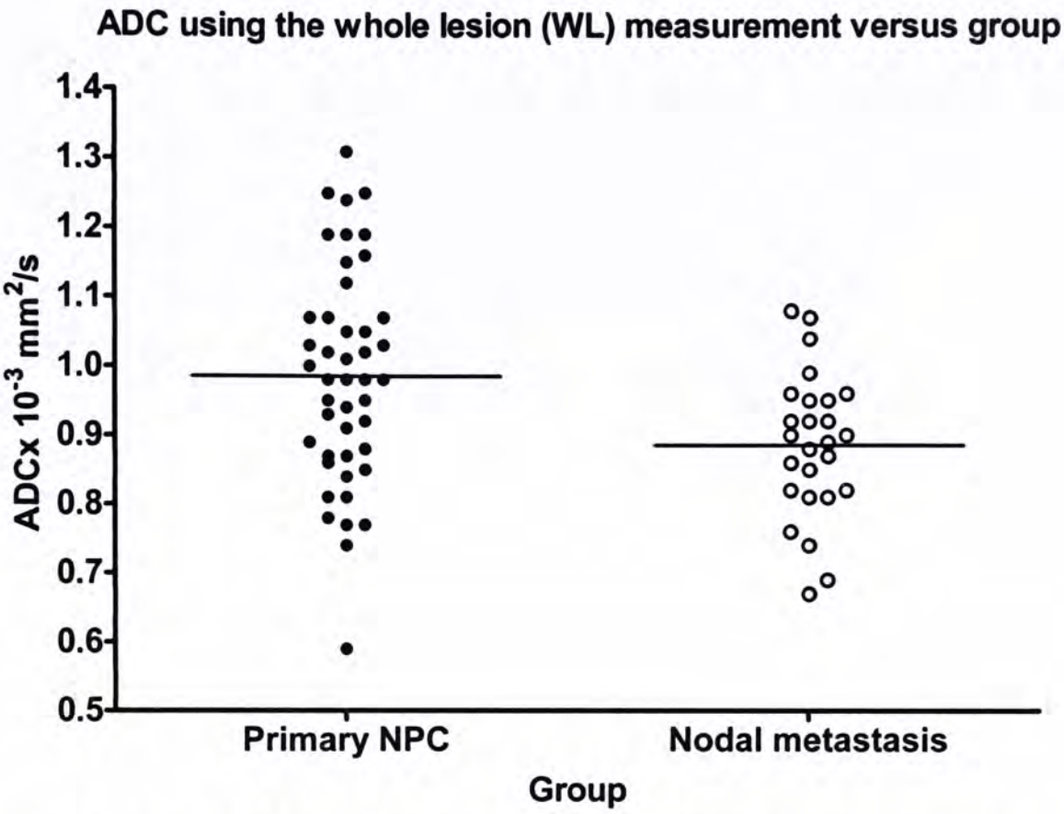

Figure 3.5: A plot of ADC using the whole lesion (WL) measurement of primary NPC and nodal metastasis ($p = 0.008$).

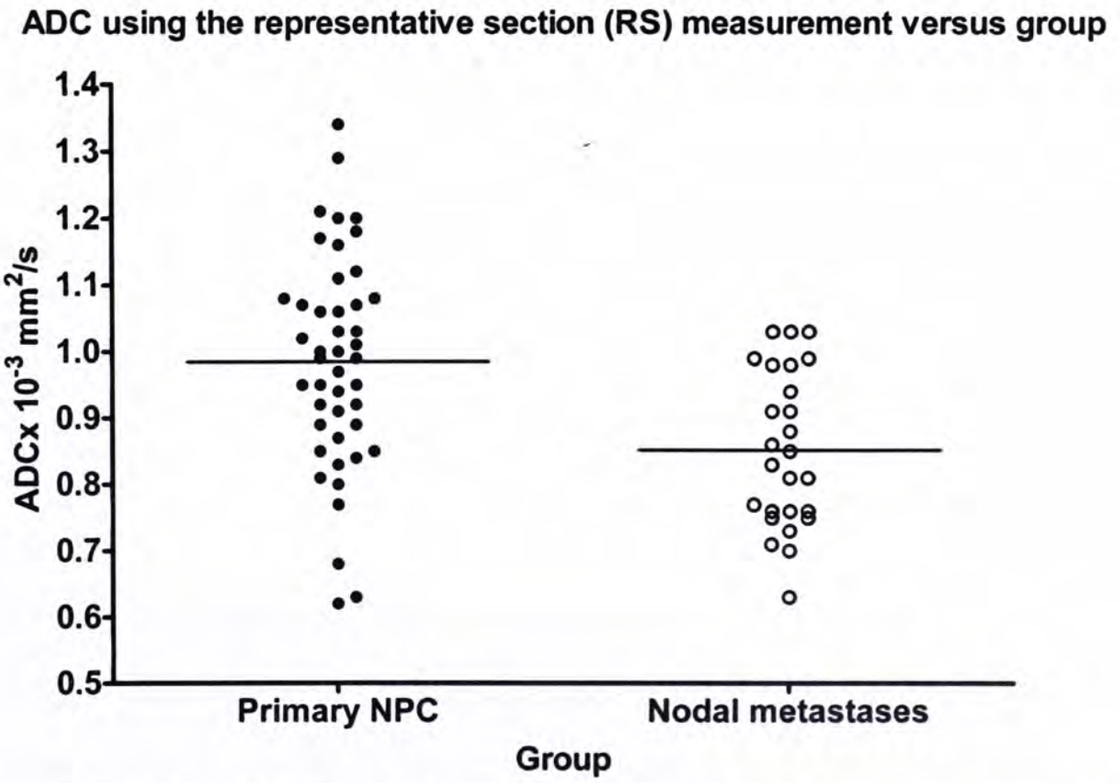

Figure 3.6: A plot of ADC using the representative section (RS) measurement versus primary NPC and nodal metastasis ($p < 0.001$).

3.2.4 Discussion

Diffusion-weighted imaging of head and neck has been used in the diagnosis of head and neck lesions (Abdel Razek, A. A. *et al.*, 2006; Friedrich, K. M. *et al.*, 2008; Kawai, Y. *et al.*, 2005; Misa Sumi, Noriyuki, 2003; Sumi, M. *et al.*, 2002; Sumi, M. *et al.*, 2006; Wang, J. *et al.*, 2001; Yoshino, N. *et al.*, 2001), evaluation of residual or recurrent tumors (Aikele, P. *et al.*, 2003; Dubrulle, F. *et al.*, 2006; Vandecaveye, V. *et al.*, 2006) as well as the assessment of tumor response to chemoradiotherapy (Vandecaveye, V. *et al.*, 2007). Previous studies have demonstrated that the utility of ADC for differentiating between benign and malignant cervical lymph nodes (de Bondt, R. B. *et al.*, 2009; Holzapfel, K. *et al.*, 2009), lymphomas from carcinomas in the head and neck (Maeda, M. *et al.*, 2003; Sumi, M. *et al.*, 2007), and cysts from head and neck tumors (Sakamoto, J. *et al.*, 2009). It has also been evaluated for predicting tumor response to neoadjuvant therapy for head and neck squamous cell carcinomas (HNSCC) (Kato, H. *et al.*, 2009), and for differentiating residual or recurrent head and neck tumors from post-radiation or post-surgical changes (Abdel Razek, A. A. *et al.*, 2007). Recent studies suggest that ADC can be used as a marker for prediction and early detection response to concurrent chemoradiation therapy in HNSCC (Kim, S. *et al.*, 2009).

Using the technique adapted to the head and neck which is described in the methods section, it was found that DWI is a feasible technique for examining NPC, not only in neck nodes, but also in the primary tumor which lies at the challenging site of the skull base. DWI was successfully performed in primary tumors in 70% of cases but it was degraded in 30% of cases by susceptibility artifacts resulting from local magnetic field variations at air-tissue interfaces in the region of the skull base. The ADC value for the primary tumor lies $0.985 \pm 0.157 \times 10^{-3}$ mm^2/s for using the whole

lesion (WL) measurement technique and $0.984 \pm 0.161 \times 10^{-3}$ mm^2/s for using the representative section (RS) measurement technique. There was no statistically significant difference in the ADC value when calculating the ADC from all sections through the whole lesion compared to just using a single section taken at the level of the largest solid tumor. This is probably because most primary tumors are homogeneous and non-necrotic so using a single RS measurement technique can provide an accurate method of assessing ADC but in a more effective way which takes less time to draw the ROI and analyze the data.

For nodal tumors there was an even higher success rate for DWI of about 93% (26/28) because of less problems with susceptibility effects. The ADC values using the WL and the RS measurement techniques for nodal metastases were $0.885 \pm 0.105 \times 10^{-3}$ mm^2/s and $0.852 \pm 0.117 \times 10^{-3}$ mm^2/s, respectively. Using these two measurement techniques, also there was no statistically significant difference in the ADC value. This is because not many necrotic nodes were involved in this study. Hence, the result in the calculation of ADC from all sections through the whole lesion was similar to that from a single section selected to exclude any obviously necrotic or cystic regions and include the largest solid component of the nodal tumor. However, taking the measurement from whole lesion could theoretically lead to error in lymph nodes with extensive necrosis, because necrotic or cystic areas tend to produce higher ADC values compared to non-necrotic areas. The ADC of nodal metastases was found to be statistically significantly lower than that of the primary tumor. The cause for this is uncertain but possibilities include the influence of the underlying normal nodal architecture on ADC or biological changes in the tumor when it spreads from the primary site to the neck node.

This study had some limitations. First, perfusion in tumor tissue can have greater influence on DWI obtained with low b-values (b =0, 30, and 100 s/mm^2) hence may contribute to the ADC calculation. In this study, the ADC values of the tumors were therefore calculated using a relatively high b-value (500 s/mm^2) to reduce the contribution of the perfusion factor. Second, micronecrosis may have been included in ROIs because it was undetected by conventional MRI. However, the necrotic foci are probably too small to contribute to the changes in ADC values of the tumors. The ability of DWI to assess the primary tumors and nodal metastases and to produce an ADC value provides the foundation for using ADC to differentiate NPC from other head and neck cancers. It also provides the potential for ADC to be used in the future to monitor treatment response to chemoradiotherapy.

3.3 DWI of Primary Tumors: Comparison of NPC with Squamous Cell Carcinoma and Extra-nodal Non-Hodgkin Lymphoma

3.3.1 Introduction and Objectives

Nasopharyngeal carcinoma (NPC), squamous cell carcinoma (SCC) and extra-nodal non-Hodgkin lymphoma (NHL) are common primary malignancies of the head and neck in Hong Kong. They may all present as a primary tumor in the nasopharynx or as a metastatic lymph node in the neck. The results from the previous study show that the ADC value of NPC seems to lie in a narrow range and therefore by using ADC values of the tumor DWI has the potential to be used as a diagnostic tool to distinguish between these three primary site cancers.

The aim of this study was therefore to determine if there are any significant differences between the ADC values of these three cancers.

3.3.2 Methods

Patient Selection and DWI

Patients with histologically confirmed undifferentiated nasopharyngeal carcinomas (NPC), squamous cell carcinomas (SCC), and extra-nodal non-Hodgkin lymphomas (NHL) were recruited and underwent DWI according to the methods in section 3.2.2 above. Analysis of the primary tumor site was performed using the RS technique also described in section 3.2.2

Statistical Analysis

Statistical tests were performed to detect any difference between subject groups. A non-parametric Kruskal-Wallis test was used to detect any statistically significant difference in the mean ADC between three subject groups, such as NPC, SCC, and NHL. If a statistically significant difference ($p < 0.05$) was found, a two-tailed non-parametric Mann-Whitney U test with Bonferroni correction was used to assess difference among the three groups, and a p-value of less than 0.05 was considered statistically significant. When a significant difference was found between each pair in the subject groups, receiver operating characteristic (ROC) analysis was employed to investigate the discriminatory capability of the ADC value for distinguishing each pair. Sensitivity and specificity were assessed by the ROC, to determine optimal sensitivity and specificity. The value that corresponded to a specificity of 100% with maximized sensitivity was also evaluated. Data were expressed as means ± standard deviation (SD). All statistical analyses were performed using SPSS, version 11.0 (SPSS, Chicago. III).

3.3.3 Results

DWI Examinations

100 consecutive patients (85 men, 15 women) with newly diagnosed head and neck cancers (NPC, n = 65; SCC, n =28; NHL, n =7) at a primary site were recruited in this prospective study, of which 24 patients (NPC, n = 20; SCC, n = 2; NHL, n = 2) were excluded because images obtained were degraded by artifact (a flowchart shown in figure 3.7). This study included 76 patients (64 men and 12 women) between 26 and 79 years of age (mean age ± standard derivation = 53 ± 11) with head and neck cancers (NPC, n = 45; SCC, n = 26; NHL, n = 5).

ADC Values of NPC, SCC and NHL

The mean ADC values of primary NPC, SCC and NHL were $0.984\pm0.161\times10^{-3}$ mm^2/s, $1.14\times10^{-3}\pm0.196$ mm^2/s and $0.746\pm0.192\times10^{-3}$ mm^2/s, respectively. The SD and range of the ADC and the average and range of the maximum axial diameter are shown in table 3.3 and examples of the three cancers are shown in figures 3.8 - 10.

Head and neck Cancer/ Statistical Analysis			
Group	NHL (n = 5)	Mean ADC ± SD (Range) $\times10^{-3}$ mm^2/s	0.746 ± 0.192 (0.723 - 0.767)
		Average maximum axial diameter (Range) cm	3.4 ± 0.80 (2.11 – 4.09)
	NPC (n = 45)	Mean ADC ± SD (Range) $\times10^{-3}$ mm^2/s	0.984 ± 0.161 (0.617 – 1.34)
		Average maximum axial diameter (Range) cm	4.12 ± 1.21 (1.64 – 7.31)
	SCC (n = 26)	Mean ADC ± SD (Range) $\times10^{-3}$ mm^2/s	1.14 ± 0.196 (.79 – 1.51)
		Average maximum axial diameter (Range) cm	4.36 ± 1.64 (1.92 – 9.48)

Table 3.3: The ADC values for each group.

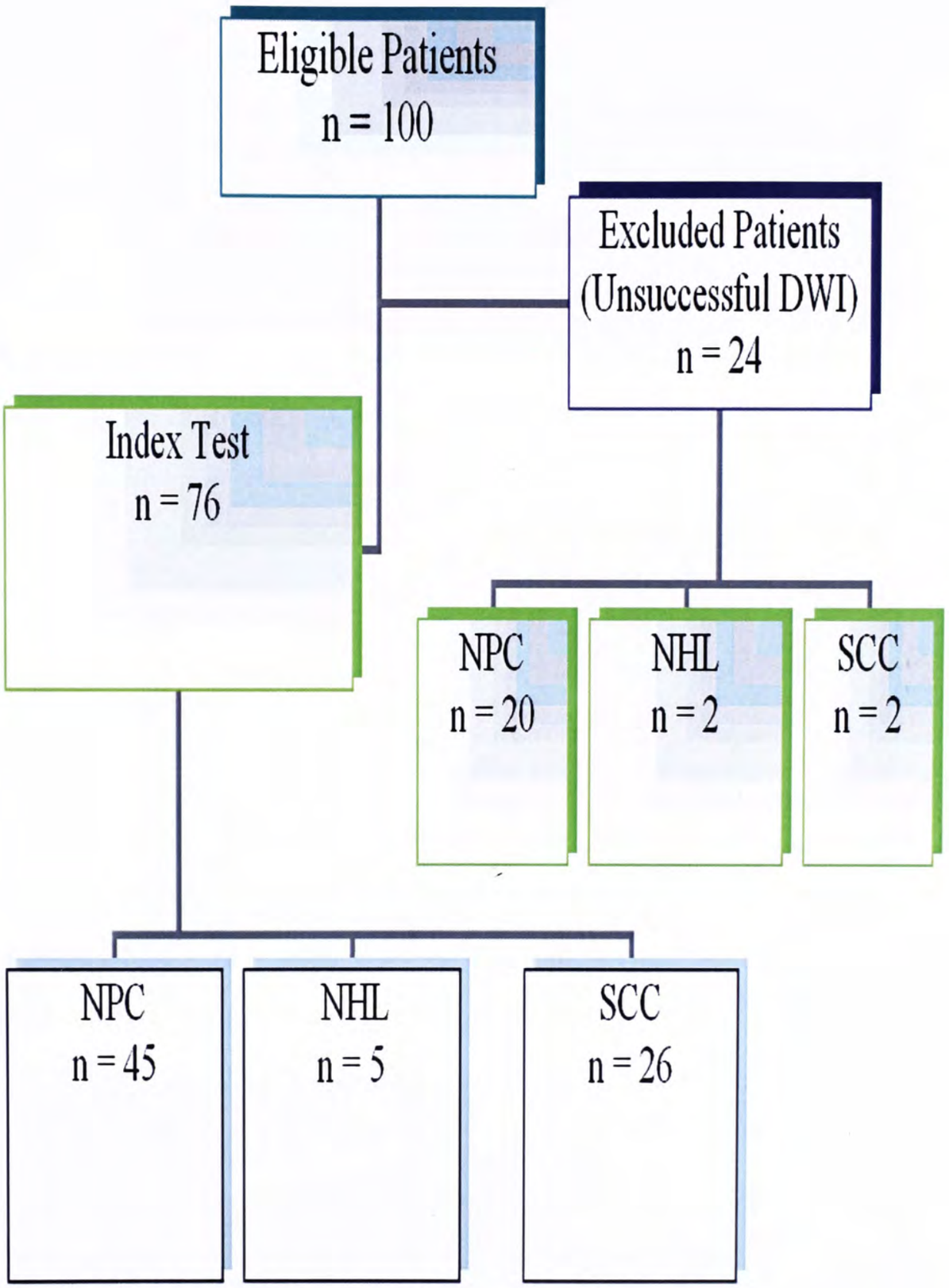

Figure 3.7: A flowchart of patients with head and neck cancers.

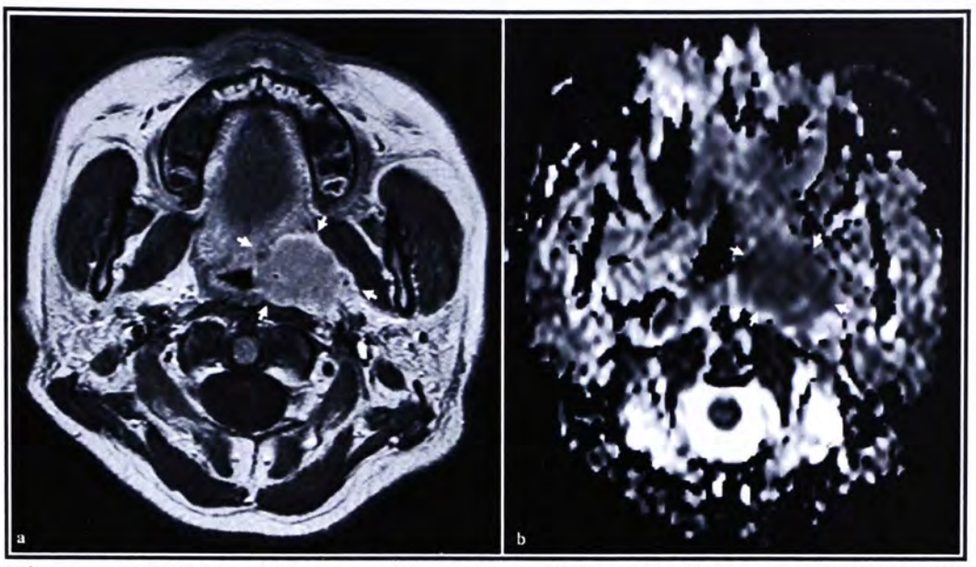

Figure 3.8: Primary NPC in a 38-year-old woman. The axial post-contrast T1W MR image (left) and ADC map (right) show a primary tumor (arrows) with the ADC value of $0.990 \pm 0.169 \times 10^{-3}$ mm^2/s.

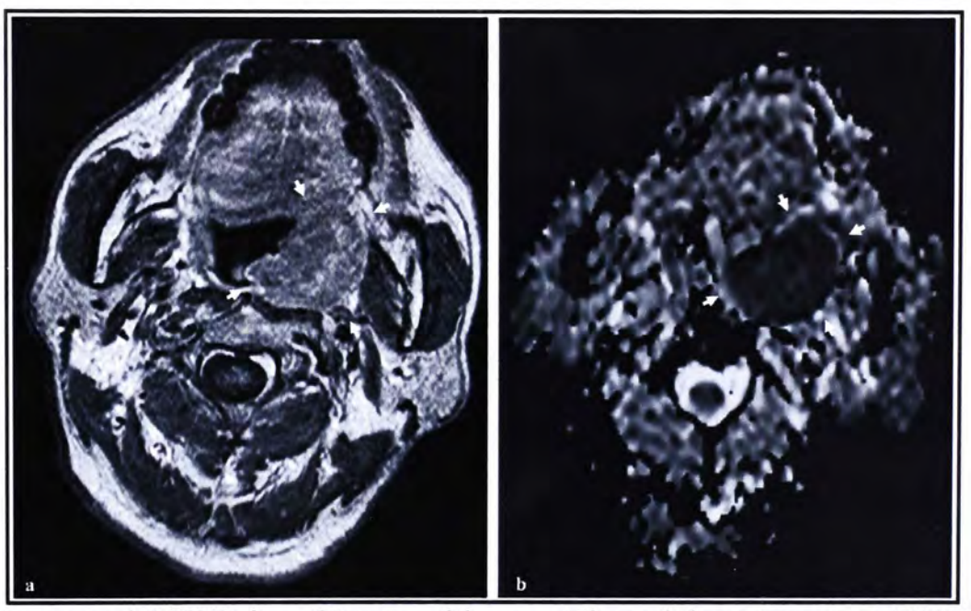

Figure 3.9: Extra-nodal NHL in a 65-year-old man. The axial post-contrast T1W MR image (left) and ADC map (right) show the primary tumor (arrows) with ADC value of $0.736 \pm 0.201 \times 10^{-3}$ mm^2/s.

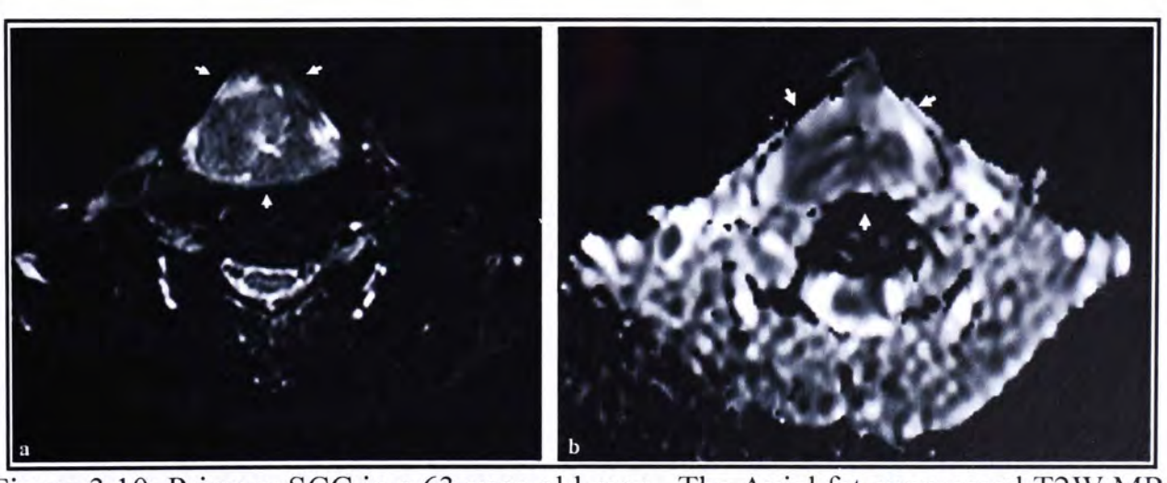

Figure 3.10: Primary SCC in a 63-year-old man. The Axial fat-suppressed T2W MR image (left) and ADC map (right) show the primary tumor (arrows) with ADC value of $1.10 \pm 0.324 \times 10^{-3}$ mm^2/s.

Comparison of the ADC Values of the Three Cancers

Results of statistical analysis showed a significant difference in the mean ADC ($p < 0.001$, Kruskal-Wallis test) between NPC, NHL and SCC. When comparing each pair, the mean ADC of NHL was significantly lower than that of NPC ($p = 0.002$) and SCC ($p < 0.001$), and the mean ADC of NPC were significantly lower ($p = 0.003$) than that of SCC (Figure 3.11, Table 3.4).

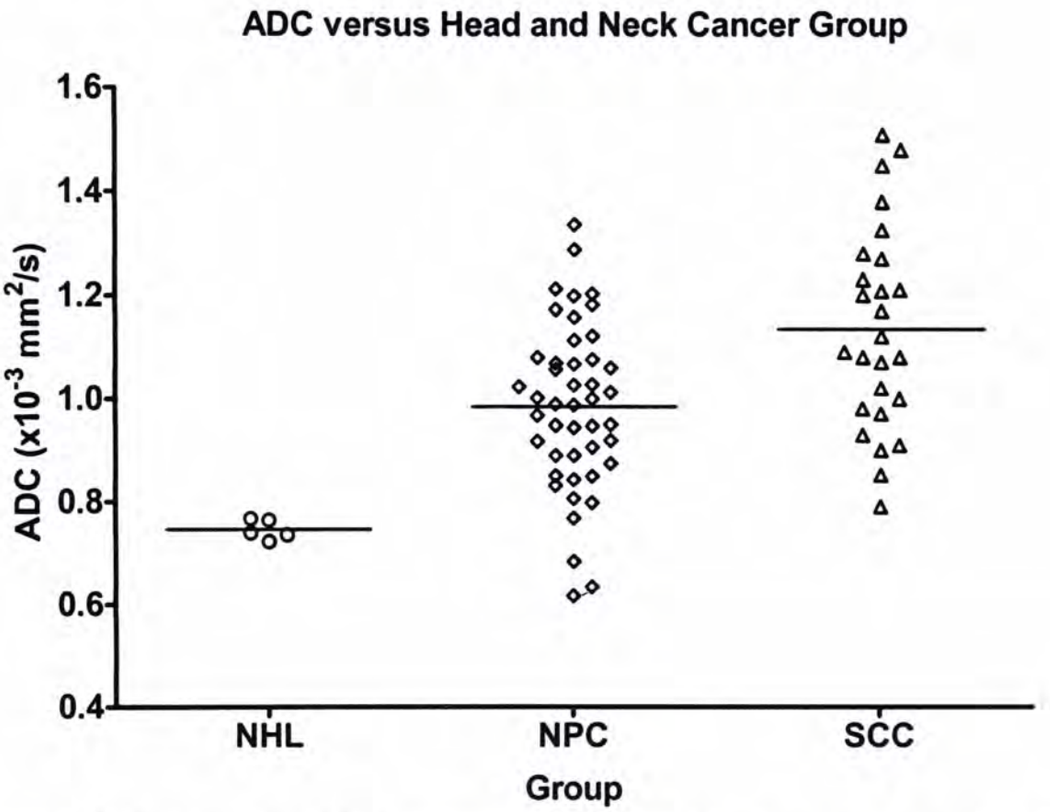

Figure 3.11: A plot of the ADC versus each head and neck cancer group ($p < 0.001$, Kruskal-Wallis test). The horizontal lines near the middle of the box represent median.

Results of Mann-Whitney U test with Bonferroni correction

Comparison of cancer groups			p-value
NPC	versus	NHL	0.002
NPC	versus	SCC	0.003
SCC	versus	NHL	<0.001

Table 3.4: Non-parametric Mann-Whitney U test with Bonferroni correction for paired group comparisons of ADC values

Results from ROC Analysis

The optimal ADC threshold value for distinguishing between SCC and NHL, between NPC and SCC, and between NHL and NPC was 0.779×10^{-3} mm^2/s, 1.07×10^{-3} mm^2/s, and 0.768×10^{-3} mm^2/s, respectively, when we optimized both sensitivity and specificity (Figures 3.12 - 14, Table 3.5).

In order to improve specificity, the results were re-evaluated to produce a threshold with a specificity of 100% while maximizing the sensitivity for discrimination between SCC and NHL, SCC and NPC, and NPC and NHL (Table 3.6). The following results were found.

1) The ADC threshold for the differentiation of SCC from NHL was 0.779×10^{-3} mm^2/s which produces a sensitivity of 100%.
2) The ADC value of SCC for the prediction of differentiation from NPC was > 1.36×10^{-3} mm^2/s which produces a sensitivity of 15.4%. The ADC value of NPC for the prediction of differentiation from SCC was < 0.779×10^{-3} mm^2/s which produces a sensitivity of 8.9%.
3) The ADC value of NPC for the prediction of differentiation from NHL was > 0.768×10^{-3} mm^2/s which produces a sensitivity of 93.3%. No suitable ADC value was obtained to distinguish NHL from NPC because specificity can not reach to 100%.

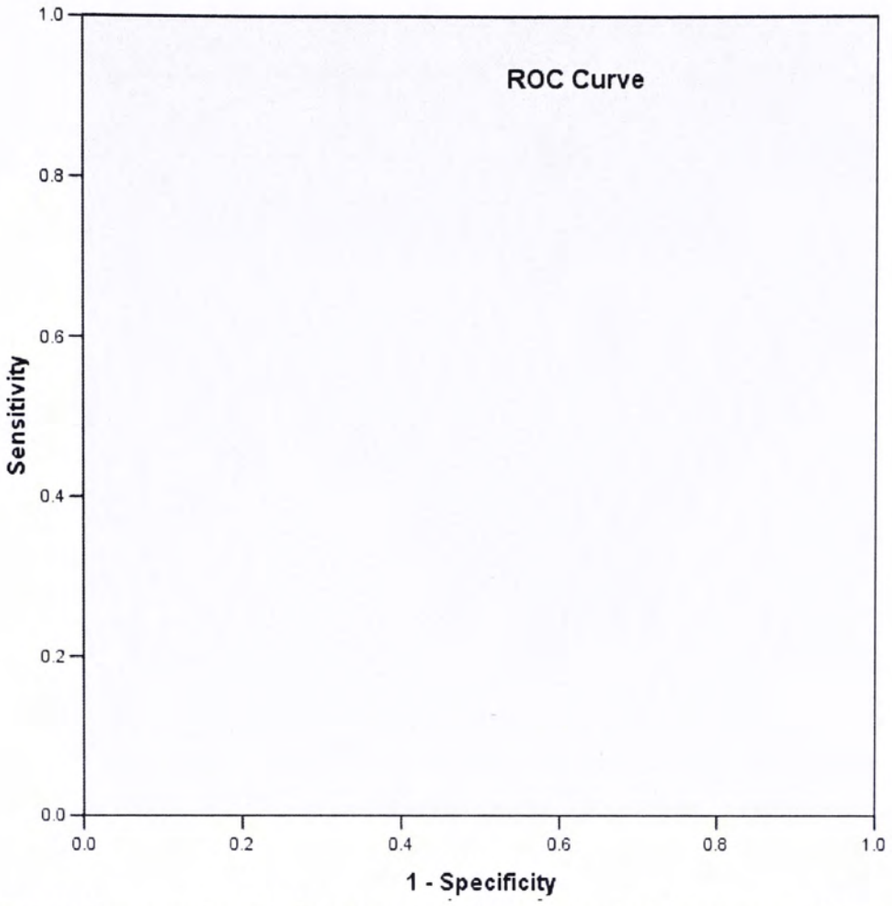

Figure 3.12: ROC curve for ADC value for discrimination between SCC and NHL.

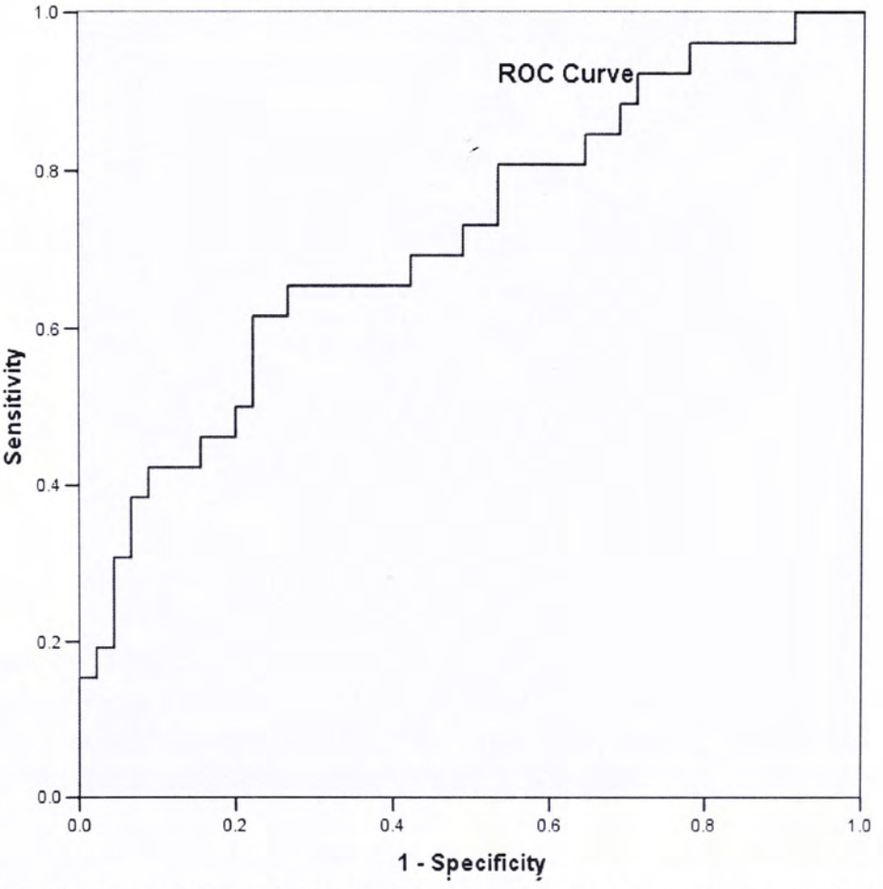

Figure 3.13: ROC curve for ADC value for discrimination between SCC and NPC.

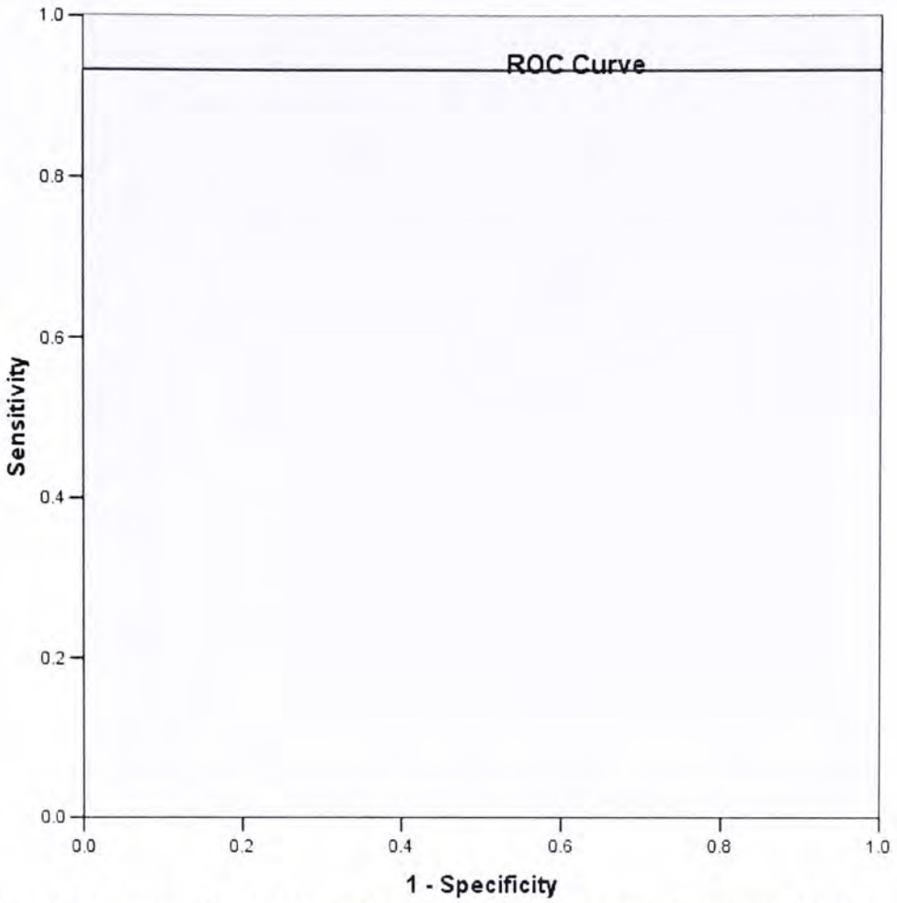

Figure 3.14: ROC curve for ADC value for discrimination between NPC and NHL.

Comparison	AUC (95% CI)	Optimal ADC threshold ($\times 10^{-3}$, mm^2/s)	SE	SP	PPV	NPV
SCC vs. NHL	1.00 (1.00 - 1.00)	0.779[a]	100%	100%	100%	100%
	1.00 (1.00 - 1.00)	0.779[b]	100%	100%	100%	100%
NPC vs. SCC	0.716 (0.589– 0.843)	1.07[c]	65.4%	73.3%	59%	79%
	0.716 (0.589– 0.843)	1.07[d]	73.3%	65.4%	79%	59%
NPC vs. NHL	0.93 (0.86–1.00)	0.768[e]	93.3%	100%	100%	63.0%
	0.93 (0.86–1.00)	0.768[f]	100%	93.3%	63.0%	100%

Table 3.5: The optimum ADC threshold values for distinguishing between SCC and NHL, SCC and NPC, and NPC and NHL with the optimal sensitivity and specificity.
Note. — AUC = area under curve, CI = confidence interval, SE = sensitivity, SP = Specificity, PPV = positive predictive value, NPC = negative predictive value.
[a] ADC values greater than the ADC threshold show stronger evidence for SCC.
[b] ADC values less than the threshold show stronger evidence for NHL.
[c] ADC values greater than the threshold show stronger evidence for SCC.
[d] ADC values less than the threshold show stronger evidence for NPC.
[e] ADC values greater than the threshold show stronger evidence for NPC.
[f] ADC values less than the threshold show stronger evidence for being NHL.

Comparison		Cut off ADC value at a specificity of 100% ($\times 10^{-3} mm^2/s$)	SE	SP	PPV	NPV
SCC vs. NHL	Predicting SCC	0.779[a]	100%	100%	100%	100%
	Predicting NHL	0.779[b]	100%	100%	100%	100%
NPC vs. SCC	Predicting SCC	1.36[a]	15.4%	100%	100%	67%
	Predicting NPC	0.779[c]	8.9%	100%	100%	39%
NPC vs. NHL	Predicting NPC	0.768[d]	93.3%	100%	100%	63%
	Predicting NHL	100% specificity unavailable (No suitable cutoff)				

Table 3.6: The cut-off ADC values for distinguishing between SCC and NHL, SCC and NPC, and NPC and NHL with a specificity of 100% and maximum sensitivity. Note. — AUC = area under curve, CI = confidence interval, SE = sensitivity, SP = Specificity.

[a] ADC values greater than the ADC threshold show stronger evidence for SCC.

[b] ADC values less than the threshold show stronger evidence for NHL.

[c] ADC values less than the threshold show stronger evidence for SCC.

[d] ADC values greater than the threshold show stronger evidence for NPC.

3.3.4 Discussion

The objectives of this study were to evaluate the utility of ADC of undifferentiated nasopharyngeal carcinoma (NPC) as a diagnostic tool to distinguish this cancer from SCC and NHL which are two other common cancers in the head and neck in our study population. This in vivo DWI study demonstrated a statistically significant difference in the ADC among the three subject groups of primary cancers. The ADC value of NPC was found to lie between that of NHL and SCC with a progressive increase in ADC from NHL to NPC to SCC. The difference in ADC values may be caused by factors such as cellularity, necrosis and perfusion. Cellularity is probably the most important factor that influences water diffusivity in tumors. There are studies that have demonstrated a close correlation between ADC and cellularity in tumors (Guo, A. C. *et al.*, 2002). Cancers with greater cellularity and less extra-cellular space have a greater restriction of diffusion and lower ADC. Lymphomas are tumors that are especially cellular and compact, which would account for this tumor having the lowest ADC value out of the three cancers in this study. Necrosis

may be another factor that influences water diffusivity in tumors. Good correlation between ADC and necrotic fraction of tumor has been shown (Lyng, H. *et al.*, 2000); the tumors with high necrotic fraction had relatively high ADC value compared to tumors with low necrotic fraction. However, this may not have accounted for the differences in this study because the necrotic portion of tumors was excluded from the ROI measurement in the RS measurement technique. Perfusion is a further possible factor that may contribute to the ADC. With b values less than 100 s/mm^2, perfusion can influence ADC by producing pseudo-diffusion coefficient, although once again in this study by using a plot of from six diffusion weighted images this effect should have been minimal.

Other studies have revealed a significantly lower ADC in lymphoma compared to SCC and these studies also highlighted the potential of using DWI for tumor characterization (Maeda, M. *et al.*, 2005; Sumi, M. *et al.*, 2007). The mean ADC values of this study appear to be consistent with those reported by Maeda et al. studies (Maeda, M. *et al.*, 2005) (mean ADC values were $0.96\pm0.11\times 10^{-3}$ mm^2/s for SCC and $0.65\pm0.09\times 10^{-3}$ mm^2/s for lymphomas) and by Sakamoto et al. studies (mean ADC values were $1.38\pm0.42\times 10^{-3}$ mm^2/s for SCC and $0.80\pm0.12\times 10^{-3}$ mm^2/s for lymphomas). In this study, no overlap was found in the ADC value for SCC and NHL and according to the ROC results, an ADC value of greater than 0.779×10^{-3} mm^2/s could be used to identify SCC, whereas an ADC value of less than 0.779×10^{-3} mm^2/s could be used to identify NHL, with 100% of specificity and sensitivity values. These thresholds may be beneficial in centers where the main differential diagnosis of malignant lymphadenopathy lies between these two cancers.

The mean ADC of NPC was found to lie between that of SCC and NHL, but in order to produce a clinically useful diagnostic tool (by setting a high specificity without too

much compromise of sensitivity) a threshold could only be found to determine NPC from NHL but not from SCC.

In conclusion, the ADC values were significantly different between primary NPC, SCC and extra-nodal NHL. In a clinical setting, thresholds could be determined to distinguish SCC with a high ADC, from lymphoma with a low ADC. Thresholds could also be determined to distinguish NPC from NHL but not from SCC.

3.3.5 Summary of DWI in Head and Neck Cancer

Using the technique described in this thesis, DWI is found to be a feasible technique for examining head and neck cancers, even in the difficult site of the skull base. The ADC values of primary and nodal NPC have been documented ($0.984 \pm 0.161 \times 10^{-3}$ mm^2/s and $0.852 \pm 0.117 \times 10^{-3}$ mm^2/s, respectively) and the single representative section measurement technique, which is quicker and easier to perform than the whole lesion measurement technique, has been shown to produce similar results in non necrotic tumors. The ADC value of NPC lies between that of SCC and NHL and the study has shown significant differences in the ADC of these three cancers. The study also shows that DWI can be used to produce clinically useful thresholds which may be helpful in distinguishing primary NPC from NHL but not from SCC. The results also confirm previous studies which show clinically useful differences between NHL and SCC.

Chapter 4: Chemical shift imaging of head and neck tumors

4.1 Introduction – Single Voxel Spectroscopy and Chemical Shift Imaging

Magnetic resonance spectroscopy is a non-invasive technique which provides information on cellular metabolism. Proton MRS (^{1}H-MRS) can detect a wide variety of proton-containing metabolites in tumors and has been used to evaluate cancers of brain, breast, prostate, colon, cervix, pancreas, ovary, and thyroid (Ian C.P. Smith and Stewart, Laura C., 2002; Shah, N. *et al.*, 2006). Previous MRS studies have shown that a common feature of many cancers is an increased choline-containing compounds (Cho) level (Lee, J. *et al.*, 2004). Cho appears to be elevated in squamous cell carcinoma of the head and neck (HNSCC) (Bisdas, S. *et al.*, 2007; Maheshwari, S. R. *et al.*, 2000; Mukherji, S. K. *et al.*, 1997; Mukherji, S. K. *et al.*, 1996; Shah, N. *et al.*, 2006) and is known to be a constituent of the membrane lipids. In proliferating malignant tissue, elevated Cho level may serve as an active marker for cellular proliferation (Mukherji, S. K. and Gerstle, R. J., 1998) and the persistence of Cho may also serve as a biomarker for residual cancer in a post-treatment mass (King, A. D. *et al.*, 2009). The results of ^{1}H-MRS studies using single voxel spectroscopy (SVS) to assess head and neck tumors have shown that ^{1}H-MRS have some diagnostic value for the diagnosis and follow-up of disease processes as well as for the evaluation of physiological condition (Star-Lack, J. *et al.*, 1998; Star-Lack, J. M. *et al.*, 2000; Wei Huang *et al.*, 2000). However, this SVS technique has two main drawbacks. Firstly, SVS only produces a spectrum, rather than an image, and so is deemed less favorable in routine clinical practice. Secondly,

it provides little information regarding the spatial distribution of Cho in large heterogeneous lesions, which could be useful to guide biopsy or to identify recurrent disease following treatment. Chemical shift imaging (CSI), on the other hand, has the potential to overcome these drawbacks. CSI uses multi-voxel spectroscopy (MVS) technique to acquire spectra from multiple adjacent voxels and it can provide a much larger volume of interest (VOI) covering the whole lesion. Hence, CSI can generate images of the distribution and level of Cho metabolite within a large lesion, which could provide valuable information for treatment planning by directing higher does of radiation to these regions where Cho is most elevated. In addition, CSI is useful to examine cancer or post-treatment residual mass to display areas of high choline concentration, commonly referred to as "hot-spots".

Proton chemical shift imaging (^{1}H-CSI) has been established and applied to the brain, breast and prostate (Hermann, E. J. *et al.*, 2008; Hricak, H., 2005; Jacobs, M. A. *et al.*, 2004). Several brain studies using MVS technique have shown that it can be used to characterize gliomas based on changes in metabolite levels (De Stefano, N. *et al.*, 1998; Furuya, S. *et al.*, 1997; Hermann, E. J. *et al.*, 2008). These studies have demonstrated that gliomas exhibit a reduction in N-acetylaspartate (NAA) and creatine (Cr), and an increase in choline (Cho), suggesting increased Cho/NAA and/ or Cho/Cr ratios associated with higher tumor grade. Because many gliomas are heterogeneous tumors, ^{1}H-CSI with choline hot spots are helpful to guide biopsy to find sites of high-grade tumor (McKnight, T. R. *et al.*, 2007; Son, B. C. *et al.*, 2001). ^{1}H-CSI has also been shown to be useful for the radiation treatment planning and follow-up of gliomas (Narayana, A. *et al.*, 2007; Nelson, S. J. *et al.*, 2002) as well as for the detection of recurrent disease and post-radiation changes (Narayana, A. *et al.*, 2007; Sundgren, P. C. *et al.*, 2009). For breast tumors, ^{1}H-MRS studies have shown

that increased Cho are generally detected by ^{1}H-MRS in breast cancers whereas in normal breast tissue and benign lesions, Cho are generally low and undetectable (Sardanelli, F. *et al.*, 2009). These findings can help to differentiate normal from abnormal breast tissue in patients with breast cancer. The first feasibility study of evaluating breast lesions with CSI technique was reported by Jacobs et. al. in 2004 (Jacobs, M. A. *et al.*, 2004) and subsequent studies have confirmed that this CSI technique is applicable in a routine clinical setting (Baek, H. M. *et al.*, 2008).

For prostate cancer, ^{1}H-MRS can detect changes in concentrations of citrate (Cit), creatine (Cr) and choline (Cho). Studies have shown that aggressive and higher grade tumors exhibit a relative augmentation of Cho level and reduction of Cit level, implying that the choline+creatine/citrate ratio ([Cho+Cr]/Cit) correlating with the Gleason grade can be helpful to predict prostate cancer aggressiveness (Swindle, P. *et al.*, 2003; Zakian, K. L. *et al.*, 2005). In clinical practice, combined MRI and ^{1}H-CSI can be useful for the pretreatment assessment of prostate cancer aggressiveness (Hricak, H., 2005).

In the head and neck region, single voxel ^{1}H-MRS studies have demonstrated increased levels of choline and lactate in cancers (Bisdas, S. *et al.*, 2007; Mukherji, S. K. *et al.*, 1997; Star-Lack, J. *et al.*, 1998). However, because of some inherent problems of performing CSI in the neck, this CSI technique has not been performed on head and neck tumors. The main challenges of performing CSI in the head and neck region are an inhomogeneous static magnetic field that affects the performance of CSI because of large susceptibility differences in the skull-base that cause difficulties in shimming. It is therefore necessary to develop a method to improve CSI, so that it can produce spectroscopy data of sufficiently high quality to allow it to be used as a research and clinical tool.

4.2 CSI – Methods Used to Reduce Magnetic Field Inhomogeneity

Anti-susceptibility Device

One method to improve magnetic field homogeneity in the head and neck region is placed by employing an anti-susceptibility device filled with a tissue-like material placed behind and around the neck (Figure 4.1). This type of device is usually known as sat pads filled with tissue-like material which has a magnetic susceptibility similar to that of human tissue. Some tissue-like materials that have magnetic susceptibility similar to human tissue (Schenck, J. F., 1996) are listed in Table 4.1. Studies have demonstrated that water bags or sad pads filled with industrial grade silica (SiO2) are useful to improve fat saturation in the air-tissue interface of the neck and to reduce the susceptibility-induced artifacts (R. M. Varek and C. Guclu, 2005), but at present they are not commercially available. On the other hand, sat pads filled with a liquid perfluorocarbon (PFC) (Sat Pad, Magmedix, Inc.) are commercially available and have been used to improve local magnetic field homogeneity and fat saturation of the neck and to improve the quality of MR images of the neck and cervical spine (Choi, H. and Ma, J., 2008). In this CSI study, sat pads filled with a liquid PFC (Figure 4.2) were used as an attempt to improve the local magnetic field homogeneity.

Material	Magnetic Susceptibility ($x10^6$)
Human Tissue	~(-11.0 to -7.0)
Water (at 37°)	-9.05
Magnesia (MgO)	-11.4
Silica (SiO_2)	-16.3
Alumina (Al_2O_3)	-18.1

Table: 4.1: Susceptibilities of selected magnetic materials.

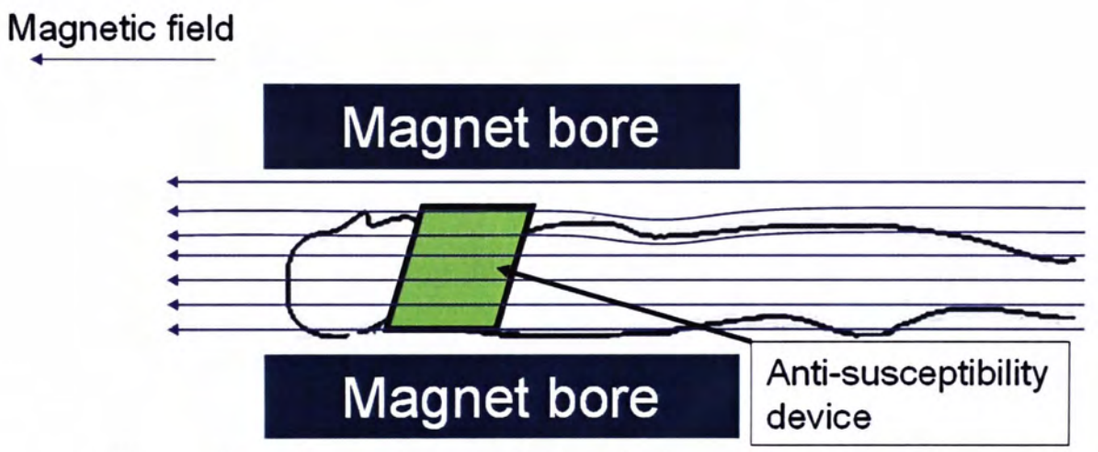

Figure 4.1: Illustration of an anti-susceptibility device used to improve magnetic field homogeneity in the head and neck region.

Figure 4.2: The sat pads filled with liquid perfluorocarbon for the neck region.

Local Shim Method

To reduce magnetic field inhomogeneities induced by the human body, the local field must be shimmed to produce a highly homogeneous magnetic field, a necessary condition for successful spectroscopy to be performed. During the shimming process, local shims are generally adjusted to optimize magnetic field homogeneity within the selected volume of interest (VOI). For each measurement situation, the effect of shimming can be very different on spectrum. Good shimming results in narrower line-width and bad shimming results in poor spectral resolution, and broadened spectral lines.

Shimming can be performed using an iterative method or non-iterative method. Iterative shimming is an optimizing shimming procedure, which by iterative measurements look for the shim settings that provide the maximal amplitude of the time domain signal. Non-iterative shimming is a fast, automatic shimming procedure that explicitly uses the formalism of spherical harmonics to analyze the field inhomogeneity and to determine the shim settings, e.g. fast automatic shimming technique by mapping along projections (FASTMAP) (Gruetter, R., 1993). In the FASTMAP method, the pencil beam (PB) excitation will be used to measure the various orders of static magnetic field variations present in the studied region, and then the measured signal will be processed to estimate the amount of electrical current to be applied to the system shim and gradient coils to balance the local magnetic field variations in the studied region.

Three shimming methods, such as iterative shimming, first-order shimming, and second-order shimming, were available on a 3T whole-body MR imaging system (Achieva 3T X-series; Philips Medical Systems, Best, the Netherlands). Iterative shimming was performed on the VOI, correcting magnetic field inhomogeneity with

the X, Y and Z linear components. The first-order and second-order shimming using pencil beam (PB) were also performed on the shim volume whose size is never smaller than 25 mm in every direction. The PB shimming can optimize magnetic field homogeneity with both first-order (X, Y, Z) and second-order (Z^2, ZX, ZY, XY, X^2-Y^2) shim corrections.

4.3 Phantom studies - CSI Experiments Using Phantoms

4.3.1 Introduction and Objectives

In the MRS data acquisition process, sub-optimal shimming leads to spectral peak broadening and frequency shifts. Studies have shown that spectral linewidth (full width at half maximum, FWHM) is even broaden at 3T compared to 1.5T (Barker, P. B. *et al.*, 2001). It is therefore necessary to develop a method to improve local magnetic field homogeneity to allow CSI in the head and neck.

MRI test phantoms were built to objectively assess the improvement in spectral quality when using an anti-susceptibility device and shimming choices from the scanner. The objectives of this study were to test whether the use of an anti-susceptibility device might improve local shimming so that reliable choline maps could be obtained in the head and neck.

4.3.2 Methods

Phantom Construction

Three phantoms were fabricated, Phantom A (a bottle, 12 cm in diameter and 19 cm in height, Figure 4.3), Phantom B (a head-and-neck (HN) phantom simulating a regular size and shape of the human head, neck and shoulders, attached with an air-

filled cylinder of 4.5 cm in diameter and 6 cm in length to mimic the nasal cavity and mouth and a small air-filled tube of 1.2 cm in diameter and 10 cm in length to mimic the human trachea, Figure 4.4) and Phantom C (a cylindrical bottle of 12 cm in diameter and 19 cm in height with four Cho samples of 1.2 cm in diameter and 4.7 cm in length at a concentration of 10, 5, 2.5 and 1.25 millimolar (mM), Figure 4.5). All phantoms were filled with copper (II) sulfate ($CuSO_4$) doped water for shortening relaxation times. $CuSO_4$ (ReagentPlus^{TM}, minimum 99%, Sigma-Aldrich, St. Louis, MO) was diluted in distilled water at a concentration of approximately 1g/L. Glycerophosphocholine (GPC) (ChromaDex, Irvine CA) was used to prepare solutions of choline.

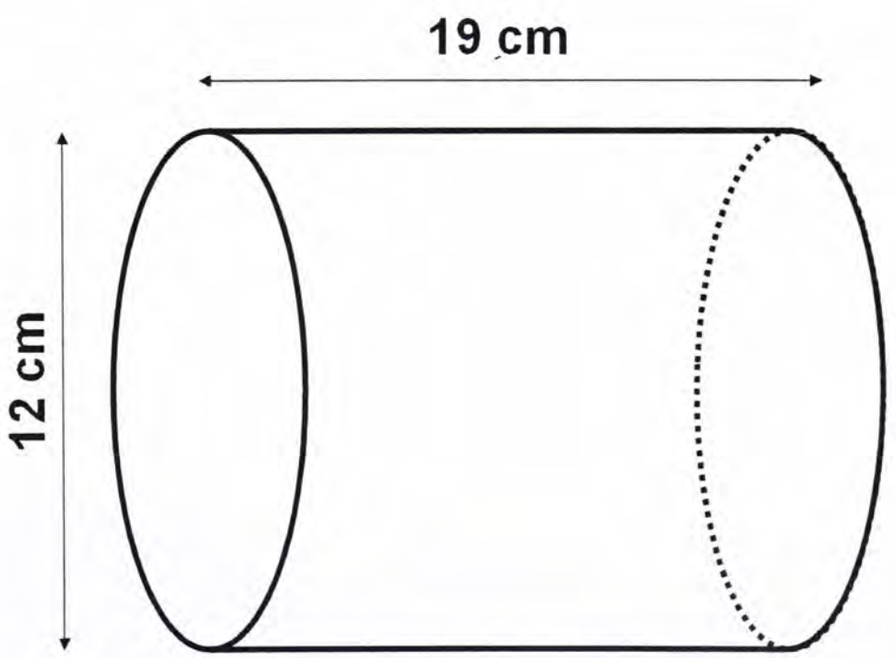

Figure 4.3: Phantom A.

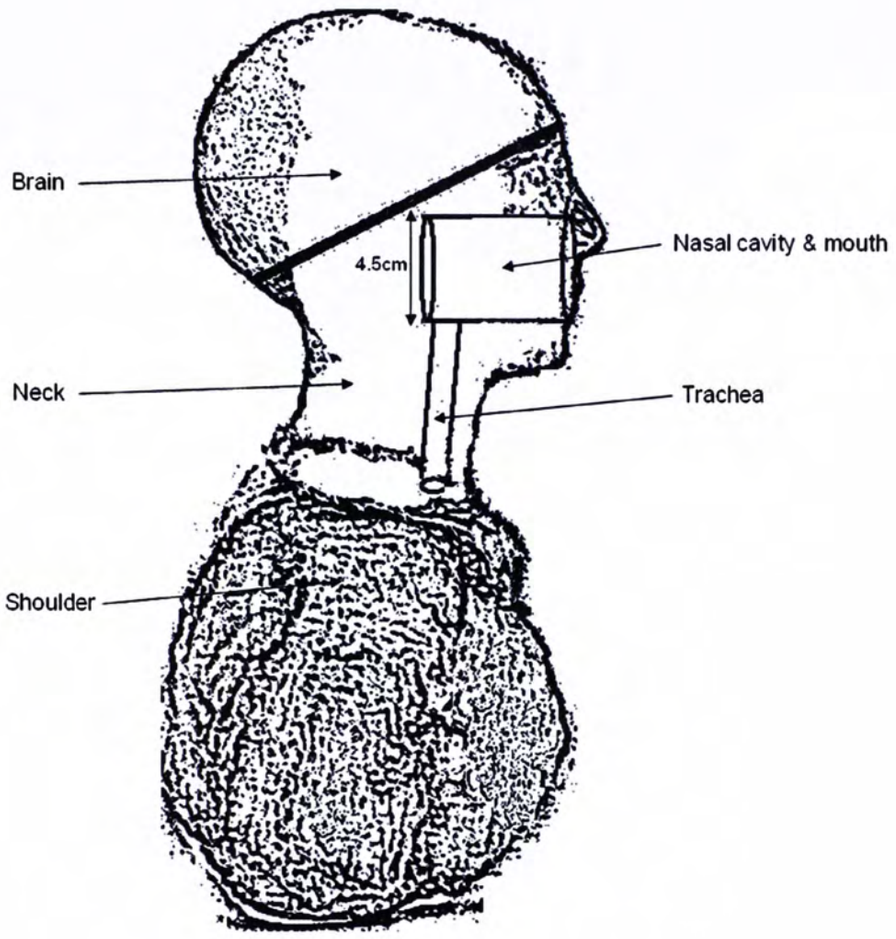

Figure 4.4: Phantom B.

Figure 4.5: Phantom C with choline samples.

4.3.3 Experiment and MR Protocol

Experiment on Phantom A

The aim of this experiment was to use a simple geometry to demonstrate the relative improvement in the line-width of water peak using Phantom A, in the presence and absence of an anti-susceptibility device (Figures 4.6 and 4.7). A VOI placed in the middle of Phantom A was used to evaluate the magnetic field homogeneity over Phantom A (Figure 4.8).

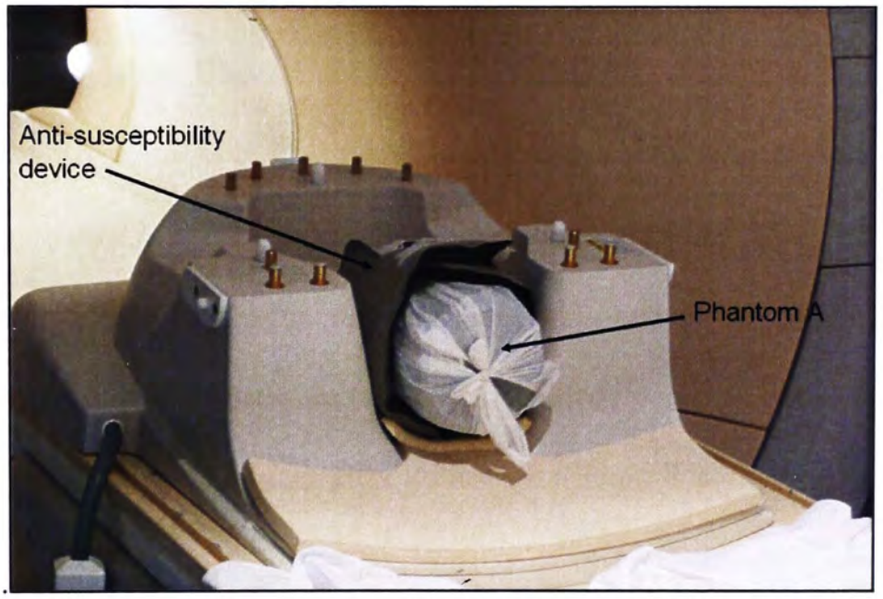

Figure 4.6: Phantom A with an anti-susceptibility device.

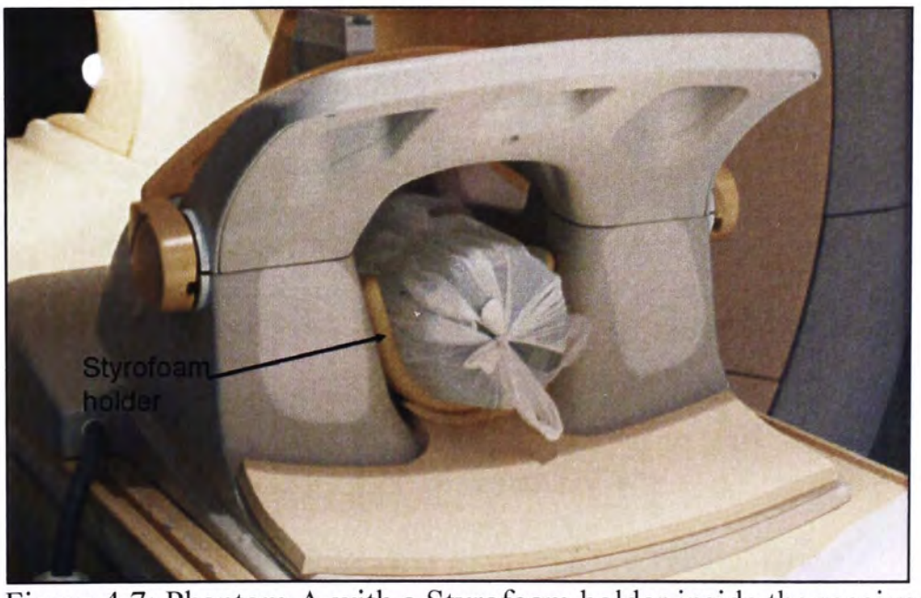

Figure 4.7: Phantom A with a Styrofoam holder inside the receiver coil.

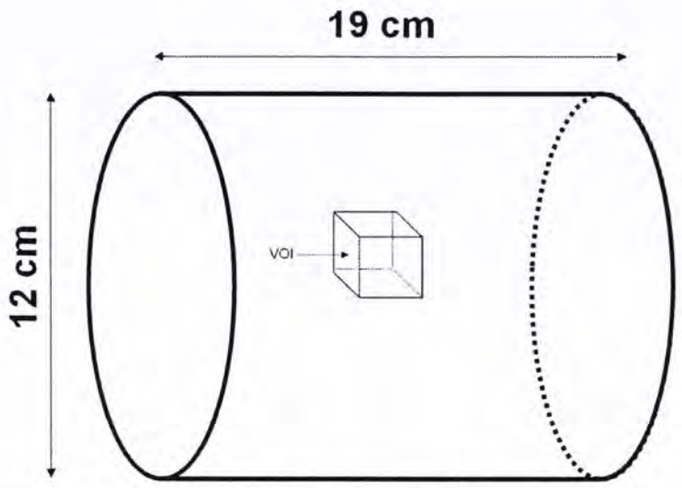

Figure 4.8: A volume of interest within phantom A.

Experiment on Phantom B

Experiments with phantom B used a realistic head and neck structure to mimic the effects of air-tissues interface on magnetic field inhomogeneity. A VOI was placed within Phantom B to measure the magnetic field homogeneity over Phantom B (Figure 4.9) based on measurement of the line-width of the water peak. Experiments were performed with an anti-susceptibility device (Figure 4.10) and without device.

Experiment on Phantom C

The aim of this experiment was to perform CSI on four choline samples at different concentrations using four different shim volume sizes to produce Cho metabolite images from the samples. Phantom C containing 1.25, 2.5, 5 and 10 mM aqueous solution of choline (Cho) samples, was used to demonstrate the feasibility of performing CSI with the use of an anti-susceptibility device. Different sizes of shim volumes were used to demonstrate the effectiveness of the MRI scanner in obtaining a homogeneous magnetic field for a given volume of interest (VOI). In general, a larger VOI will be more difficult to shim compared to a smaller one.

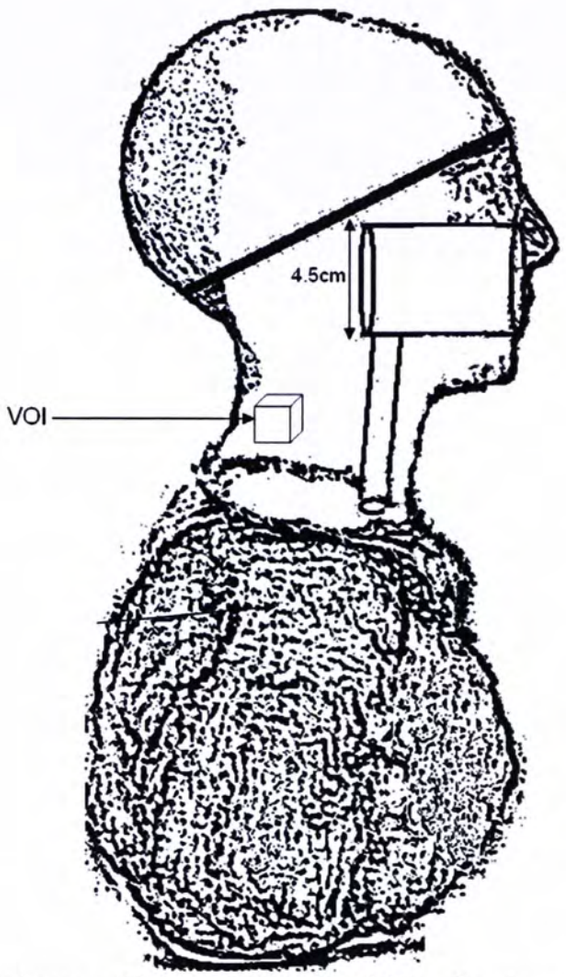

Figure 4.9: A volume of interest (VOI) within phantom B.

Figure 4.10: Phantom B with an anti-susceptibility device.

MRI Equipment and MRI Protocol

All experiments were performed on a 3T whole-body MR imaging system (Achieva 3T X-series; Philips Medical Systems, Best, the Netherlands). The MRI scanner was equipped with an 80 mT/m maximum gradient strength and a standard 16-channel NeuroVascular coil used for signal reception. All scans were done in one session without repositioning of the phantoms.

MRI protocol consisted of a T1-weighted turbo spin-echo (T1W TSE) sequence (repetition time = 360 ms, echo time = 10 ms, section thickness = 4 mm, with no intersection gap; number of signals acquired = two, flip angle = 90°, TSE factor = 4) to guide the positioning of volume of interest (VOI) for MRS.

MRS Protocol for Experiments on Phantom A and B

MRS on Phantoms A and B consisted of a point-resolved spectroscopic (PRESS) sequence with single voxel spectroscopy (SVS) technique (repetition time = 3000 ms, echo time = 288 ms, spectral bandwidth = 2000 Hz, number of signals acquired = 16, data samples = 1024). The VOI was placed in the iso-center of the MR scanner by setting the off-centre parameters to zero. A $2 \times 2 \times 2$ cm^3 shim volume was set to obtain spectra for evaluation. For each shimming method, the same MRS experiment was repeated up to five times (in the presence and/ or absence of an anti-susceptibility device) to obtain sufficient experimental data to allow statistical analysis to be performed.

CSI Protocol for Experiments on Phantom C

CSI on Phantom C consisted of a PRESS-CSI sequence (repetition time = 2000 ms, echo time = 144 ms, the voxel size = $1 \times 1 \times 1$ cm^3, FOV = 24 cm, spectral bandwidth

= 2000 Hz, number of signals acquired = one, data samples = 1024). An automatic water suppression method provided by the scanners was employed.

4.3.4 Data Analysis

Phantom Measurements

Data were reconstructed with the Philips data analysis package (Philips Medical Systems, Best, the Netherlands). All resonant peaks were analyzed using scanner's data processing workstation (ViewForum^{TM} R2.5.3, The Netherlands). The peak fitting procedure generated spectral data describing the peak heights, positions, areas and SNR, as well as producing color-coded metabolite maps and spectra of selected voxels. The water peak was set at 4.67 ppm and the Cho peak at 3.22 ppm (range, 3.16 – 3.28 ppm) in the spectral fitting protocol.

To evaluate the magnetic field homogeneity, spectral line-width was measured at the full width at half maximum (FWHM) in term of parts per million (ppm). The Larmor equation was used to convert the FWHM from Hz to ppm of the magnetic field strength, $FWHM(ppm) = FWHM(Hz)/42.576B_o(T)$. The FWHM (ppm) defines the magnetic field inhomogeneity over the phantom volume (Joseph G. Och *et al.*, 1992).

Statistical Analysis

The percentage reduction in field inhomogeneity (δB_o) was calculated by subtracting the mean water peak line-width after using the device from the mean water peak line-width before using device and then dividing by the mean water peak line-width before using the device

A Wilcoxon signed rank test was employed to detect any statistically significant difference of the water line-width between before and after the use of an anti-susceptibility device in the phantoms. A Friedman test was employed to detect any statistically significant difference of the water peak line-width among the three groups, first-order shimming, second-order shimming, and iterative shimming. If statistically significant difference ($p < 0.05$) was obtained, a two-tailed non-parametric Mann-Whitney U test was used to assess difference between each pair of these groups, and a p-value of less than 0.05 was considered to be statistically significantly different. Data were expressed as means ± standard deviation (SD). All statistical analyses were performed using SPSS, version 11.0 (SPSS, Chicago. III).

4.3.5 Phantom Experimental Results

Results from Experiments on Phantom A

Results of the experiments using Phantom A (cylindrical phantom) are shown in Table 4.2. The mean line-width of water peak without an anti-susceptibility device was 3.94 ± 1.9 Hz. The mean line-width of the water peak with an anti-susceptibility device was 2.22 ± 0.32 Hz. Spectral line-width was significantly lower with an anti-susceptibility device ($p < 0.001$, Wilcoxon signed rank test). The average reduction of the magnetic field inhomogeneity (δBo) was calculated about 43.7%.

Three shimming methods were tested using Phantom A without using an anti-susceptibility device. The mean line-widths and ranges of the water peaks were calculated and shown in the Table 4.3. When comparing first-order shimming, second-order shimming, and iterative shimming, statistical analysis showed that there was a statistically significant difference ($p = 0.007$, Friedman test) in terms of water peak line-widths among these three groups. When comparing each pair, the spectral

line-widths of second-order shimming were significantly lower than that of first-order shimming ($p < 0.001$) and iterative shimming ($p = 0.001$). The spectral line-widths of iterative shimming were significantly lower ($p = 0.002$) than that of first-order shimming (Figure 4.11, Table 4.4).

These shimming methods were again tested using an anti-susceptibility device wrapped around Phantom A. The mean line-widths and ranges of the water peaks are shown in Table 4.5. By comparing the three groups of first-order shimming, second-order shimming, and iterative shimming, a statistically significant difference ($p < 0.001$, Friedman test) was found among them. When comparing each pair, the spectral line-widths of second-order shimming were significantly lower than that of first-order shimming ($p < 0.001$) and iterative shimming ($p < 0.001$), and the spectral line-widths of iterative shim were significantly lower ($p = 0.001$) than that of first-order shim (Figure 4.12, Table 4.6). The second-order shimming method produced the narrowest water peak line-widths compared with other shimming methods whether an anti-susceptibility device was used or not.

	Water peak line-width (Hz)	
Phantom A/ Statistical values	Without Device	With Device
Mean	3.94	2.22
standard deviation (SD)	1.9	0.32
Range	1.53 - 6.13	1.66 - 2.81
Number of scan	27	40
Reduction of the field inhomogeneity (δBo)	43.7%	
p-value	<0.001	

Table 4.2: Comparison of Phantom A with and without device.

Phantom A Without Device/ Method	Mean water peak line-width ± SD (Hz)	Range (Hz)
First-order shimming (n = 10)	5.98 ±0.08	5.88-6.13
Second-order shimming (n = 12)	1.94 ±0.21	1.53-2.17
Iterative shimming (n = 5)	4.67 ±0.35	4.22-5.11

Table 4.3: Phantom A without device, mean weak peak line-width ± standard deviation (SD) and range.

Mann-Whitney U test for Phantom A without device

Comparison			p-value
First-order shim	versus	Second-order shim	<0.01
Second-order shim	versus	Iterative shim	0.001
First-order shim	versus	Iterative shim	0.002

Table 4.4: Comparison of shimming techniques for Phantom A without device.

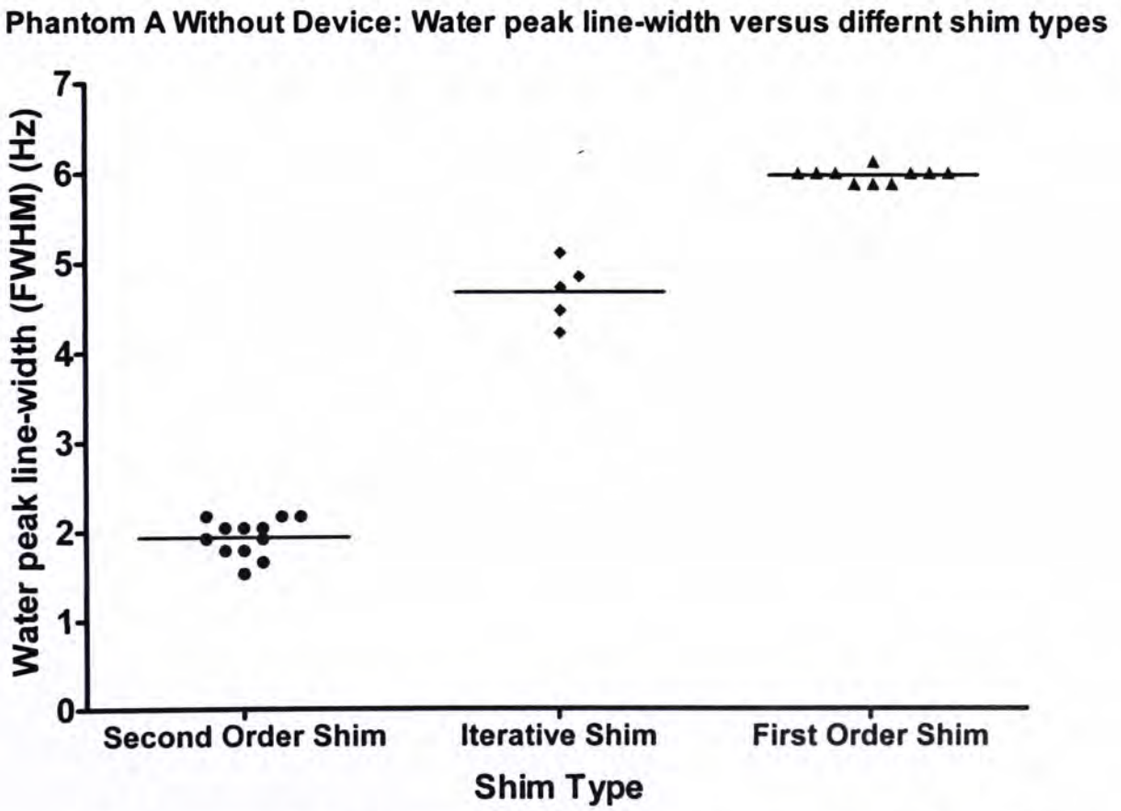

Figure 4.11: A scatter plot of Phantom A without device: Water peak line-width versus different shim types.

Phantom A With Device/ Method	Mean water peak line-width ± SD (Hz)	Range (Hz)
First-order shimming (n = 16)	2.54 ±0.15	2.30-2.81
Second-order shimming (n = 16)	1.90 ±0.12	1.66-2.04
Iterative shimming (n = 8)	2.24 ±0.15	2.04-2.55

Table 4.5: Phantom A with mean weak peak line-width ± standard deviation (SD), range, number of scan (n), reduction of the field inhomogeneity (δBo) and p-values.

Mann-Whitney U test for Phantom A with device

Comparison of shimming techniques			p-value
First-order shim	versus	Second-order shim	<0.001
Second-order shim	versus	Iterative shim	<0.001
First-order shim	versus	Iterative shim	0.001

Table 4.6: Comparison of shimming techniques for Phantom A with device.

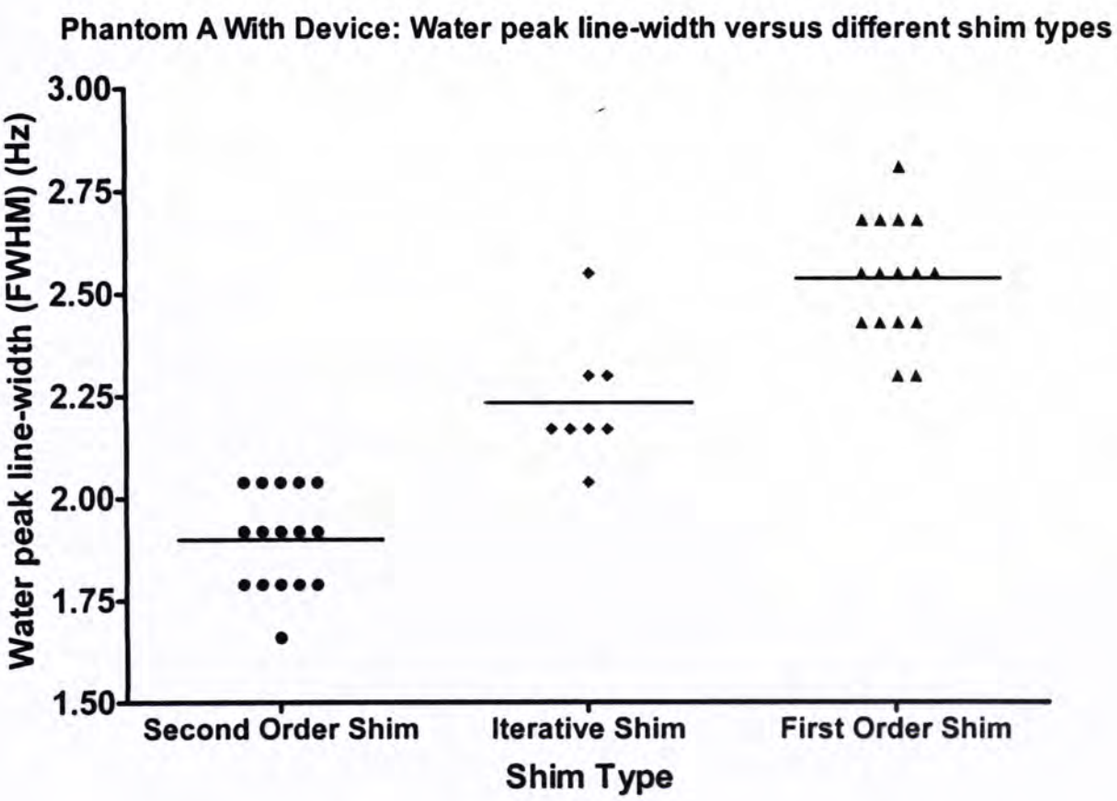

Figure 4.12: A scatter plot of Phantom A with device: Water peak line-width versus different shim types.

Results from Experiments on Phantom B

Phantom B, designed to mimic the large susceptibility differences in the head and neck, was tested with and without an anti-susceptibility device while undergoing MRS experiments (Table 4.7) and the mean line-width of water peak when an anti-susceptibility device was used was 4.9 Hz. Spectral line-width of water peak was significantly lower with an anti-susceptibility device ($p < 0.001$, Wilcoxon Signed Rank test). After the use of an anti-susceptibility device in Phantom B, the average reduction of the magnetic field inhomogeneity (δBo) was about 57%.

Without using an anti-susceptibility device, the three shimming methods were tested using Phantom B. The mean line-widths and ranges of the water peaks obtained are shown in Table 4.8. When comparing the three shimming methods (first-order shimming, second-order shimming and iterative shimming), statistical analysis demonstrated that there was a statistically significant difference ($p = 0.007$, Friedman test) among them. When comparing each pair, the mean water peak line-widths of second-order shimming were significantly lower than that of first-order shimming ($p < 0.001$) and iterative shimming ($p = 0.002$), and the mean line-widths of first-order shimming were significantly lower ($p = 0.003$) than that of iterative shimming (Figure 4.13, Table 4.9).

These three shimming methods were again tested using Phantom B together with an anti-susceptibility device. The mean line-widths and ranges of the water peaks are shown in Table 4.10. When comparing first-order shimming, second-order shimming, and iterative shimming, a statistically significant difference ($p = 0.001$, Friedman test) was found among them. When comparing each pair, the mean water peak line-widths of second-order shimming were significantly lower than that of first-order shimming ($p < 0.001$) and iterative shimming ($p < 0.001$). The spectral

line-widths of iterative shimming were significantly lower (p= 0.011) than that of first-order shimming (Figure 4.14, Table 4.11). The second-order shimming produced the narrowest line-widths compared to other shimming methods.

	Water peak line-width (Hz)	
Phantom B/ Statistical values	Without Device	With Device
Mean	11.4	4.90
Standard deviation (SD)	6.34	2.29
Range	4.22 – 18.27	1.79 – 7.15
Number of scan (n)	24	35
Reduction of the field inhomogeneity (δBo)	57.0%	
p-value	<0.001	

Table 4.7: Comparison of Phantom B with and without device.

Phantom B Without Device/Method	Mean water peak line-width ± SD (Hz)	Range (Hz)
First-order shimming (n = 8)	16.5 ±0.36	15.97-16.99
Second-order shimming (n = 11)	4.67 ±0.38	4.22-5.36
Iterative shimming (n = 5)	18.0 ±0.25	17.63-18.27

Table 4.8: Phantom B without device, mean weak peak line-width ± standard deviation (SD) and range.

Mann-Whitney U test for Phantom B without device

Comparison			p-value
First-order shim	versus	Second-order shim	<0.001
Second-order shim	versus	Iterative shim	0.002
First-order shim	versus	Iterative shim	0.003

Table 4.9: Comparison of shimming techniques for Phantom B without device.

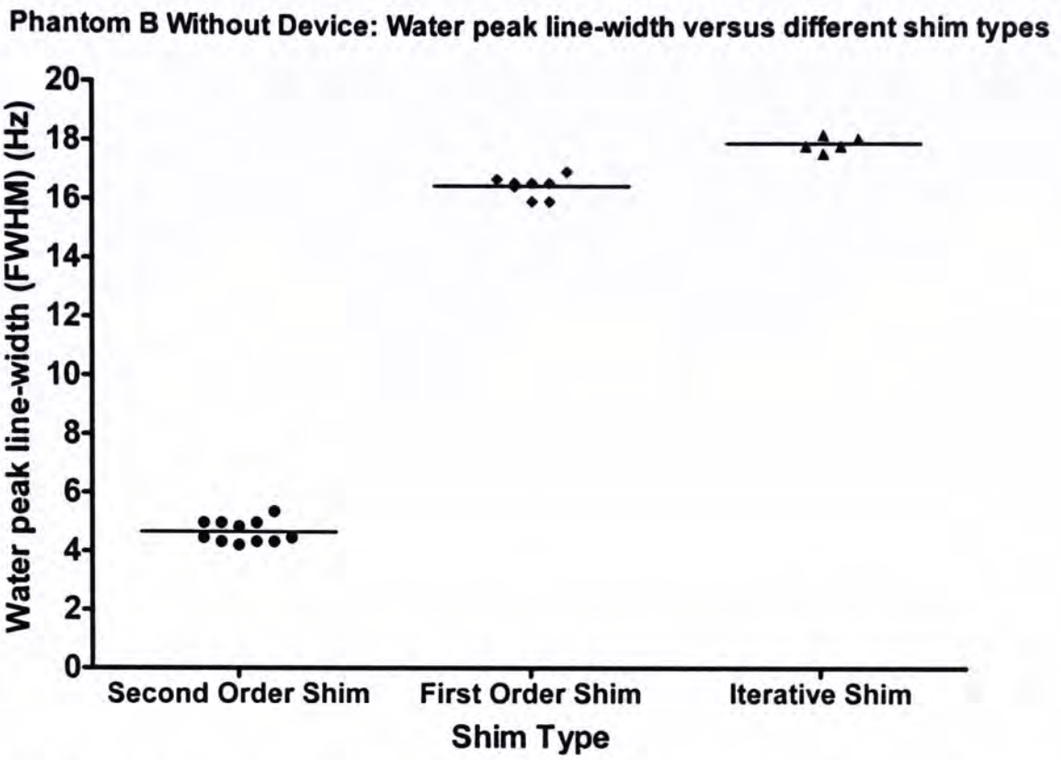

Figure 4.13: A scatter plot of Phantom B without device: Water peak line-width versus different shim types.

Phantom B With Device/Shim Type	Mean water peak line width ± SD (Hz)	Range (Hz)
First-order shimming (n = 14)	6.83 ±0.23	6.51-7.15
Second-order shimming (n = 14)	2.15 ±0.19	1.79-2.43
Iterative shimming (n = 7)	6.53 ±0.17	6.26-6.77

Table 4.10: Phantom B with device, mean weak peak line-width ± standard deviation (SD) and range.

Mann-Whitney U test for Phantom B with device

Comparison of shimming techniques			p-value
First-order shim	versus	Second-order shim	<0.001
Second-order shim	versus	Iterative shim	<0.001
First-order shim	versus	Iterative shim	0.011

Table 4.11: Comparison of shimming techniques for Phantom B with device.

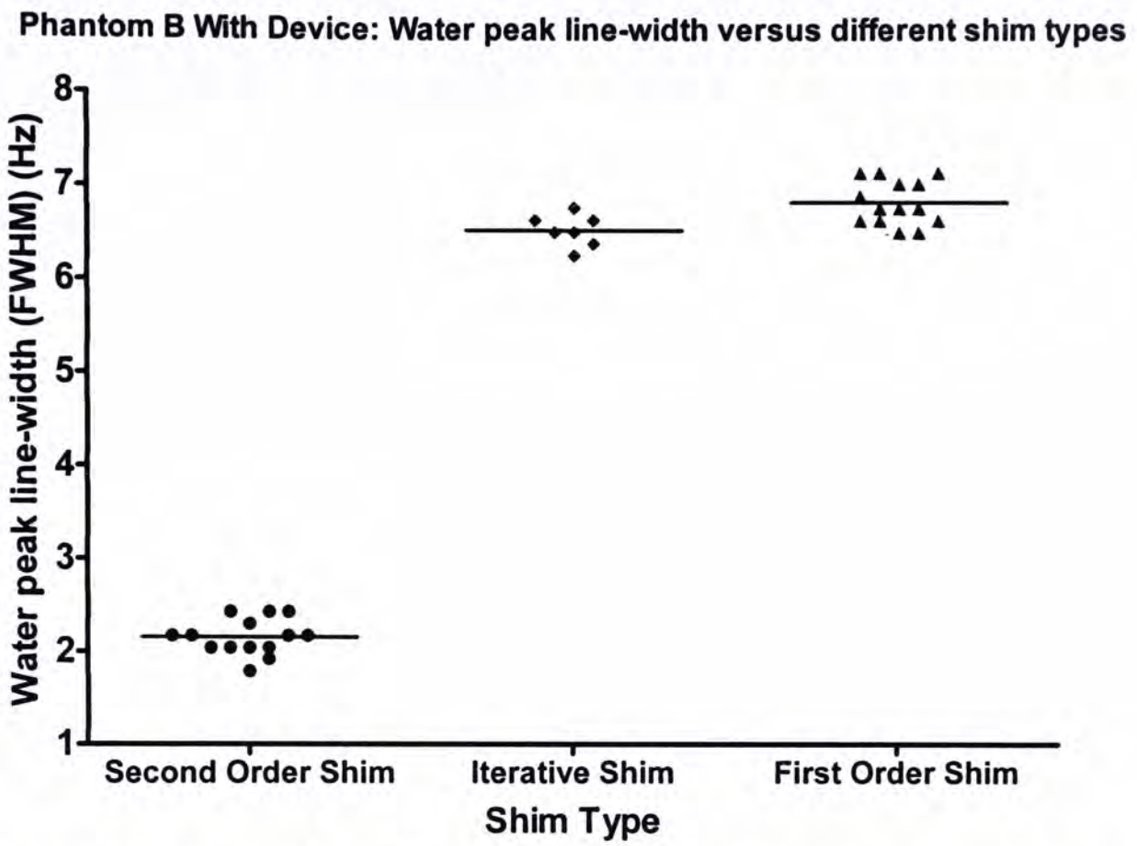

Figure 4.14: A scatter plot of Phantom B with device: Water peak line-width versus different shim types.

Results from Experiments on Phantom C

CSI experiments were using Phantom C which contained 1.25, 2.5, 5 and 10 mM Cho samples. Results obtained for PB auto second order shimming demonstrated the feasibility of performing CSI with different shim volumes, such as $8\times8\times1$ cm^3 (Figure 4.15), $7\times7\times1$ cm^3 (Figure 4.16), $6\times6\times1$ cm^3 (Figure 4.17), and $5.5\times5.5\times1$ cm^3 (Figure 4.18).

The colour-coded images showed that hot spots in yellow represented a relatively high Cho signal compared to the cold spot in orange.

Cho maps were correctly produced where Cho samples were placed. The spectral line-widths measured from the 10 mM Cho sample spectra obtained from different shim volumes showed that as shim volume was reduced, there was a corresponding

reduction in the peak line-width (Table 4.12) without marked changes in the peak SNR.

Shim volume size	Line-width of a 10 mM choline solution	Signal-to-noise ratio (SNR)
8x8x1 cm^3	10.60 Hz	108
7x7x1 cm^3	10.22 Hz	127.7
6x6x1 cm^3	9.84 Hz	125.2
5.5x5.5x1 cm^3	9.45 Hz	106

Table 4.12: Shim volume sizes with line-widths of choline peak.

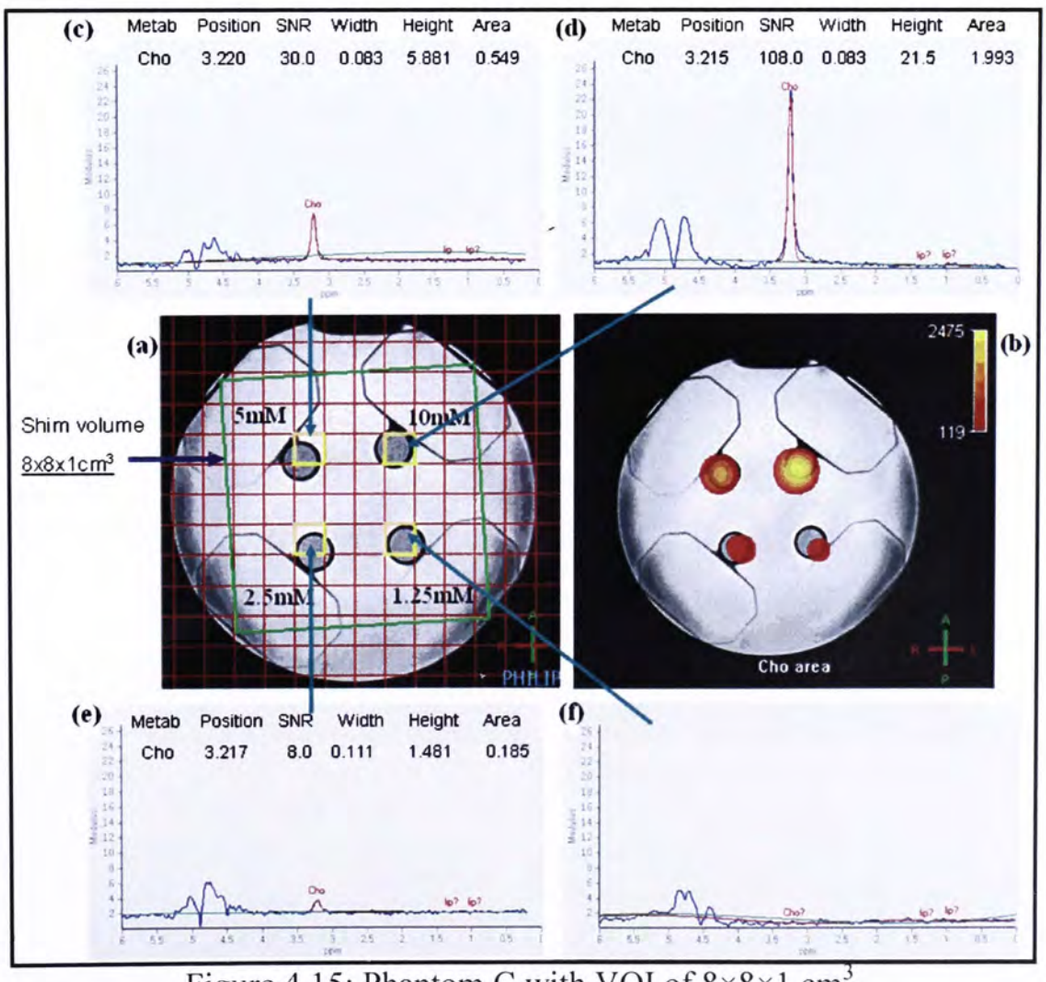

Figure 4.15: Phantom C with VOI of 8×8×1 cm^3.

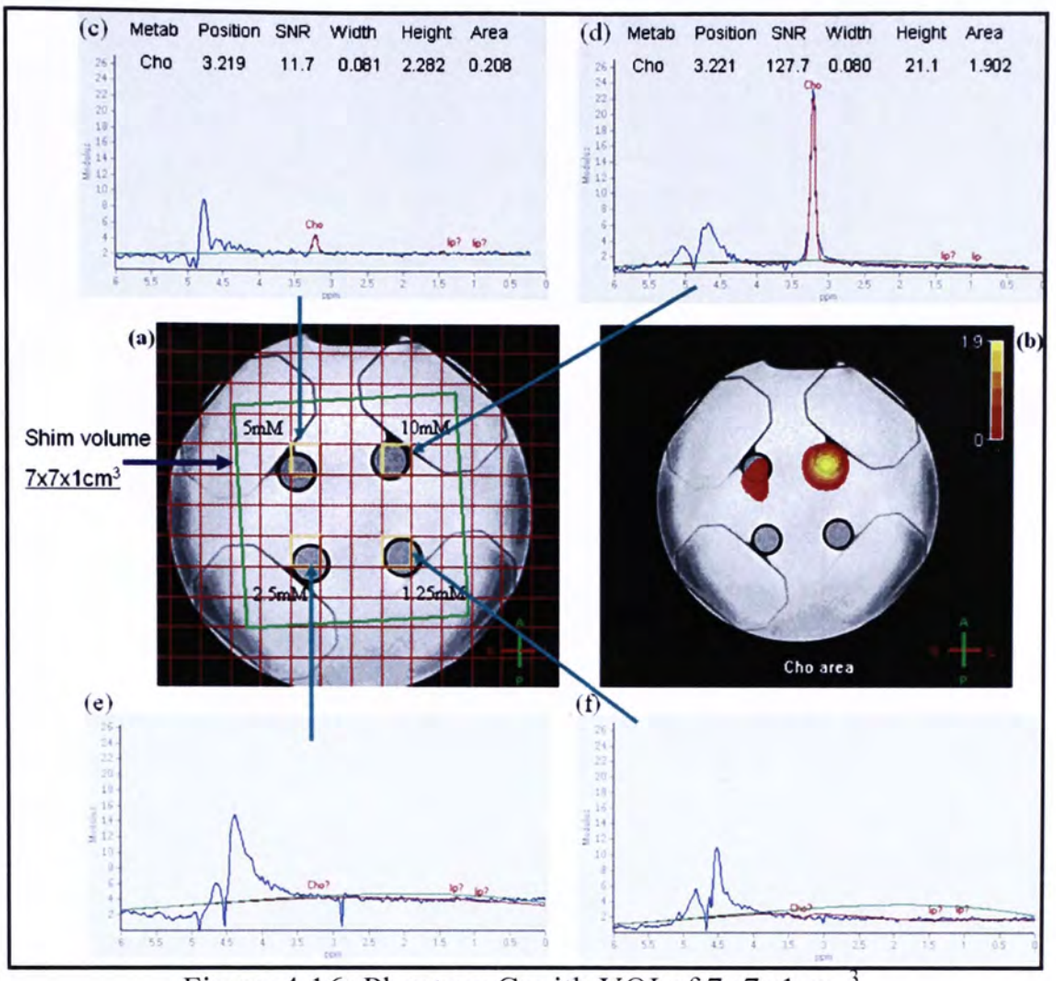

Figure 4.16: Phantom C with VOI of 7×7×1 cm^3.

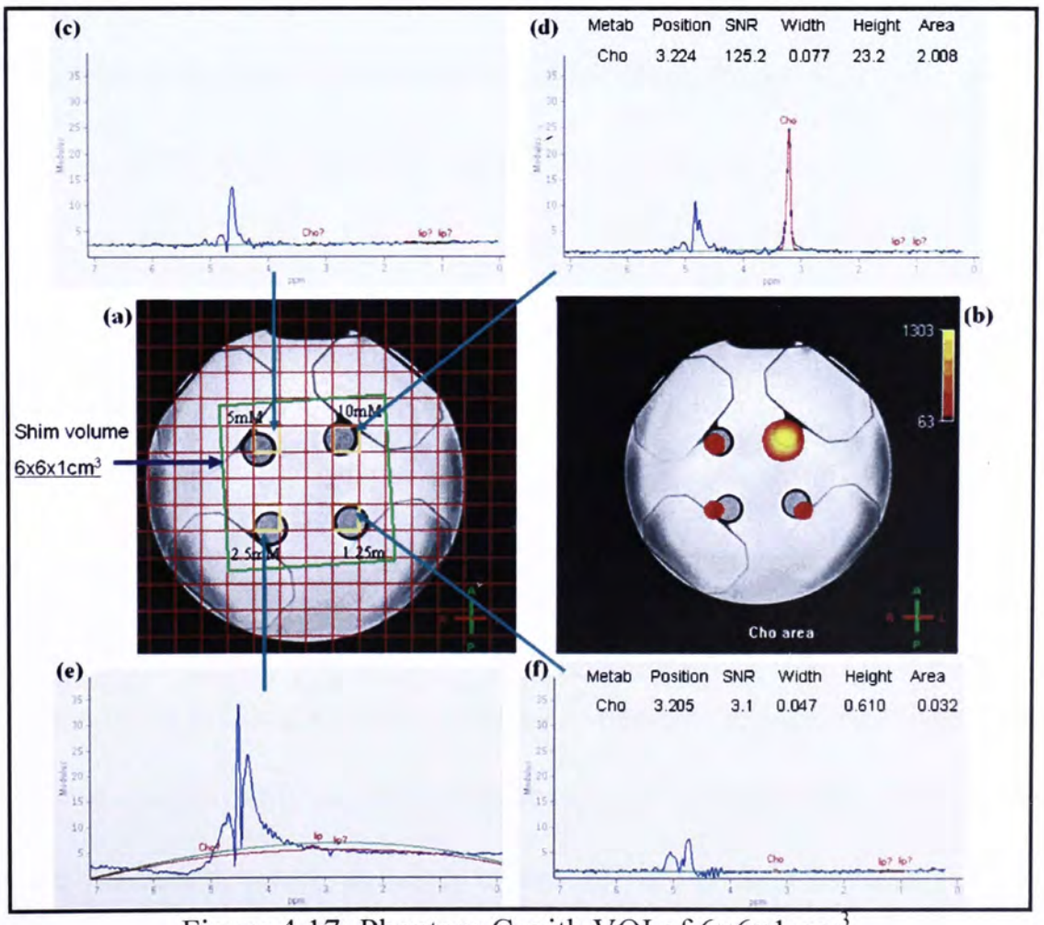

Figure 4.17: Phantom C with VOI of 6×6×1 cm^3.

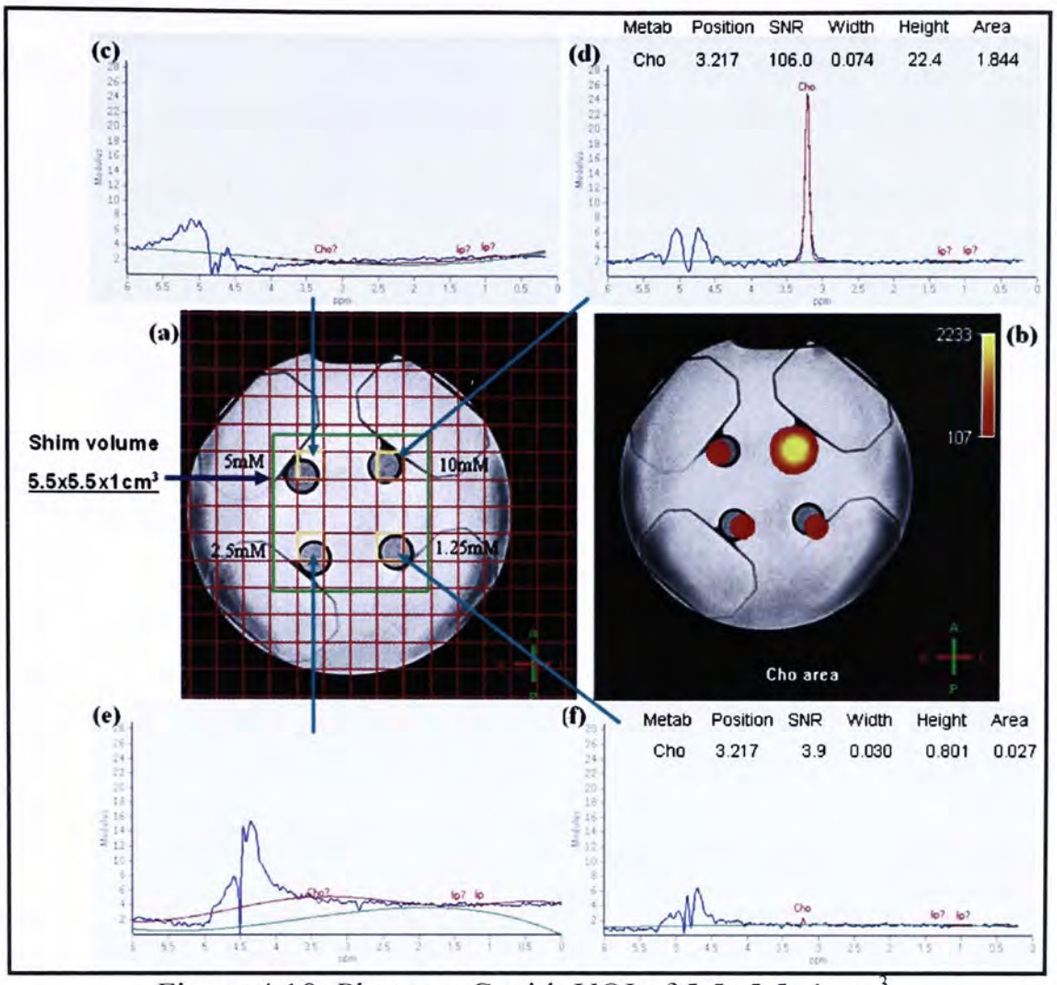

Figure 4.18: Phantom C with VOI of 5.5×5.5×1 cm^3.

4.3.6 Discussion and Conclusion on Phantom Experiments

Spectral line-widths obtained before and after the use of an anti-susceptible device filled with liquid perfluorocarbon (PFC) in the phantom studies showed that the device could significantly reduce magnetic field inhomogeneities and improve spectral resolution. Liquid PFC is a non-protonated substance that does not generate any proton signal in proton MRI and has a magnetic susceptibility similar to human tissues. Hence, the device has been used to improve fat saturation of the neck and quality of MR images.

By comparing the line-width of the water peaks obtained from experiments without using an anti-susceptibility device, a relatively large standard deviation was noted. This large standard deviation indicated a large variability and uncertainty in

obtaining consistent results from all three shimming methods tested. When employing the anti-susceptibility device, the spectral line-widths became much narrower with a smaller standard deviation. The device groups appeared to yield more consistent results from the three shimming methods tested. This effect can be explained by the fact that the anti-susceptibility device filled with the outer air spaces of the phantoms such that susceptibility effects were reduced. Hence, the use of an anti-susceptibility device could improve the local magnetic field homogeneity and enables reliable CSI to be performed, demonstrated by narrow peak line-widths. Effectiveness of the iterative, first-order and second-order shimming methods were tested using phantoms, and the spectral line-widths of water peak obtained were compared. In experiment using a cylindrical bottle, these three shimming methods could produce relatively narrow line-widths in a given VOI. This was probably because the geometry of the cylindrical bottle, being in a cylindrical shape and with no air gap, the susceptibility effects of the phantom on the local magnetic field homogeneity were minimal. Hence, these three shimming methods could produce narrow line-widths.

However, the spectral line-widths obtained from a human-sized head and neck phantom designed and constructed for this research indicated significant differences among different shimming methods. The spectral line-widths of iterative and first-order shimming were greater than that of the second-order shimming. This meant that iterative and first-order shimming could not reduce field inhomogeneity as effective as second-order shimming, and thereby leading to a much broader line-width. This line-width broadening occurred because of inadequate shimming, leading to inhomogeneities in the local magnetic field during data acquisition. Magnetic field inhomogeneity was more severe in the head and neck phantom than a

cylindrical bottle due to the geometry of the phantom, and presence of air within the phantom. Hence, first-order and iterative shimming seemed to be an insufficient method to correct local field inhomogeneities in the head and neck phantom. Second-order shimming, on the other hand, could effectively reduce field inhomogeneity created by the head and neck phantom, producing a much narrower peak line-width.

To minimize motion artifacts during CSI data acquisition, a short scan time is essential. The total execution time for PB-shimming (first-order and second-order shimming) and iterative shimming are approximately 30-40 seconds and 4-5 minutes, respectively, with the exclusion of the time required for water and/or fat suppression. PB-shimming could provide a shorter total scan time than iterative shimming, and therefore, PB-shimming may be used to minimize motion artifacts in CSI.

This study also showed that shimming a larger VOI is more challenging than shimming a smaller one. A large VOI could create difficulties in shimming, leading to broadened line-widths in CSI or study failure. In the phantom studies, CSI was performed with different shim volumes on a bottle phantom containing choline samples. Data from this study showed that the spectral line-width of a 10 mM choline solution became smaller with decreasing shim volume. These results suggest that shimming a smaller volume could result in a more homogeneous local magnetic field and better spectral resolution.

Results from CSI experiments also showed that Cho at low concentration such as 1.25 and 2.5 mM may not be readily detectable. Undetectable Cho could also be due to partial volume contamination or the effect of voxel bleeding, which is referred to signal contamination from adjacent spectroscopic voxels. Metabolite spectra within such a voxel would exhibit contamination by signals from surrounding voxels. To

minimize partial volume effects, carefully positioning smaller voxels within ROI might be helpful.

Experimental data from this work strongly supports the notion that an anti-susceptibility device filled with liquid PFC could significantly improve the local magnetic field homogeneity. Results from this work indicated the best local magnetic field homogeneity in the phantoms could be achieved when using an anti-susceptibility device together with PB-auto second-order shimming. Local shimming could be further improved by shimming a relatively smaller volume of interest, which implies that selecting a shim volume matching the dimensions of the lesion of interest could significantly increase the likehood of a successful CSI study.

4.4 In vivo CSI Study of Human Head and Neck Tumors

4.4.1 Introduction and Objectives

Proton chemical shift imaging (^{1}H-CSI) has been successfully used to detect elevated choline containing-compounds (Cho) in different cancers, but because of inherent problems of performing CSI in the head and neck region, this technique has not been applied in the study of head and neck tumors. In this project, phantom based experiments have identified the conditions under which CSI may be performed in the head and neck where large susceptibility differences have a negative effect on local magnetic field homogeneity. The objectives of this part of the CSI study were to apply the methods learned from phantoms studies on patients with head and neck tumors in vivo.

4.4.2 Patient Selection

Consecutive patients with newly diagnosed head and neck tumors were recruited for this prospective study. The research ethics committee approval was obtained and an informed consent was also obtained from all patients before the study. Thirteen patients with head and neck tumors underwent both MRI and CSI examinations between November 2008 and March 2009. Histological and imaging findings were the reference standard for the head and neck tumors.

4.4.3 MRI and CSI Protocol

All examinations were performed on a 3T whole-body MR imaging system (Achieva 3T X-series; Philips Medical Systems, Best, the Netherlands). The MRI scanner was equipped with an 80 mT/m maximum gradient strength for MRI. A 16-channel NeuroVascular coil was used to obtain high-quality images to include tumors arising from the upper aerodigestive tract. An anti-susceptibilities device filled with liquid perfluorocarbon (PFC) (Sat Pad, Magmedix, Inc.) was used to improve the local magnetic field homogeneity in the head and neck tumor patients.

MRI images were used to help defining the volumes of interest (VOI) to include the region of interest (ROI) for CSI. MRI sequences included an axial T1-wieghted turbo spin-echo (T1W TSE) sequence (repetition time = 540 ms, echo time = 10 ms, section thickness = 4mm, with no intersection gap, acquisition matrix = 512 ×352, number of signals acquired = 2), an axial T2-wieghted fat-suppressed (T2W FS) sequence (repetition time = 4455 ms, echo time = 80 ms, section thickness = 4 mm, with no intersection gap acquisition matrix = 364 × 262, number of signals acquired = 2).

CSI was performed on a single slice using a two-dimension point-resolved spectroscopic sequence (2-D PRESS) for volume selection (repetition time = 2000 ms, echo time = 144 ms, voxel size = $1\times1\times1$ cm^3, FOV = 24 cm, number of signals acquired =1, spectral bandwidth = 2000 Hz, data samples = 1024). PB-auto second order shimming was used to optimize the local magnetic field homogeneity for CSI.

4.4.4 Data Analysis

CSI data were analyzed using the Philips data analysis package (Philips Medical Systems, Best, the Netherlands). The water peak was referenced at 4.67 ppm, Cho peak at 3.22 ppm (range, 3.15 – 3.27 ppm) and the fatty acids peaks (0.9 – 1.3 ppm) from methylene group at 0.9 ppm and methyl group at 1.3 ppm.

Head and neck tumor measurements, such as minimum axial diameter, maximum axial diameter and area of lesion, were also recorded. Statistical data were expressed as the mean plus or minus the standard deviation (SD).

4.4.5 Results from CSI on Patients

CSI was performed on 13 head and neck tumors which showed an average maximum axial diameter of 3.73 ± 1.67 cm (range, 1.86 – 8.57 cm), average minimum axial diameter of 2.36 ± 0.89 cm (range, 1.32 – 4.65 cm), and average area of 7.51 ± 6.19 cm^2 (range, 1.27 – 25.91 cm^2). CSI was unsuccessful in four cases due to patient movement and susceptibility artifacts (primary NPC, n = 2; tonsil SCC, n = 1; hard palate mucoepidermoid carcinoma (MECa), n = 1). CSI was successful in producing choline maps showing the distribution of choline-containing compounds (Cho) in nine patients, hence, the success rate of performing CSI was calculated to be 69% (9/13) in this pilot CSI study. The nine patients comprised of eight men and one

woman aged between 26 and 55 years of age (mean age ± standard derivation = 48 ± 9) with 9 head and neck tumors (undifferentiated nasopharyngeal carcinoma (NPC) lymph node metastasis, n = 5; squamous cell carcinoma (SCC) lymph node metastasis, n = 2; benign Schwannoma, n = 2). Table 4.13 summarizes the patent demographics, lesion characteristics, and CSI results. The average of Cho SNR was 5.26 ± 2.60 (range, 2.3 – 9.48), and the average line-width of Cho was 15.4 ± 5.68 Hz (range, 7.41 – 25.5 Hz). Lipids (at 0.9 and 1.3 ppm) were also present in the spectra.

Figure 4.19-22 show four examples of successful CSI, the corresponding MR images and selected spectra from the head and neck tumors of four patents. Elevated Cho were apparent within the CSI images; their SNR were sufficient for data analysis and interpretation. The shim volume was used to optimize the magnetic field homogeneity over the studied region, shown by the green rectangle.

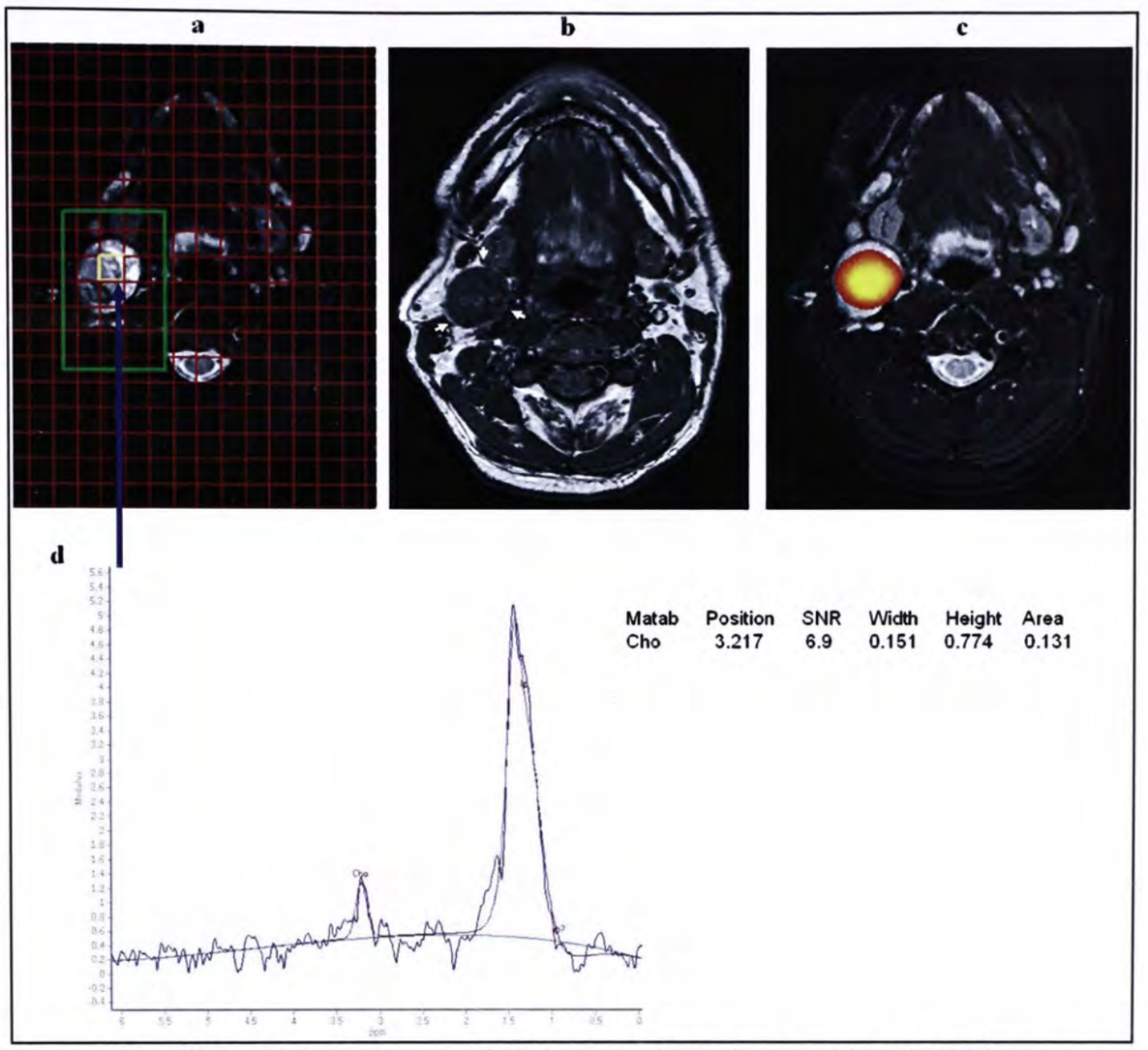

Figure 4.19: MRI and CSI images of a 41-year-old patient (subject 1) with a metastatic node of SCC. The elevated choline "hot-spot" (range of SNR Cho, 2.6 – 6.9) was correctly produced where the lesion was located as shown by conventional MR images. The spectrum as shown was selected from the yellow voxel found within the green rectangle (shim volume) and choline signal from that voxel had a SNR of 6.9.

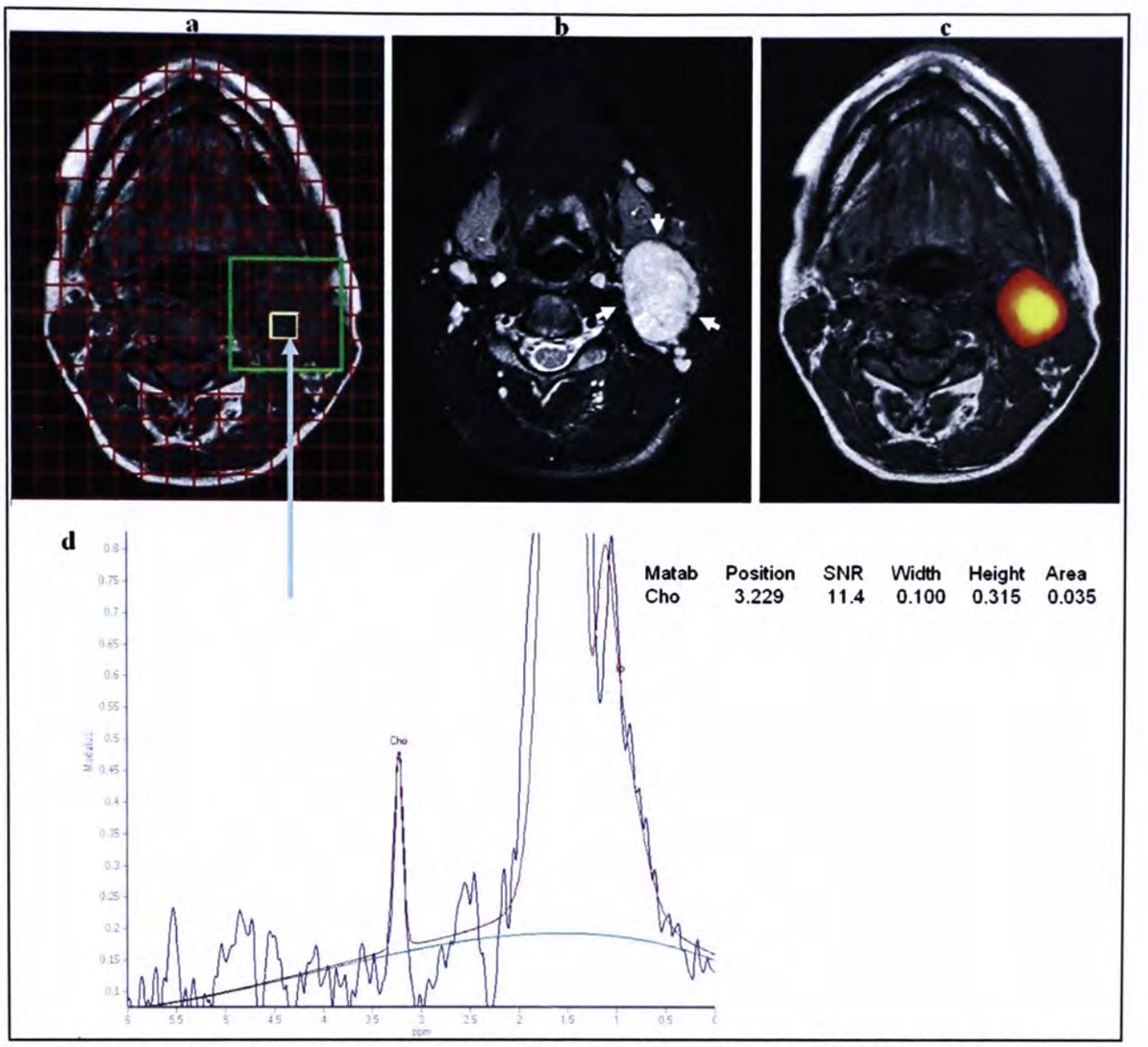

Figure 4.20: MRI and CSI images of a 50-year-old patient (subject 2) with a metastatic node of NPC. The elevated choline "hot-spot" (range of SNR Cho, 2.5 – 19.5) was correctly produced where the lesion was located as shown by conventional MR images. The spectrum as shown was selected from the yellow voxel found within the shim volume and choline signal from that voxel had a SNR of 11.4.

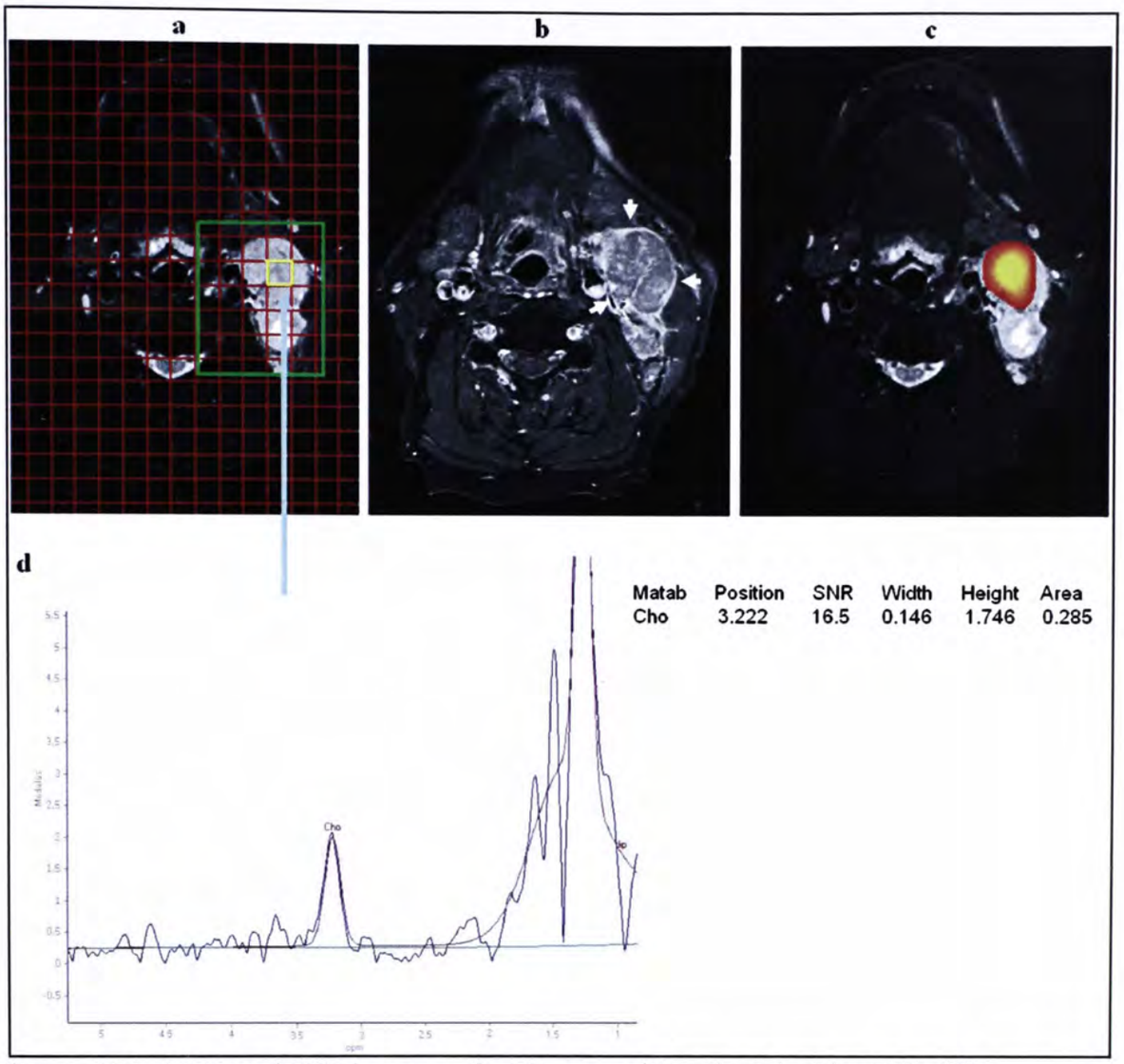

Figure 4.21: MRI and CSI images of a 52-year-old patient (subject 4) with a metastatic node of NPC. The superior part of the tumor had elevated Cho signals (range of SNR Cho, 4.8 – 16.5) compared with the inferior parts of the lesion. The spectrum as shown was selected from the yellow voxel found within the shim volume. The choline signal from that voxel had a fairly narrow line-width (suggesting good shimming was achieved) and a high SNR (16.5).

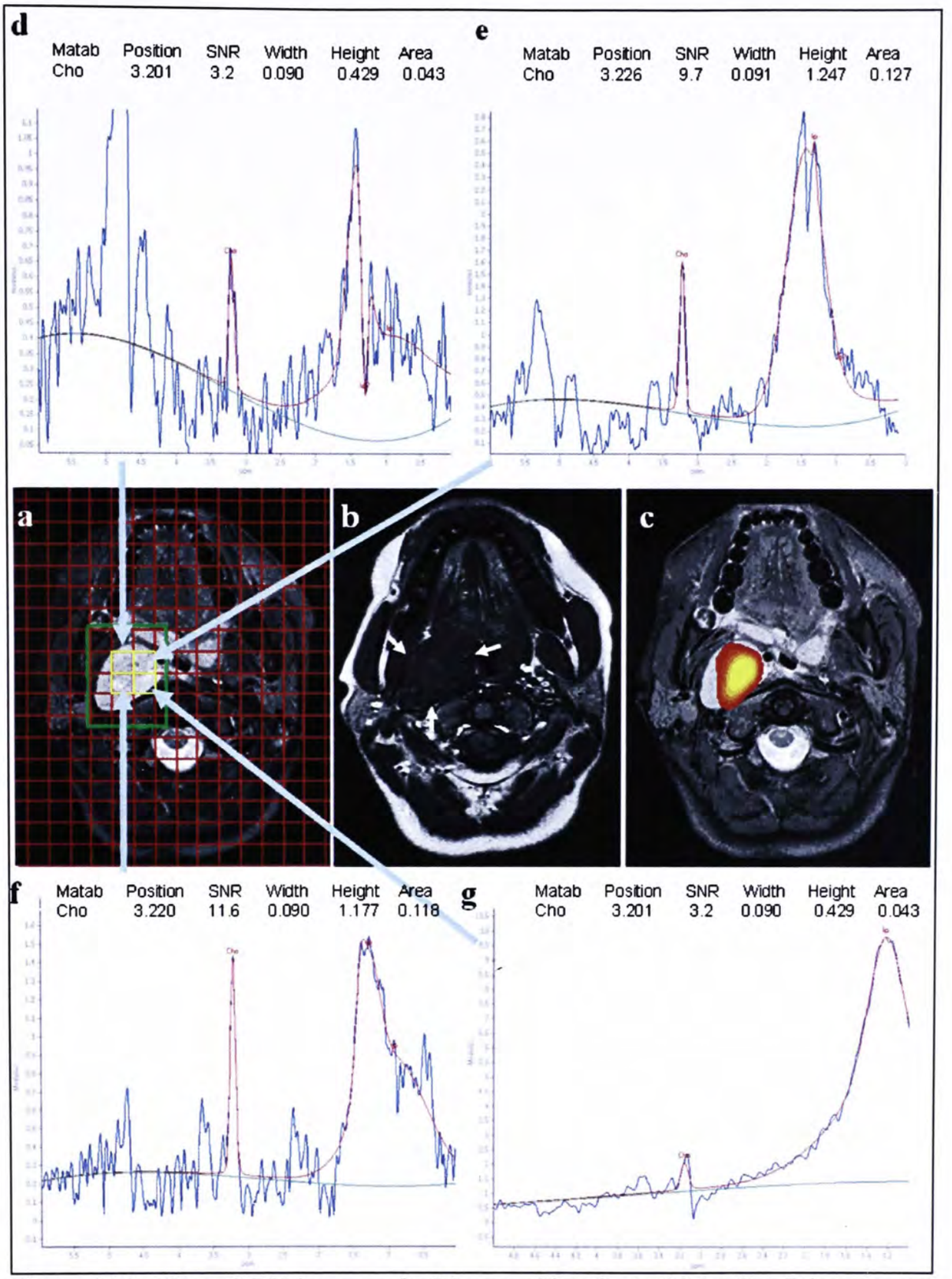

Figure 4.22: MR and CSI images of a 26-year-old patient with benign Schwannoma (Subject 6). The elevated choline "hot-spot" was apparent in this benign tumor as shown by conventional MR images. The spectra as shown were selected from the yellow voxels found within the shim volume and choline signals from selected voxels had a range of SNR from 3.2 to 11.6.

#	Sex	Age	Shim Volume (cm^3)	Lesion	TN Stage	Choline	Average Cho SNR ± SD	Average linewidth of Cho peak ± SD	Fatty acid (0.9 ppm)	Fatty acid (1.3 ppm)	Max. axial diameter of tumor (mm)	Min. axial diameter of tumor (mm)	Area for ROI (mm^2)
1	M	41	6×4×1	SCC Node	T2N1	Yes	5.2 ± 1.83	14.9 ± 4.65	+	+	30.7	24.8	487.4
2	M	50	4×4×1	NPC Node	T1N1	Yes	8.28 ± 5.73	11.35 ± 4.8	+	+	33.7	26	673
3	M	53	5×3.4×1	NPC Node	T3N3b	Yes	3.85 ± 1.21	16.4 ± 4.69	+	+	85.7	46.5	2591.4
4	M	52	6×5×1	NPC Node	T2bN1	Yes	9.48 ± 4.64	11.84 ± 5.31	+	+	46.9	27.2	791.4
5	M	55	4×5×1	Schwannoma	NA	Yes	3.0 ± 0.41	21.68 ± 4.71	+	+	33.4	20.1	557.9
6	F	26	4.7×3.7×1	Schwannoma	NA	Yes	7.75 ± 3.69	11.46 ± 0.16	+	+	34.3	22.8	609.8
7	M	54	6×5×1	SCC Node	T4N2	Yes	3.28 ± 1.18	18.03 ± 6.64	+	+	44.2	31.6	1285
8	M	54	6×4×1	NPC Node	T4N2	Yes	2.3	7.41	+	+	41.8	24	739.5
9	M	50	5×2.8×1	NPC Node	T1N1	Yes	4.2	25.5	+	+	18.6	13.6	127.4
10	F	59	3.7×3.7×1	Tonsil SCC	T4N1	CSI failed	NA	NA	NA	NA	35.6	15.4	434.2
11	F	70	4×4×1	Primary NPC	T1N0	CSI failed	NA	NA	NA	NA	27.8	13.2	436.5
12	M	53	6×5×1	Primary NPC	T4N2	CSI failed	NA	NA	NA	NA	31.9	24.9	729.5
13	F	40	5.3×5x1	Palate MECa	T1N0	CSI failed	NA	NA	NA	NA	19.9	16.4	296

Note: (#): Patient No.; (+): Positive Presence of Metabolite; NA: Not Applicable; Schwannoma: Benign Schwannoma; NPC: Undifferentiated Nasopharyngeal Carcinoma; SCC: Squamous Cell Carcinoma; MECa: Mucoepidermoid Carcinoma;

Table4.13: Summary of CSI and histopathologic findings in thirteen patients with head and neck tumors

4.4.6 Discussion and Conclusion of CSI on Patients

Detection of choline signal in human neck lesions with CSI has not been previously reported, although prior studies have been successfully performed using single-voxel (SV) MR spectroscopy (King, A. D. *et al.*, 2004; King, A. D. *et al.*, 2005a; King, A. D. *et al.*, 2005b; King, A. D. *et al.*, 2005c; Mukherji, S. K. *et al.*, 1996; Star-Lack, J. *et al.*, 1998; Wei Huang *et al.*, 2000). The result of this study showed that CSI is feasible in the study of human head and neck tumors when using an anti-susceptibility device filled with liquid perfluorocarbon (PFC) and appropriately selected shimming method. High quality choline maps depicting the distribution of choline-containing compounds (Cho) in large heterogeneous tumor within acceptable scanning time have been shown to be feasible.

This CSI study extended the previous work done with SV methods and demonstrated the feasibility of using CSI to study head and neck tumors. One of the prior studies investigated seven patients with SV ^{1}HMRS and found elevated Cho in all patients with histologically proved squamous cell carcinoma (SCC) of the upper aerodigestive tract (Mukherji, S. K. *et al.*, 1997). Another studies also detected Cho in lymph node metastasis (Chawla, S. *et al.*, 2009; Star-Lack, J. M. *et al.*, 2000) and malignant tumors(Wei Huang *et al.*, 2001). Elevated Cho is found not only in malignant neoplasm, but also in benign neoplasm that is hyper-cellular and in inflammatory processes. In vitro studies at 11T found elevated Cho in benign tumors of the head and neck, including glomus tumors, inverting papillomas and Schwannoma (Maheshwari, S. R. *et al.*, 2000). In vivo studies at 1.5T showed the detectable Cho signals in benign tumors and benign lymphoid hyperplasia (Bisdas, S. *et al.*, 2007). In this CSI study, elevated Cho were found in metastatic lymph nodes

and benign and malignant tumors and their Cho distributions were apparent within the CSI images.

This in vivo CSI study was performed on a clinical 3T scanner. Generally, higher field strength, such as 3T, compared with conventional 1.5 T should provide better signal-to-noise ration (SNR), since the SNR is directly proportional to the magnetic field strength. In MRI, the advantage of better SNR can be used to improve spatial resolution and reduce acquisition times. In MR spectroscopy, higher field strength would provide greater SNR and better spectral resolution. However, the susceptibility effects increase with higher field strength, and thereby leading to lower magnetic field homogeneity over the studied region. In vivo MRS studies have shown that the line-widths were even broader at 3T than at 1.5T (Barker, P. B. *et al.*, 2001). Hence, the use of 3T or above will increase variability in the homogeneity of the magnetic field over the VOI, particularly a large one.

In this study, several strategies were adopted to improve local magnetic field homogeneity. One effective way to improve local magnetic field homogeneity was to use an anti-susceptibility device filled with liquid PFC that has a magnetic susceptibility similar to human tissue. Alternative materials could potentially be used to improve magnetic field homogeneity. The use of water bags behind and around the neck is an inexpensive way to reduce susceptibility artifacts and improve magnetic field homogeneity. Water bags, however, would produce a large amount of unwanted bright signal surrounding the neck, which may be distracting for viewing T2W images. In the CSI data acquisition, any minimal motion of this vast water signal in the phase-encoding direction will immediately induce artifacts in CSI (Rosen, Y. *et al.*, 2007). Hence, because of artifacts induced by the water movement in the water bags, the use of water bags may be less effective for CSI. Other

materials that have the magnetic properties similar to human tissues include silica (SiO_2), alumina (Al_2O_3) and magnesia (MgO). These materials are non-protonated substances that could be potentially used to improve magnetic field homogeneity. The silica-based pads filled with industrial grade silica have been shown to reduce susceptibility-induced artifacts and improve fat saturation of the neck (R. M. Varek and C. Guclu, 2005). Comparing the effectiveness of different materials in improving local magnetic field homogeneity was beyond the scope of the present study and future studies may be necessary to further improve the current method using better materials.

Higher-order shimming was shown to be necessary to correct magnetic field inhomogeneities over the VOI in the head and neck. Local field inhomogeneity may be more complex in the head and neck than the brain due to variations in susceptibility and the geometry of the neck. Higher-order shimming, such as second-order shimming, proved to be an effective means to reduce local field inhomogeneity over a large VOI. Shimming a smaller volume that matches the approximate dimensions of the heterogeneous lesion is another strategy that allows CSI to be performed successfully. Local shimming is less demanding when the shim volume is smaller but the downside is that CSI may not be feasible if lesions are widely spread or located bilaterally.

Despite the encouraging results of this prospective study, there are limitations on applying CSI. In this CSI study, spectra were uninterpretable in four cases when the tumors were located near the tongue and jaw bone (mandible) (Figure 4.23), nasopharynx (Figure 4.24), skull base (Figure 4.25), and hard palate (Figure 4.26). Susceptibility differences in these regions may be very large causing artifacts in the spectra, thereby rendering interpretation more difficult. Hence, tumors in regions of

large susceptibility differences are difficult to evaluate with CSI. Evaluation of head and neck tumors in these difficult regions may, therefore, rely on SV MRS, which is less prone to susceptibility problems. Other possible factors, which could cause difficulties in CSI, were patient movements, such as breathing, swallowing and dental implants.

There are other technical limitations that require attention when performing CSI in the head and neck on patients. Firstly, CSI was only tested using a single slice only, due to the fact that the time required for the study must be reasonably short. Secondly, small shim volume means that lesions that are too large may not be properly studied or may leave other suspicious tissue uninvestigated (Figure 4.27).

In conclusion, this in vivo CSI study demonstrated that proton CSI of the head and neck is feasible with the use of an anti-susceptibility device filled with liquid PFC, and that metabolic mapping of Cho is promising for the non-invasive identification of head and neck tumors. Good quality spectra may be difficult to obtain near nasopharynx, skull base, and hard palate due to high susceptibility differences. CSI, therefore, may have the potential to guide biopsies of head and neck tumors as well as may be useful for characterization of head and neck lesions.

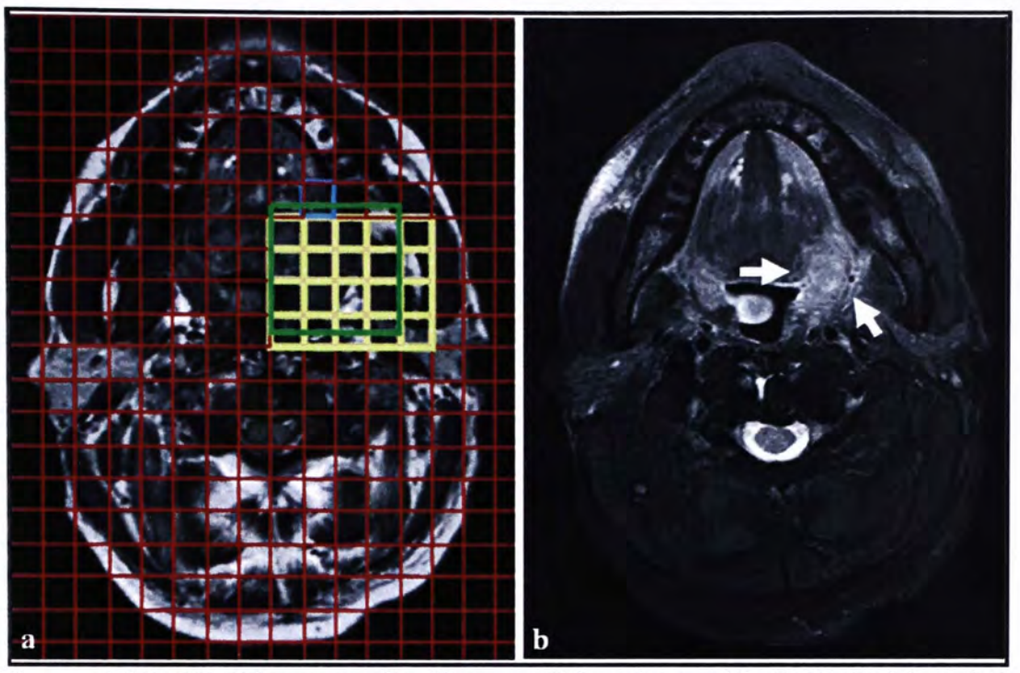

Figure 4.23: MRI images of a 59-year-old patient with SCC (subject 10).

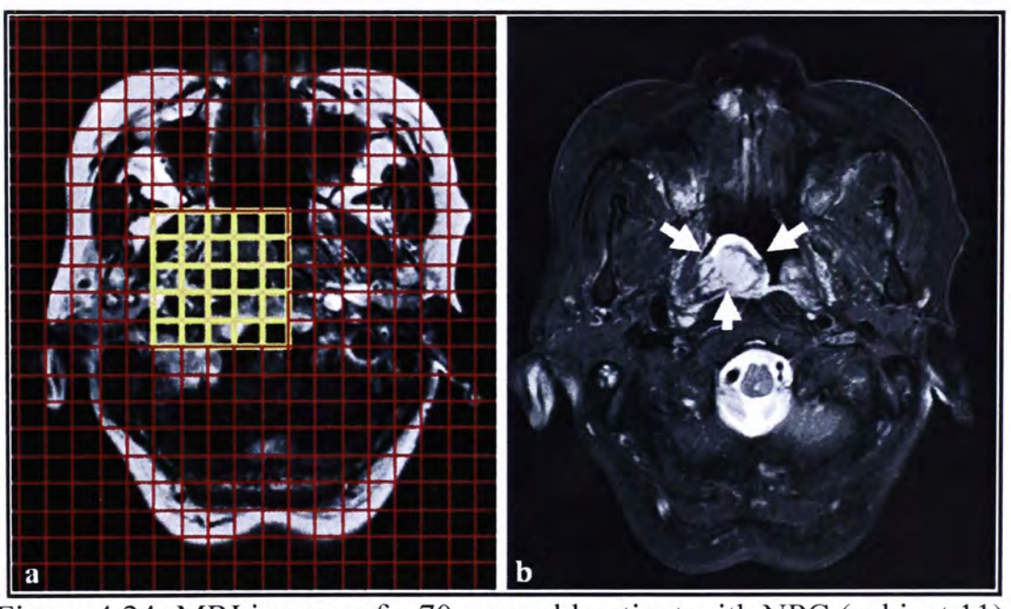

Figure 4.24: MRI images of a 70-year-old patient with NPC (subject 11).

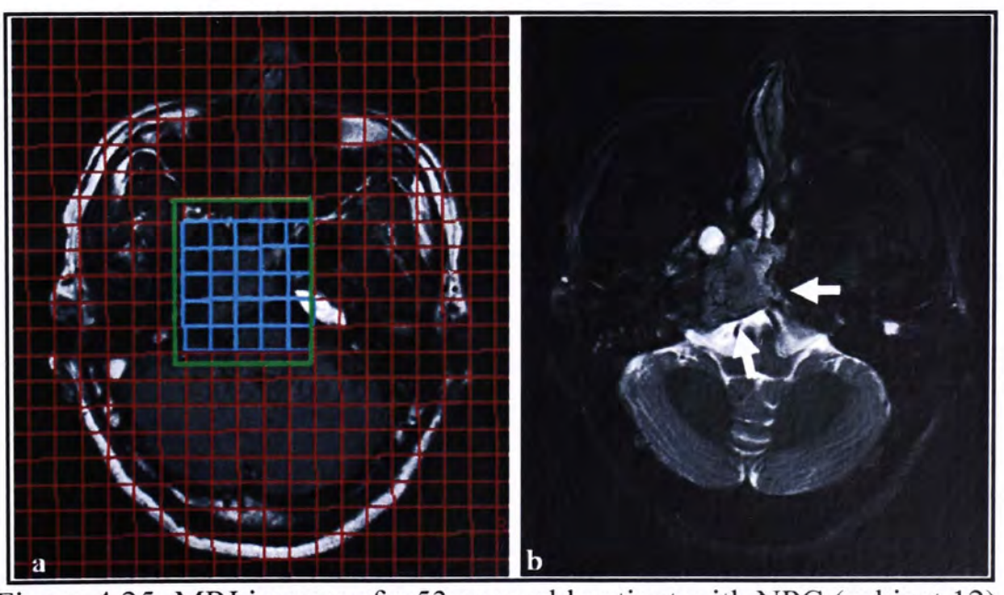

Figure 4.25: MRI images of a 53-year-old patient with NPC (subject 12).

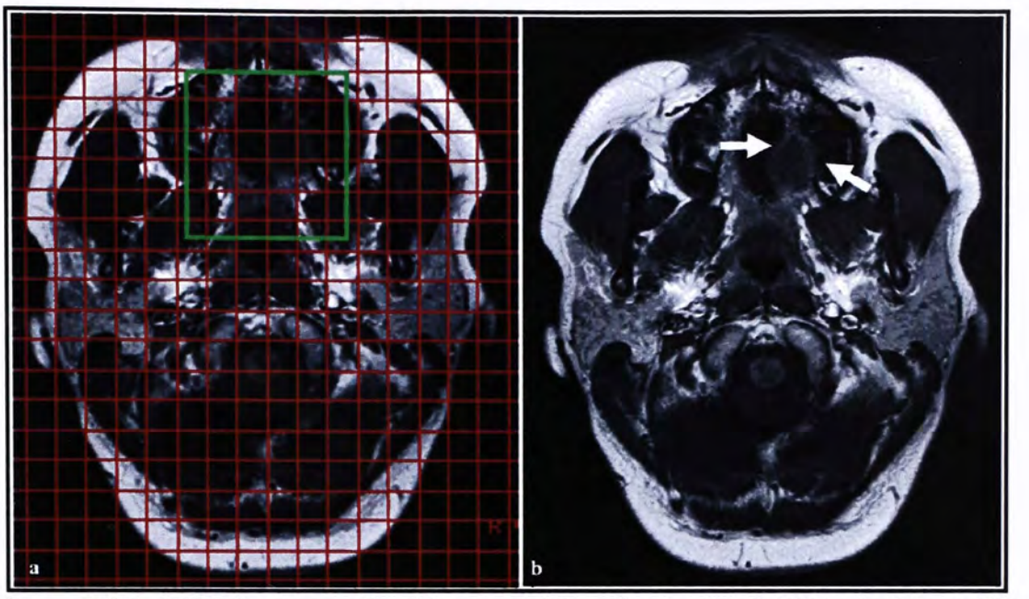

Figure4.26: MRI images of a 40-year-old patient with MECa (subject 13).

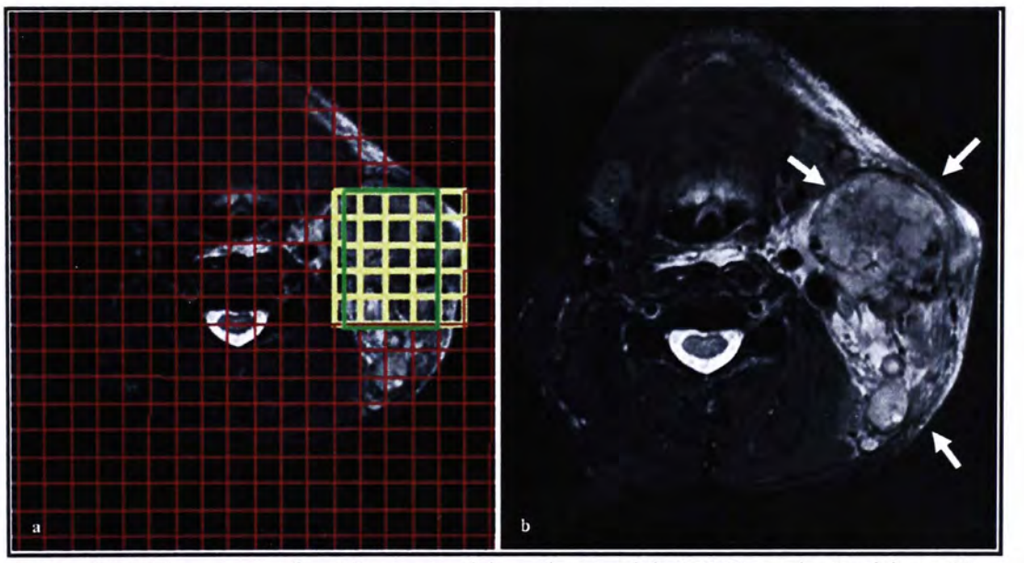

Figure 4.27: MRI images of a 53-year-old patient with NPC node (subject 3).

Chapter 5: Summary, conclusion and future studies

5.1 Summary

DWI and CSI are MRI techniques that both show great potential for examining head and neck tumors, but they both can be difficult to perform in the head and neck due to technical problems including susceptibility artifacts. The results of this thesis show that these technical problems can be overcome and the main findings are summarized as follows:

DWI

- By employing six b values up to 500 s/mm^2, such as 100, 200, 300, 400 and 500 s/mm^2, DWI is feasible for examining head and neck cancers, even at sites that suffer from susceptibility artifacts such as the skull base;
- This study further documented the ADC values of primary NPC and nodal metastases ($0.984 \pm 0.161 \times 10^{-3}$ mm^2/s and $0.852 \pm 0.117 \times 10^{-3}$ mm^2/s, respectively);
- The results have showed that using the single representative section technique for ADC measurement in non necrotic lesions can produce results similar to using the whole lesion technique;
- The results have also showed that the ADC value of NPC lies between that of SCC and NHL and this study has indicated significant differences in the ADC of these three cancers, suggesting that ADC measurement may be useful in the characterization of head and neck cancers;

- This study also indicates that DWI with ADC measurement can be used to produce clinically useful thresholds which may be helpful in distinguishing primary NPC from NHL but not from SCC;
- The results also confirmed previous studies which show clinically useful differences between NHL and SCC.

CSI

- For CSI, the data provided in this study strongly supports the notion that an anti-susceptibility device filled with liquid PFC could significantly improve the local magnetic field homogeneity;
- The results indicated that the best local magnetic field homogeneity in the phantoms could be achieved when using an anti-susceptibility device filled with liquid PFC, together with PB-auto second-order shimming;
- The results also indicated that local shimming could be further improved by shimming a relatively smaller volume of interest, which implies that selecting a shim volume that matches the dimensions of the lesion of interest could significantly increase the likehood of a successful CSI study;
- This study shows that metabolic mapping of Cho is feasible and is a promising non-invasive tool for evaluating head and neck tumors;
- However, good quality spectra may be difficult to obtain near nasopharynx, skull base, and hard palate due to high susceptibility differences.

5.2 Conclusion

DWI is a feasible technique for examining head and neck cancers, even at the site of the skull base. To measure ADC value within non-necrotic lesions in the head and neck, the single representative section technique is preferred. The results showed that ADC values were significant difference among primary NPC, SCC and extra-nodal NHL, suggesting that the ADC measurements may be useful in the characterization of head and neck cancer. For CSI, to the best of my knowledge, the results from this pilot study are the first to demonstrate the feasibility of performing CSI in the head and neck to show metabolic mapping of Cho in head and neck tumors. This information has the potential to detect cancer and guide biopsies.

5.3 Future Studies

Future research is needed in this area, particular concerning a large study group of patients with head and neck lesions, developing techniques further and identifying potential clinical applications. In this study, DWI showed the capability to characterize the ADC of NPC, so that future studies need to assess the changes in tumor ADC after therapy as well as evaluate the role of DWI in monitoring the response to treatment. For CSI of the head and neck, this technique is feasible with the use of an anti-susceptibility device filled with liquid PFC, so that future studies need to further improve the current method using better materials and/ or protocols (e.g. turbo spectroscopic imaging (TSI) and SENSE). Another direction for future studies is to evaluate the diagnostic ability of CSI in the detection and localization of head and neck cancer, prospectively compared with histopathologic findings as well as to assess the role of CSI in monitoring the effects of treatment in patients with head and neck cancer.

References

Abdel Razek, A. A., et al. (2007). "Role of diffusion-weighted echo-planar MR imaging in differentiation of residual or recurrent head and neck tumors and posttreatment changes." AJNR Am J Neuroradiol 28(6): 1146-52.

Abdel Razek, A. A., et al. (2006). "Role of diffusion-weighted MR imaging in cervical lymphadenopathy." Eur Radiol 16(7): 1468-77.

Aikele, P., et al. (2003). "Diffusion-weighted MR imaging of cholesteatoma in pediatric and adult patients who have undergone middle ear surgery." AJR Am J Roentgenol 181(1): 261-5.

Akduman, E. I., et al. (2008). "Comparison between malignant and benign abdominal lymph nodes on diffusion-weighted imaging." Acad Radiol 15(5): 641-6.

Alessandro Lascialfari and M. Corti (2007). Part I: Basic concepts of Magnetic Resonance Imaging. NMR-MRI, uSR and Mossbauer Spectroscopies in Molecular Magnets. Pietro Carretta and A. Lascialfari, Springer Milan: 294.

American Cancer Society (2006). "Cancer Facts & Figures 2006."

Andrzej Dzik-Jurasz and Simon Doran (2006). Chapter 16: Diffusion MR Imaging in Tumors. New techniques in oncologic imaging. A. R. Padhani and P. L. Choyke. New York, Taylor & Francis: 377.

Arend Heerschap (2007). Chapter 13: In Vivo Magnetic Resonance Spectroscopy in Clinical Oncology. In Vivo Imaging of Cancer Therapy. Anthony Frank Shields, Humana PRESS: 326.

Atul B. Mehta and A. Victor Hoffbrand (2000). Chapter 25: Lymphoma I: Hodgkin lymphoma (Hodgkin's disease). Haematology at a glance. Atul B. Mehta and A. Victor Hoffbrand, Blackwell Science Ltd.: 122.

Baek, H. M., et al. (2008). "Detection of choline signal in human breast lesions with chemical-shift imaging." J Magn Reson Imaging 27(5): 1114-21.

Baird, A. E., et al. (1997). "Enlargement of human cerebral ischemic lesion volumes measured by diffusion-weighted magnetic resonance imaging." Ann Neurol 41(5): 581-9.

Bammer, R. (2003). "Basic principles of diffusion-weighted imaging." Eur J Radiol 45(3): 169-84.

Barker, P. B., et al. (2001). "Single-voxel proton MRS of the human brain at 1.5T and 3.0T." Magn Reson Med 45(5): 765-9.

Baur, A., et al. (1998). "Diffusion-weighted MR imaging of bone marrow: differentiation of benign versus pathologic compression fractures." Radiology 207(2): 349-56.

Bisdas, S., et al. (2007). "In vivo proton MR spectroscopy of primary tumours, nodal and recurrent disease of the extracranial head and neck." Eur Radiol 17(1): 251-7.

Brateman, L. (1986). "Chemical shift imaging: a review." AJR Am J Roentgenol 146(5): 971-80.

Bruce Brockstein and Gregory Masters (2003). Chapter 1: Overview of Head and Neck Cancer. Head and Neck Cancer. Bruce Brockstein and Gregory Masters, Kluwer Academic Publishers: 114.

Brun, E., et al. (2002). "FDG PET studies during treatment: prediction of therapy outcome in head and neck squamous cell carcinoma." Head Neck 24(2): 127-35.

Brunberg, J. A., et al. (1995). "In vivo MR determination of water diffusion coefficients and diffusion anisotropy: correlation with structural alteration in gliomas of the cerebral hemispheres." AJNR Am J Neuroradiol 16(2): 361-71.

Castillo, M., et al. (2001). "Apparent diffusion coefficients in the evaluation of high-grade cerebral gliomas." AJNR Am J Neuroradiol 22(1): 60-4.

Catherine Castaigne, et al. (2008). Chapter 17: Position Emission Tomography in Head and Neck Cancer. Head and Neck Cancer Imaging. R. Hermans, Springer: 370.

Catherine Westbrook, et al. (2005). MRI in Practice (3 ed.): Wiley-Blackwell.

Catherine Westbrook. and C. K. Roth (2005). Chapter 1 Basic principles. MRI in Practice. C. W. C. K. Roth, Wiley-Blackwell: 326.

Chawla, S., et al. (2009). "Proton and phosphorous MR spectroscopy in squamous cell carcinomas of the head and neck." Acad Radiol 16(11): 1366-72.

Choi, H. and J. Ma (2008). "Use of perfluorocarbon compound in the endorectal coil to improve MR spectroscopy of the prostate." AJR Am J Roentgenol 190(4): 1055-9.

de Bondt, R. B., et al. (2009). "Diagnostic accuracy and additional value of diffusion-weighted imaging for discrimination of malignant cervical lymph nodes in head and neck squamous cell carcinoma." Neuroradiology 51(3): 183-92.

De Stefano, N., et al. (1998). "In vivo differentiation of astrocytic brain tumors and isolated demyelinating lesions of the type seen in multiple sclerosis using 1H magnetic resonance spectroscopic imaging." Ann Neurol 44(2): 273-8.

Denis Le Bihan, et al. (1988). "Separation of diffusion and perfusion in intravoxel incoherent motion MR imaging." Radiology 168(2): 497-505.

Donald W. McRobbie, et al. (2003). Chapter 15: It's not just squiggles: in vivo spectroscopy. MRI from picture to proton. D. W. McRobbie, E. A. Moore, M. J. Graves and M. R. Prince, Cambridge: 359.

Dubrulle, F., et al. (2006). "Diffusion-weighted MR imaging sequence in the detection of postoperative recurrent cholesteatoma." Radiology 238(2): 604-10.

Dzik-Jurasz, A., et al. (2002). "Diffusion MRI for prediction of response of rectal cancer to chemoradiation." Lancet 360(9329): 307-8.

Edward F. Jackson (2001). Chapter 4: Principles of Magnetic Resonance Imaging and Magnetic Resonance Spectroscopy. Targeted molecular imaging in oncology. E. E. Kim and D. J. Yang, Springer: 289.

Filippi, C. G., et al. (2001). "Appearance of meningiomas on diffusion-weighted images: correlating diffusion constants with histopathologic findings." AJNR Am J Neuroradiol 22(1): 65-72.

Forastiere, A. A., et al. (2003). "Concurrent chemotherapy and radiotherapy for organ preservation in advanced laryngeal cancer." N Engl J Med 349(22): 2091-8.

Frederick L. Greene, et al. (2006). AJCC Cancer Staging Atlas (ed.): Springer.

Friedrich, K. M., et al. (2008). "Diffusion-weighted magnetic resonance imaging of head and neck squamous cell carcinomas." Eur J Radiol 68(3): 493-8.

Furuya, S., et al. (1997). "Evaluation of metabolic heterogeneity in brain tumors using 1H-chemical shift imaging method." NMR Biomed 10(1): 25-30.

Gary Liney (2006). Chapter I: The Basics. MRI in Clinical Practice. Gary Liney, Springer London: 128.

Gonzalez, R. G., et al. (1999). "Diffusion-weighted MR imaging: diagnostic accuracy in patients imaged within 6 hours of stroke symptom onset." Radiology 210(1): 155-62.

Gruetter, R. (1993). "Automatic, localized in vivo adjustment of all first- and second-order shim coils." Magn Reson Med 29(6): 804-11.

Guo, A. C., et al. (2002). "Lymphomas and high-grade astrocytomas: comparison of water diffusibility and histologic characteristics." Radiology 224(1): 177-83.

Hayashida, Y., et al. (2006). "Monitoring therapeutic responses of primary bone tumors by diffusion-weighted image: Initial results." Eur Radiol 16(12): 2637-43.

Heidi Johansen-Berg and Timothy E. J. Behrens (2009). Diffusion MRI: From quantitative measurement to in-vivo neuroanatomy (1 ed.): Academic Press.

Hein, P. A., et al. (2004). "Diffusion-weighted imaging in the follow-up of treated high-grade gliomas: tumor recurrence versus radiation injury." AJNR Am J Neuroradiol 25(2): 201-9.

Her, C. (2001). "Nasopharyngeal cancer and the Southeast Asian patient." Am Fam Physician 63(9): 1776-82.

Hermann, E. J., et al. (2008). "Stereotactic biopsy in gliomas guided by 3-tesla 1H-chemical-shift imaging of choline." Stereotact Funct Neurosurg 86(5): 300-7.

Holzapfel, K., et al. (2009). "Value of diffusion-weighted MR imaging in the differentiation between benign and malignant cervical lymph nodes." Eur J Radiol 72(3): 381-7.

Hong Kong Cancer Registry (2008). Hong Kong Cancer Stat 2006. Hong Kong, Hong Kong Cancer Registry, Hospital Authority.

Hricak, H. (2005). "MR imaging and MR spectroscopic imaging in the pre-treatment evaluation of prostate cancer." Br J Radiol 78 Spec No 2: S103-11.

Ian C.P. Smith and L. C. Stewart (2002). "Magnetic resonance spectroscopy in medicine: clinical impact." Progress in Nuclear Magnetic Resonance Spectroscopy 40: 1-34.

Issa, B. (2002). "In vivo measurement of the apparent diffusion coefficient in normal and malignant prostatic tissues using echo-planar imaging." J Magn Reson Imaging 16(2): 196-200.

Jacobs, M. A., et al. (2004). "Proton magnetic resonance spectroscopic imaging of human breast cancer: a preliminary study." J Magn Reson Imaging 19(1): 68-75.

Joseph G. Och, et al. (1992). "Acceptance testing of magnetic resonance imaging systems: report of AAPM Nuclear Magnetiç Resonance Task Group No. 6." Med Phys 19(1): 217-29.

Karen Belkic (2004). Chapter 11: Head and Neck Cancer. Molecular Imaging Through Magnetic Resonance for Clinical Oncology, CISP: 320.

Kato, H., et al. (2009). "Head and neck squamous cell carcinoma: usefulness of diffusion-weighted MR imaging in the prediction of a neoadjuvant therapeutic effect." Eur Radiol 19(1): 103-9.

Kawai, Y., et al. (2005). "Diffusion-weighted MR microimaging of the lacrimal glands in patients with Sjogren's syndrome." AJR Am J Roentgenol 184(4): 1320-5.

Kim, S., et al. (2009). "Diffusion-weighted magnetic resonance imaging for predicting and detecting early response to chemoradiation therapy of squamous cell carcinomas of the head and neck." Clin Cancer Res 15(3): 986-94.

Kim, T., et al. (1999). "Diffusion-weighted single-shot echoplanar MR imaging for liver disease." AJR Am J Roentgenol 173(2): 393-8.

Kim, Y. J., et al. (1998). "Brain abscess and necrotic or cystic brain tumor: discrimination with signal intensity on diffusion-weighted MR imaging." AJR Am J Roentgenol 171(6): 1487-90.

King, A. D., et al. (2004). "In vivo proton MR spectroscopy of primary and nodal nasopharyngeal carcinoma." AJNR Am J Neuroradiol 25(3): 484-90.

King, A. D., et al. (2005a). "In vivo 1H MR spectroscopy of thyroid carcinoma." Eur J Radiol 54(1): 112-7.

King, A. D., et al. (2005b). "Salivary gland tumors at in vivo proton MR spectroscopy." Radiology 237(2): 563-9.

King, A. D., et al. (2005c). "Human cervical lymphadenopathy: evaluation with in vivo 1H-MRS at 1.5 T." Clin Radiol 60(5): 592-8.

King, A. D., et al. (2009). "Monitoring of treatment response after chemoradiotherapy for head and neck cancer using in vivo (1)H MR spectroscopy." Eur Radiol.

Klose, U. (2008). "Measurement sequences for single voxel proton MR spectroscopy." Eur J Radiol 67(2): 194-201.

Koh, D. M. and D. J. Collins (2007). "Diffusion-weighted MRI in the body: applications and challenges in oncology." AJR Am J Roentgenol 188(6): 1622-35.

Kostakoglu, L. and S. J. Goldsmith (2004). "PET in the assessment of therapy response in patients with carcinoma of the head and neck and of the esophagus." J Nucl Med 45(1): 56-68.

Kuroki, Y., et al. (2004). "Diffusion-weighted imaging of breast cancer with the sensitivity encoding technique: analysis of the apparent diffusion coefficient value." Magn Reson Med Sci 3(2): 79-85.

Lam, W. W., et al. (1997). "Retropharyngeal lymphadenopathy in nasopharyngeal carcinoma." Head Neck 19(3): 176-81.

Le Bihan, D., et al. (1988). "Separation of diffusion and perfusion in intravoxel incoherent motion MR imaging." Radiology 168(2): 497-505.

Le Bihan, D., et al. (2006). "Artifacts and pitfalls in diffusion MRI." J Magn Reson Imaging 24(3): 478-88.

Lee, J., et al. (2004). "Clinical evaluation of choline measurement by proton MR spectroscopy in patients with malignant tumors." Radiat Med 22(3): 148-54.

Lindsay T. Byrne (2008). Chapter 3: Nuclear Magnetic Resonance Spectroscopy: Strategies for Structural Determination. Bioactive natural products; detection, isolation, and structural determination. Steven M. Colegate and R. J. Molyneux, CRC / Taylor & Francis: 605.

Lovblad, K. O., et al. (1998). "Clinical experience with diffusion-weighted MR in patients with acute stroke." AJNR Am J Neuroradiol 19(6): 1061-6.

Lyng, H., et al. (2000). "Measurement of cell density and necrotic fraction in human melanoma xenografts by diffusion weighted magnetic resonance imaging." Magn Reson Med 43(6): 828-36.

Maeda, M., et al. (2005). "Usefulness of the apparent diffusion coefficient in line scan diffusion-weighted imaging for distinguishing between squamous cell carcinomas and malignant lymphomas of the head and neck." AJNR Am J Neuroradiol 26(5): 1186-92.

Maeda, M., et al. (2003). "Quantitative assessment of diffusion abnormalities in benign and malignant vertebral compression fractures by line scan diffusion-weighted imaging." AJR Am J Roentgenol 181(5): 1203-9.

Maheshwari, S. R., et al. (2000). "The choline/creatine ratio in five benign neoplasms: comparison with squamous cell carcinoma by use of in vitro MR spectroscopy." AJNR Am J Neuroradiol 21(10): 1930-5.

Mark A. Brown and Richard C. Semelka (2006). Chapter 2 Magnetic Resonance Imaging Principles and Applications. Computed body tomography with MRI correlation. J. K. T. Lee, S. S. Sagel, R. J. Stanley and J. P. Heiken, Philadelphia : Lippincott Williams & Wilkins. 1: 2050.

Matsuki, M., et al. (2007). "Diffusion-weighted MR imaging for urinary bladder carcinoma: initial results." Eur Radiol 17(1): 201-4.

McKnight, T. R., et al. (2007). "Correlation of magnetic resonance spectroscopic and growth characteristics within Grades II and III gliomas." J Neurosurg 106(4): 660-6.

Miller, A. B., et al. (1981). "Reporting results of cancer treatment." Cancer 47(1): 207-14.

Misa Sumi, N. (2003). "Discrimination of metastatic cervical lymph nodes with diffusion-weighted MR imaging in patients with head and neck cancer." 24(8): 1627-34.

Mori, S. and P. B. Barker (1999). "Diffusion magnetic resonance imaging: its principle and applications." Anat Rec 257(3): 102-9.

Moteki, T. and H. Ishizaka (1999). "Evaluation of cystic ovarian lesions using apparent diffusion coefficient calculated from reordered turboflash MR images." Magn Reson Imaging 17(7): 955-63.

Mukherji, S. K. and R. J. Gerstle (1998). "In vitro 1H MR spectroscopy of squamous cell carcinoma of the extracranial head and neck." Neuroimaging Clin N Am 8(4): 835-47.

Mukherji, S. K., et al. (1997). "Proton MR spectroscopy of squamous cell carcinoma of the extracranial head and neck: in vitro and in vivo studies." AJNR Am J Neuroradiol 18(6): 1057-72.

Mukherji, S. K., et al. (1996). "Proton MR spectroscopy of squamous cell carcinoma of the upper aerodigestive tract: in vitro characteristics." AJNR Am J Neuroradiol 17(8): 1485-90.

Namimoto, T., et al. (1997). "Focal liver masses: characterization with diffusion-weighted echo-planar MR imaging." Radiology 204(3): 739-44.

Narayana, A., et al. (2007). "Use of MR spectroscopy and functional imaging in the treatment planning of gliomas." Br J Radiol 80(953): 347-54.

Nelson, S. J. (2003). "Multivoxel magnetic resonance spectroscopy of brain tumors." Mol Cancer Ther 2(5): 497-507.

Nelson, S. J., et al. (2002). "In vivo molecular imaging for planning radiation therapy of gliomas: an application of 1H MRSI." J Magn Reson Imaging 16(4): 464-76.

Nouha Mikhael Salibi and Mark A. Brown (1998). Clinical MR spectroscopy: First Principles (1 ed.): Wiley-Liss.

Oberholzer, K., et al. (2008). "Assessment of tumor microcirculation with dynamic contrast-enhanced MRI in patients with esophageal cancer: initial experience." J Magn Reson Imaging 27(6): 1296-301.

Okamoto, K., et al. (2000). "Diffusion-weighted echo-planar MR imaging in differential diagnosis of brain tumors and tumor-like conditions." Eur Radiol 10(8): 1342-50.

Payne, G. S. and M. O. Leach (2006). "Applications of magnetic resonance spectroscopy in radiotherapy treatment planning." Br J Radiol 79 Spec No 1: S16-26.

Peter B. Barker (2005). Section 1: Chpater 1: Fundamentals of MR spectroscopy. Clinical MR neuroimaging: diffusion, perfusion, and spectroscopy. Jonathan H. Gillard, Adam D. Waldman and P. B. Barker, Cambridge: 827.

Quon, H., et al. (2001). "Potential molecular prognostic markers in head and neck squamous cell carcinomas." Head Neck 23(2): 147-59.

R. M. Varek and C. Guclu (2005). "Improving Field Homogeneity on Fat-Suppressed Cervical Spine Images." Proceedings of the International Society for Magnetic Resonance in Medicine 13: 1976.

R.H. Wu, et al. (2003). Evaluation of chemical shift imaging using a two-dimensional PRESS CSI sequence: work in progress. The 25th Annual International Conference of the IEEE EMBS, Cancum, Mexico.

Robin de Graaf (2004). Chapter 3: Techniques-MRS, fMRI, 13C NMR, Indirect Detection of 13C. Brain energetics and neuronal activity: applications to fMRI and medicine. R. G. Shulman and D. L. Rothman, John Wiley & Sons, Ltd.: 321.

Rosen, Y., et al. (2007). "3T MR of the prostate: reducing susceptibility gradients by inflating the endorectal coil with a barium sulfate suspension." Magn Reson Med 57(5): 898-904.

Ross, B. D., et al. (2003). "Evaluation of cancer therapy using diffusion magnetic resonance imaging." Mol Cancer Ther 2(6): 581-7.

Sakamoto, J., et al. (2009). "Tissue characterization of head and neck lesions using diffusion-weighted MR imaging with SPLICE." Eur J Radiol 69(2): 260-8.

Sardanelli, F., et al. (2009). "In vivo proton MR spectroscopy of the breast using the total choline peak integral as a marker of malignancy." AJR Am J Roentgenol 192(6): 1608-17.

Schaefer, P. W. (2001). "Applications of DWI in clinical neurology." J Neurol Sci 186 Suppl 1: S25-35.

Schaefer, P. W., et al. (2000). "Diffusion-weighted MR imaging of the brain." Radiology 217(2): 331-45.

Schaeffter, T. and H. Dahnke (2008). "Magnetic resonance imaging and spectroscopy." Handb Exp Pharmacol(185 Pt 1): 75-90.

Schenck, J. F. (1996). "The role of magnetic susceptibility in magnetic resonance imaging: MRI magnetic compatibility of the first and second kinds." Med Phys 23(6): 815-50.

Shah, N., et al. (2006). "Magnetic resonance spectroscopy as an imaging tool for cancer: a review of the literature." J Am Osteopath Assoc 106(1): 23-7.

Sinha, S., et al. (2002). "In vivo diffusion-weighted MRI of the breast: potential for lesion characterization." J Magn Reson Imaging 15(6): 693-704.

Skoch, A., et al. (2008). "Spectroscopic imaging: basic principles." Eur J Radiol 67(2): 230-9.

Son, B. C., et al. (2001). "Proton magnetic resonance chemical shift imaging (1H CSI)-directed stereotactic biopsy." Acta Neurochir (Wien) 143(1): 45-9; discussion 49-50.

Sorensen, A. G., et al. (1996). "Hyperacute stroke: evaluation with combined multisection diffusion-weighted and hemodynamically weighted echo-planar MR imaging." Radiology 199(2): 391-401.

Star-Lack, J., et al. (1998). "In vivo lactate editing with simultaneous detection of choline, creatine, NAA, and lipid singlets at 1.5 T using PRESS excitation with applications to the study of brain and head and neck tumors." J Magn Reson 133(2): 243-54.

Star-Lack, J. M., et al. (2000). "In vivo 1H MR spectroscopy of human head and neck lymph node metastasis and comparison with oxygen tension measurements." AJNR Am J Neuroradiol 21(1): 183-93.

Sugahara, T., et al. (1999). "Usefulness of diffusion-weighted MRI with echo-planar technique in the evaluation of cellularity in gliomas." J Magn Reson Imaging 9(1): 53-60.

Sumi, M., et al. (2007). "Diagnostic ability of apparent diffusion coefficients for lymphomas and carcinomas in the pharynx." Eur Radiol 17(10): 2631-7.

Sumi, M., et al. (2002). "Diffusion-weighted echoplanar MR imaging of the salivary glands." AJR Am J Roentgenol 178(4): 959-65.

Sumi, M., et al. (2006). "MR microimaging of benign and malignant nodes in the neck." AJR Am J Roentgenol 186(3): 749-57.

Sundgren, P. C., et al. (2009). "Metabolic alterations: a biomarker for radiation-induced normal brain injury-an MR spectroscopy study." J Magn Reson Imaging 29(2): 291-7.

Suresh K. Mukherji, et al. (2004). "Clinical applications of tumor volume measurements for predicting outcome in patients with squamous cell carcinoma of the upper aerodigestive tract." AJNR Am J Neuroradiol 25(8): 1425-32.

Swindle, P., et al. (2003). "Pathologic characterization of human prostate tissue with proton MR spectroscopy." Radiology 228(1): 144-51.

T. Scarabino, et al. (2006). Chapter 7: 3.0 T Diffusion Studies. High field brain MRI: use in clinical practice. U. S. Salvolini, T. New York, Springer: 237.

Tanner, S. F., et al. (2000). "Quantitative comparison of intrabrain diffusion in adults and preterm and term neonates and infants." AJR Am J Roentgenol 174(6): 1643-9.

Therasse, P., et al. (2000). "New guidelines to evaluate the response to treatment in solid tumors. European Organization for Research and Treatment of Cancer, National Cancer Institute of the United States, National Cancer Institute of Canada." J Natl Cancer Inst 92(3): 205-16.

Thoeny, H. C., et al. (2005). "Diffusion-weighted MR imaging of kidneys in healthy volunteers and patients with parenchymal diseases: initial experience." Radiology 235(3): 911-7.

Tien, R. D., et al. (1994). "MR imaging of high-grade cerebral gliomas: value of diffusion-weighted echoplanar pulse sequences." AJR Am J Roentgenol 162(3): 671-7.

Tsuruda, J. S., et al. (1990). "Diffusion-weighted MR imaging of the brain: value of differentiating between extraaxial cysts and epidermoid tumors." AJR Am J Roentgenol 155(5): 1059-65; discussion 1066-8.

Urba, S. G., et al. (2000). "Neoadjuvant therapy for organ preservation in head and neck cancer." Laryngoscope 110(12): 2074-80.

Vandecaveye, V., et al. (2007). "Detection of head and neck squamous cell carcinoma with diffusion weighted MRI after (chemo)radiotherapy: correlation between radiologic and histopathologic findings." Int J Radiat Oncol Biol Phys 67(4): 960-71.

Vandecaveye, V., et al. (2006). "Evaluation of the larynx for tumour recurrence by diffusion-weighted MRI after radiotherapy: initial experience in four cases." Br J Radiol 79(944): 681-7.

Vega, F., et al. (2005). "Extranodal lymphomas of the head and neck." Ann Diagn Pathol 9(6): 340-50.

Wang, J., et al. (2001). "Head and neck lesions: characterization with diffusion-weighted echo-planar MR imaging." Radiology 220(3): 621-30.

Warach, S., et al. (1995). "Acute human stroke studied by whole brain echo planar diffusion-weighted magnetic resonance imaging." Ann Neurol 37(2): 231-41.

Wei Huang, et al. (2000). "Evaluation of Head and Neck Tumor Response to Therapy Using In Vivo 1H MR Spectroscopy: Correlation with Pathology." Proc. Intl. Soc. Mag. Reson. Med. 8: 552.

Wei Huang, et al. (2001). "Evaluation of Thyroid Masses Using In Vivo 1H MR Spectroscopy: Correction with Pathology." Proc. Intl. Soc. Mag. Reson. Med. 9: 2347.

Wen -Yih Isaac Tseng and Li-Wei Kuo (2008). Diffusion Magnetic Resonance Imaging in Neuroimaging. Novel Trends in Brain Science: Brain Imaging, Learning and Memory, Stress and Fear, and Pain. M. Onozuka and C.-T. Yen, Springer: 254.

Yamashita, Y., et al. (1998). "Mucin-producing tumor of the pancreas: diagnostic value of diffusion-weighted echo-planar MR imaging." Radiology 208(3): 605-9.

Yoshino, N., et al. (2001). "Salivary glands and lesions: evaluation of apparent diffusion coefficients with split-echo diffusion-weighted MR imaging--initial results." Radiology 221(3): 837-42.

Zakian, K. L., et al. (2005). "Correlation of proton MR spectroscopic imaging with gleason score based on step-section pathologic analysis after radical prostatectomy." Radiology 234(3): 804-14.

Publications

"Diffusion-weighted Magnetic Resonance Imaging of Nasopharyngeal Carcinoma"

D. K. Fong, A. D. King, F. K. Lee, Q. Chan, and D. Yeung

Pro. Intl. Soc. Mag. Reson. Med. 17, pg 1316, Apr 2009.

"Diagnostic Accuracy of Diffusion-weighted MR Imaging for Nasopharyngeal Carcinoma, Head and Neck Lymphoma and Squamous Cell Carcinoma at the Primary Site." Kwan-Ying Fong, K SS Bhatia, D.K. Yeung and Ann D King (paper submitted)

"Chemical Shift Imaging in the Head and Neck at 3T: Initial Results"

D. K. Yeung, Kwan-Ying Fong, Q. Chan, and A. D. King

SMRT 19th Annual Meeting (May 2010) (Accepted)

"Chemical Shift Imaging in the Head and Neck at 3T: Initial Results"

D. K. Yeung, Kwan-Ying Fong, Q. Chan, and A. D. King (paper submitted)